Journal of
Mechanics of
Materials and Structures

JOURNAL OF MECHANICS OF MATERIALS AND STRUCTURES

msp.org/jomms

Founded by Charles R. Steele and Marie-Louise Steele

Cover photo: Ev Shafrir

ON THE VIBRATION SIMULATION OF SUBMERGED PIPES: STRUCTURAL HEALTH MONITORING ASPECTS

PEJMAN RAZI AND FARID TAHERI

This work aims to provide further insight into the modeling aspects and influence of some important parameters involved in the simulation of vibration of submerged pipes, especially in relation to vibration-based structural health monitoring (VB-SHM) techniques. Two widely used techniques for modeling submerged pipelines, namely the "added mass" and "coupled acoustic-structural" approaches are compared, and their limitations and advantages in the context of VB-SHM are highlighted. Moreover, the paper also presents a comprehensive study of the effect of operational variability on the accuracy of VB-SHM of offshore pipelines. It is demonstrated that the geometric stiffness produced by the operational variability (such as changes in the internal and external pressures of pipelines) could variably alter the overall stiffness of such submerged bodies, hence affecting their dynamic response. Depending on the pipe stiffness, the imposed variations could significantly affect the accuracy of VB-SHM trials.

A list of symbols can be found on page 121.

Introduction

Vibration-based structural health monitoring (VB-SHM) of submerged structures has received several researchers' attentions in recent years [Peng and Hao 2012; Peng et al. 2012; Zhu et al. 2008; Chen et al. 2010; Na and Kundu 2002; Bao et al. 2013; Rizzo et al. 2010]. Some of these studies have included numerical simulations of their damage detection case studies in addition to their experimental verifications [Peng and Hao 2012; Peng et al. 2012; Zhu et al. 2008; Chen et al. 2010; Bao et al. 2013]. In some of those numerical studies, the fluid-structure interaction (FSI) has been idealized by using the concept of "added mass" [Peng and Hao 2012; Peng et al. 2012; Zhu et al. 2008; Bao et al. 2013] while others have adopted a more elaborate approach, namely the "coupled acoustic-structural" method, in their numerical simulations [Chen et al. 2010].

It has been shown that the idealization in representing the FSI could lead to erroneous predictions. For instance, Zeinoddini et al. [2012] compared the performances of the added mass approach (AMA) against the "coupled acoustic-structural" approach (CASA) in predicting the seismic and harmonic responses of an offshore pipeline's free-spanning (a segment of a pipe that is suspended and does not have the seabed support). They showed that the conventional AMA generally provided more conservative predictions in comparison to the CASA. With the application of the AMA, the maximum mid-span deflection of the pipe was predicted to be about 6% higher than the one obtained through the CASA. The reason was postulated to be because that the AMA inherently overlooks the dynamic pressure wave travel and therefore provides more conservative predictions.

Moreover, the simple "added mass" term can only be formulated where the velocity potential function around a vibrating structure is mathematically definable [Blevins 2001]. Kramer et al. [2013] adopted the "added-mass" term, which was originally formulated for analyzing the vibration of a submerged beam, to study the free vibration of submerged composite plates. They showed that the adoption of the AMA instead of CASA could yield inaccurate results in predicting the eigenvalues of the submerged plates with low aspect ratios (length/width). However, the predictions were in good agreement when the plates had larger aspect ratios (close to a beam-type geometry).

Therefore, in order to do an effective and accurate VB-SHM of submerged structures, one needs to gain a better understanding of the influence of such idealization in representing the associated FSI.

In addition to the modeling aspects, certain combinations of operational variables could adversely affect VB-SHM of submerged structures. Specific to offshore pipelines, variation in the internal pressure (due to a drop and/or an increase in the internal fluid's pressure) or in the external pressure (upon possible changes in the depth of submergence) could variably modify the geometric stiffness of the pipes, thereby affecting their vibration. If deviance in the vibration characteristic is noticeable, it could lead to a false alarm in detecting damage. Therefore, the VB-SHM of submerged structures would be vulnerable to the presence of such operational variability.

Zou et al. [2005] reported negligible variation in the bending eigenvalues of a composite pipe subjected to a variable internal pressure. Ross et al. [2007], however, observed significant reductions in the eigenvalues of a submerged urethane prolate when subjected to a variable external pressure.

Moreover, to the best of authors' knowledge, the influence of such operational variability on the accuracy of VB-SHM has not been addressed [Peng and Hao 2012; Peng et al. 2012; Zhu et al. 2008; Bao et al. 2013; 2011; Rezaei and Taheri 2010; Razi et al. 2013].

The present study aims to investigate the effect of above-mentioned influential parameters on the accuracy of a vibration-based damage detection methodology when applied to submerged pipes. Accordingly, the main objectives of the current research can be listed as follows.

- To identify the more suitable approach (i.e., AMA or CASA) for numerical simulation of submerged structures with particular emphasis on VB-SHM. This is achieved by comparing the efficiency and accuracy of the "added mass" and "coupled acoustic-structural" approaches in analyzing the vibration response of a submerged steel pipe.

- To gain an insight on the influence of operational variability on the accuracy of VB-SHM of submerged structures. This is addressed by investigating the vibration response of submerged steel and composite pipes that are subject to variable internal and/or external pressures.

Evaluation of the performance of "added mass" and "coupled acoustic-structural" approaches within the context of VB-SHM

In this section, the theories of AMA and CASA are first reviewed. Then the response of a submerged API-5L X65 steel pipe is numerically modeled by the two approaches, and its eigenvalues are investigated.

Theory of the added mass approach. Consider a pipe vibrating in a body of water in the direction shown in Figure 1. The dynamic response of the pipe can be determined once the applied force acting on its surface is formulated. For this purpose, the pressure distribution around the pipe's circumference
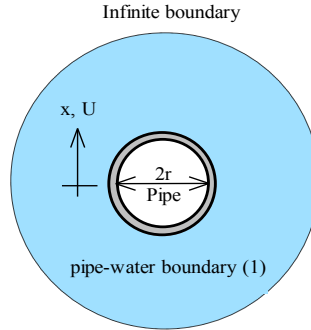
Figure 1. A pipe vibrating in a large body of fluid.

should be identified. Euler's equation [Cengel and Cimbala 2006] describes the relationship between the pressure gradient and velocity of the fluid in an unsteady flow (note that the lateral vibration of the pipe causes an unsteady flow around the pipe). For an incompressible fluid, Euler's equation can be written as

$$\frac{\partial V}{\partial t} + (V \cdot \nabla)V = -\frac{1}{\rho}\nabla p - g\nabla z. \tag{1}$$

The above equation can be simplified as [Blevins 2001]

$$\nabla\left(\frac{\partial \phi}{\partial t} + \tfrac{1}{2}V^2 + \frac{p}{\rho_f} + gz\right) = 0. \tag{2}$$

The above identity implies that the quantity within the parentheses is not a function of space. Therefore, for an arbitrary location within the fluid domain, one can assume

$$p_s = -\rho_f \frac{\partial \phi}{\partial t} - \tfrac{1}{2}\rho_f V^2 - \rho_f gh. \tag{3}$$

The above equation, which describes the static pressure as a function of the velocity potential, is called the generalized Bernoulli equation.

Bernoulli's equation is applicable to incompressible fluids and in parts of a flow in which the effect of viscosity is negligible [Cengel and Cimbala 2006]. As can be seen from (3), in order to obtain the static pressure, the velocity potential has to be identified. Once that is done, the velocity vector can be subsequently evaluated by the following equation and its magnitude substituted in (3) [Cengel and Cimbala 2006]:

$$V = \nabla\phi. \tag{4}$$

It has been shown that the velocity potential for a region around a cylinder vibrating laterally in a reservoir containing stationary fluid can be expressed by [Blevins 2001]

$$\phi = \frac{U(t)r^2[x - X(t)]}{[x - X(t)]^2 + y^2}, \tag{5}$$

where x and y are the coordinates of points of interest.

Substituting the time derivative of (5) into (3), then integrating the pressure term over the circumference of the pipe, one would obtain the net force per unit length as

$$F = -\rho_f \pi r^2 \frac{dU(t)}{dt} i, \tag{6}$$

where i signifies the direction of the vector (here along the x axis, as shown in Figure 1). As can be seen, the force exerted by the fluid is opposing the pipe's motion since it is acting against the pipe's vibration.

It is very important to note that the term $\rho_f gh$, which represents the hydrostatic pressure in (3), has no contribution to the net force. The hydrostatic pressure is assumed to be uniformly distributed around the pipe's circumference; thus, from the perspective of total net force, the total finite forces generated by this term would cancel one another. However, this pressure could shift the eigenvalues of the pipe as will be explained in the following sections.

Assuming the motion of the pipe (cylinder) is a single-degree-of-freedom system, one can rearrange the equation of motion as

$$(M + \rho_f \pi r^2) \frac{d^2 X(t)}{dt^2} + K X(t) = 0. \tag{7}$$

In essence, the surrounding fluid imposes some extra mass onto the structure, or equivalently, the cylinder imparts part of its acceleration to the surrounding medium. The term, $\rho_f \pi r^2$ is therefore referred to as the "added mass". Note that no structural damping is considered in (7).

Coupled acoustic-structural analysis. Free vibration of a pipe in an acoustic medium can be solved numerically by the standard Galerkin discretization approach applied to the weak form of the fluid equation [Zienkiewicz et al. 2005]. The weak form representing the dynamics of the acoustic medium can be written as

$$d\Pi_f = \int_{\Omega_f} dp \left[\frac{1}{c^2} \ddot{p} - \nabla^2 p \right] d\Omega. \tag{8}$$

Equation (8) expands to the following equation once the appropriate boundary conditions specific to vibration of a pipe in an infinite acoustic medium are applied:

$$\int_{\Omega_f} \left[\delta p \frac{1}{c^2} \ddot{p} - (\nabla \delta p)^T (\nabla p) \right] d\Omega + \int_{\Gamma_1} \delta p \rho_f n^T \ddot{u} \, d\Gamma + \int_{\Gamma_2} \delta p \frac{1}{c} \dot{p} \Gamma. \tag{9}$$

The reader is referred to [Zienkiewicz et al. 2005] for derivation of the boundary conditions at the interface of solid-fluid (the second term) and the radiation boundary representing an infinite acoustic medium (the third term). In a similar manner, the weak form representing the pipe's response can be established.

To solve the above equations for a discrete domain, the displacement and the nodal acoustic pressure are approximated by

$$u = N_u \tilde{u},$$
$$p = N_p \tilde{p}. \tag{10}$$

The discrete form of the structural and acoustic domains can be represented as

$$M \ddot{\tilde{u}} + C \dot{\tilde{u}} + K \tilde{u} - Q \tilde{p} + F = 0 \tag{11}$$

and

$$S\ddot{\tilde{p}} + \widetilde{C}\dot{\tilde{p}} + H\tilde{p} + \rho_f Q^T \ddot{\tilde{u}} = 0, \tag{12}$$

where

$$
\begin{aligned}
Q &= \int_{\Gamma_t} N_u^T \boldsymbol{n} N_p \, d\Gamma, \\
S &= \int_{\Omega_f} N_p^T \frac{1}{C^2} N_p \, d\Omega, \\
\widetilde{C} &= \int_{\Gamma_2} N_p^T \frac{1}{C} N_p \, d\Gamma, \\
H &= \int_{\Omega_f} (\nabla N_p)^T \nabla N_p \, d\Omega.
\end{aligned}
\tag{13}
$$

Free vibration of the coupled system could then be represented by the matrices

$$
\begin{bmatrix} M & 0 \\ \rho_f Q^T & S \end{bmatrix} \begin{bmatrix} \ddot{\tilde{u}} \\ \ddot{\tilde{p}} \end{bmatrix} + \begin{bmatrix} K & -Q \\ 0 & H \end{bmatrix} \begin{bmatrix} \tilde{u} \\ \tilde{p} \end{bmatrix} = 0. \tag{14}
$$

It should be noted that the force and damping terms present in the original equations (i.e., (11) and (12)) have been ignored in the above equation; the only damping mechanism is, therefore, due to the radiant energy loss. Note that the above equation is not a standard eigenvalue equation (i.e., the type with symmetric matrices); a simple method proposed by Ohayon [1979] could, however, convert it to a standard eigenvalue problem.

Numerical study. This section provides details of the numerical models developed for investigating the vibration response of submerged pipes. The models have been developed in ABAQUS. The eigenvalues of the pipe obtained via the two theories described in the preceding sections are compared. An API-5L X65 steel pipe, commonly used for offshore oil and gas transportation, is considered in this study. The pipe's dimensions and mechanical properties are listed in Table 1. Figure 2 illustrates the cross-section of the submerged pipe modeled via the two approaches. The pipe was modeled with C3D20R elements in ABAQUS (i.e., three-dimensional 20-node reduced integration continuum elements with three translational degrees of freedom per node). Fully restrained boundary conditions (clamped) were assigned to both ends of the pipe by restricting the translational degrees of freedom at the corresponding nodes.

A mesh convergence study, conducted on the pipe, tuned the mesh density to obtain an acceptable convergence level with respect to the computed natural frequencies of interest. Accordingly, a total of 1600 elements connected by 2460 nodes make up the pipe.

elastic modulus (GPa)	206	length (mm)	2000
Poisson's ratio	0.3	outer diameter (mm)	168.3
density (kg/m^3)	7850	wall thickness (mm)	11
yield strength (MPa)	450		

**Table 1.** Mechanical properties and dimensions of the pipe.
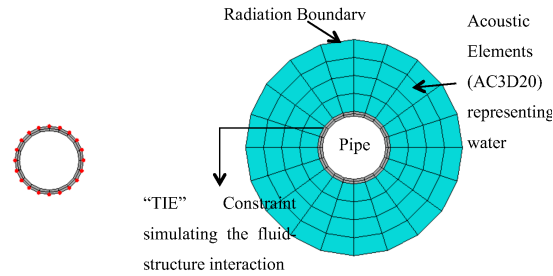
Figure 2. The submerged pipe's models. Left: the added mass approach. Right: the coupled acoustic-structural approach.

As for the first approach, using (7), the total added mass was determined to be 44.36 kg. This mass was evenly distributed on the outer surface of the pipe along its length via lumped masses assigned to the corresponding nodes, as shown in Figure 2, left.

Alternatively, the water surrounding the pipe could be modeled by AC3D20 elements (acoustic three-dimensional 20-node elements with one degree of freedom per node) in ABAQUS. The density and bulk modulus of the fluid must be defined as the material properties for the acoustic element. The corresponding values for water were taken as 997 kg/m^3, and 2.13 GPa, respectively. In addition, the boundary conditions had to be defined on both the acoustic-structural interfaces and infinite boundaries. Hence, a surface-based "TIE" constraint, defined as the interface region, was implemented in the model to simulate the coupling between the pipe and water by correlating the pipe's outer surface nodal displacements to the neighboring water elements' pressure degrees of freedom. Moreover, a radiation boundary was attributed to the exterior boundaries of water to approximate the infinite boundary; this scheme facilitated the transmission of the acoustic waves across the boundaries with little reflection of energy back into the acoustic domain. It should be noted that the reflection from the boundary becomes negligible once the boundary is located far enough from a vibrating structure; Figure 2, right, elucidates these details.

It should also be noted that the extent of the distance that should be included within an acoustic domain in order for the solution to converge efficiently when analyzing various types of problems (i.e., eigenvalue, steady state dynamic, or transient analyses) has been a controversial subject. To overcome this dilemma, the eigenvalues of a submerged pipe in a scaled depth of water were carefully investigated in our study. As such, the performances of the two boundaries as shown in Figure 3 were assessed,
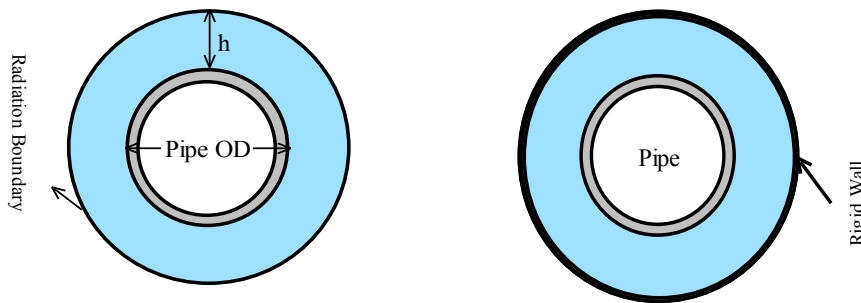
Figure 3. A submerged pipe with radiation (left) and rigid wall (right) boundaries.
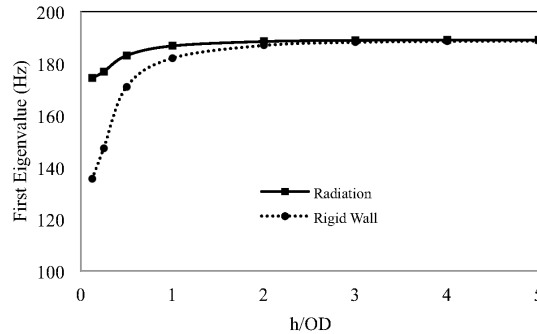
Figure 4. Convergence of the first eigenvalue.

and the results are shown in Figure 4. As can be seen, the first eigenvalue of the pipe converges to a constant value after a certain depth (distance), regardless of the type of the assigned boundary conditions. It is therefore concluded that there would be an effective water level (EWL) beyond which the reflection from the far-field boundary would become negligible. Accordingly, it was determined that modeling the surrounding water to a certain radius (in this case, $h/\text{OD} = 4$) would ensure the convergence of the first six eigenvalues, which are the main focus of this research. It should, however, be highlighted that the EWL may vary significantly depending on the intensity of disturbance caused by the nature of the load(s) within a given analysis (i.e., transient or steady-state dynamic analysis).

Results and discussion. Table 2 compares the eigenvalues of the submerged pipe obtained via the two approaches. The results reveal a noticeable difference in estimation of the third eigenvalue (21% difference) while the variation among the other five eigenvalues is limited to approximately 2%.

The third eigenvalue corresponds to the first torsional mode of the pipe. In this mode, the pipe exchanges almost no energy with the surrounding water. Therefore, it is expected for the torsional modes to yield the same eigenvalues as if the pipe was in the air. The CASA could correctly simulate this condition while, on the other hand, the AMA failed to predict the eigenvalues corresponding to the

Mode	m	n	Pipe in air	Submerged pipe AMA	CASA	% difference between AMA and CASA
1	bending		230.8	187.4	189	0.85
2	bending		580.7	471.5	478.4	1.45
3	torsion		789.9	627.0	789.9	20.60
4	bending		1033.2	838.5	855.4	1.98
5	1	2	1081.1	889.17	907	1.97
6	2	2	1126.5	926.3	947	2.20

m: number of longitudinal half-waves
n: number of circumferential waves [Ustundag 2011]
AMA: added mass approach
CASA: coupled acoustic-structural approach

Table 2. Comparison of the eigenvalues obtained from the AMA and CASA.

torsional modes accurately. A careful examination of the derivation of the added mass term (presented on page 106) reveals that, in that formulation, the velocity potential has been formulated based on the assumption that a submerged pipe would only vibrate in the lateral direction [Blevins 2001]. Hence, the discrepancy associated with this approach is minimized only when the bending modes are dominant, and the contribution of the torsional modes could be ignored.

Based on the above findings, the following recommendation is offered if a successful numerical simulation of a submerged pipeline, in the context of VB-SHM, is desired.

As stated earlier, the AMA has been formulated based upon the consideration of only the lateral vibration of pipes. Therefore, frequency-based VB-SHM approaches that only interrogate the bending eigenvalues of submerged pipes can reliably utilize AMA. However, the accuracy of signal-based (energy-based) VB-SHM approaches could be adversely affected due to the contribution of the torsional, circumferential, and longitudinal mode shapes in the vibration response of a given pipe. For instance, when a submerged pipe is excited by ambient vibration, all mode shapes of the pipe can contribute to its vibration whereas, in the case of an applied impact force perpendicular to the pipe's longitudinal axis, the contribution from the torsional and longitudinal mode shapes becomes relatively negligible in a pipe's vibration response. In addition, the AMA inherently includes other simplification that may cause discrepancies between the results produced by it and those of experiments or real-life situations. The simplifications include the negligence of compressibility and the energy dissipation mechanism induced by the fluid-structure interaction. It should be noted that, in [Razi and Taheri 2014], the authors reported a close agreement between the CASA's prediction of the flexural eigenvalues and the experimentally evaluated ones for a submerged pipe. Consequently, the use of the CASA is recommended when considering the VB-SHM of offshore pipelines.

Effect of operational variability on the accuracy of submerged structures' VB-SHM

In general, any change in the internal or external pressure of a pipe would change its overall stiffness, consequently affecting its vibration response [Rao 2011]. In this case, the equation for free vibration of a pipe is given by

$$M\ddot{\tilde{u}} + C\dot{\tilde{u}} + (K_G + K)\tilde{u} = 0. \tag{15}$$

The stiffness introduced by the external loads is called the "geometric stiffness", K_G [Cook 1995]. In the case of a submerged pipeline, the internal fluid's pressure or the external hydrostatic pressure would affect the apparent stiffness of the pipe, thereby changing the pipe's eigenvalues and dynamic response.

In VB-SHM techniques, deviations in the eigenvalues or dynamic response of a structure are attributed to the initiation of damage within the structure. Any variation in the geometric stiffness (which in turn alters the eigenvalues) of the structure during a VB-SHM trial could cause false alarms. In the case of a submerged pipeline, such variations could be developed by a sudden drop in the internal fluid's pressure or variation in the depth of submergence (which affects the magnitude of the external hydrostatic pressure).

This section investigates the effect of such operational variability on the eigenvalues and dynamic response of submerged steel and composite pipes. For this purpose, eigenvalues of the pipes when subject to various combinations of internal and external pressures are evaluated. The external pressure on the pipes was varied between 0 to 3 MPa to account for the variable hydrostatic pressure experienced
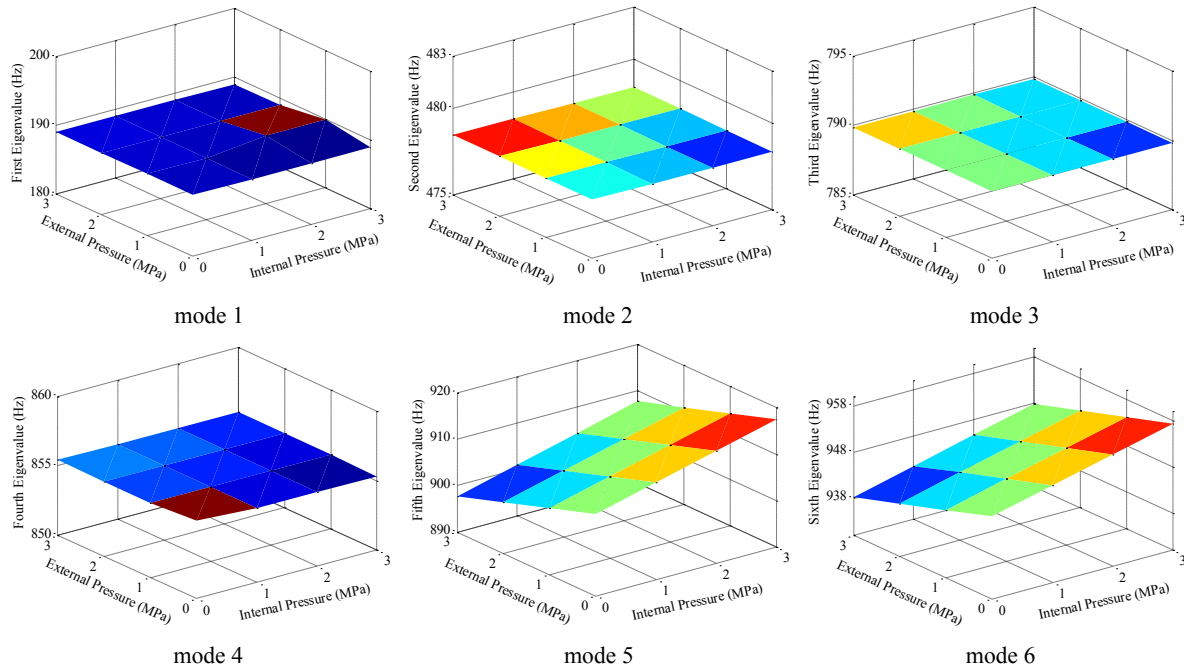
Figure 5. Variation in the eigenvalues of the submerged steel pipe due to varying external and/or internal pressures (buckling pressure (P_{cr}) = 392 MPa): mode 1 (bending), mode 2 (bending), mode 3 (torsional), mode 4 (bending), mode 5 ($m = 1$, $n = 2$), and mode 6 ($m = 2$, $n = 2$), where m is the number of longitudinal half-waves and n is the number of circumferential waves [Ustundag 2011].

by the pipes as the depth of submergence varies between 0 to 300 m. The internal pressure was assumed to vary between 3 to 0 MPa to simulate an internal pressure drop of 3 MPa.

Effect of operational variability on pipes' eigenvalues. The steel pipe described in the previous section was first considered and modeled using the CASA scheme. Figure 5 shows the variation of the submerged pipe's eigenvalues due to the external and/or internal pressures. As can be seen, variations in the eigenvalues corresponding to bending and torsional modes are negligible. However, the mode shapes with longitudinal and circumferential waves (see Figure 6) experienced a maximum of 2% variations in their eigenvalues.

The increase in the external pressure (in the presence of a constant internal pressure) causes a decrease in the eigenvalues of the latter modes while the internal pressure acts in an opposite fashion. The reason is postulated to be because the latter modes include local deformations; therefore, the geometric stiffness, K_G, produced by the internal pressure increases the total stiffness of the pipe, hence providing more resistance against formation of circumferential and longitudinal waves. The external pressure, however, decreases the overall stiffness of the pipe, thereby facilitating the appearance of local deformations. In summary, the geometric stiffness, K_G, developed as a result of the applied external and/or internal pressures would have a greater effect on the overall stiffness of the latter modes (the fifth and sixth modes).
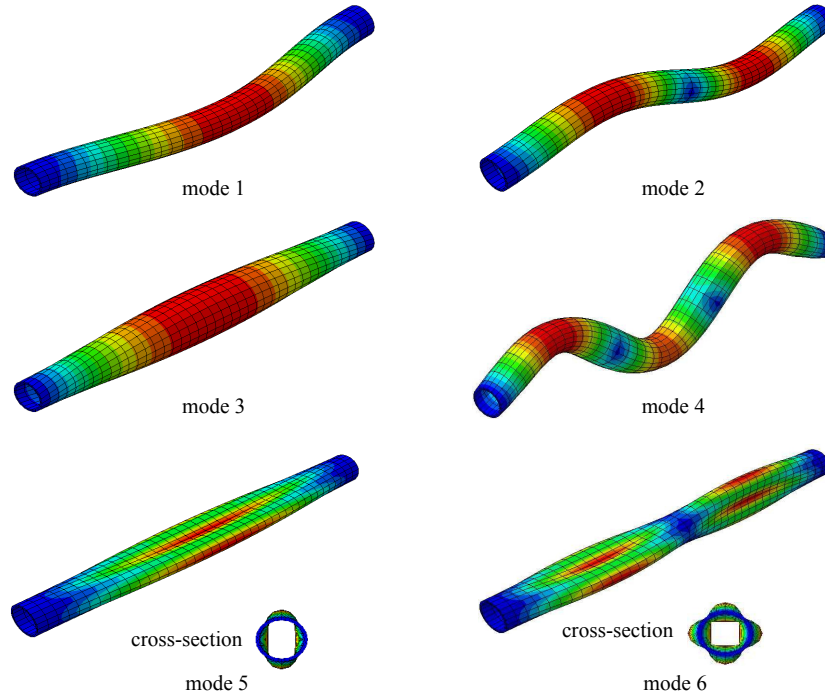
Figure 6. The first six eigenmodes of the steel pipe: mode 1 (bending), mode 2 (bending), mode 3 (torsional), mode 4 (bending), mode 5 ($m = 1$, $n = 2$), and mode 6 ($m = 2$, $n = 2$), where m is the number of longitudinal half-waves and n is the number of circumferential waves [Ustundag 2011].

To examine the effect of the geometric stiffness on pipes' eigenvalues further, two submerged pipes made of fiber-reinforced plastic composites (FRPC) were also considered. One pipe was made of carbon/epoxy and the other was an E-glass epoxy pipe. The lay-up configuration, dimensions, and mechanical properties of the composite pipes are given in Table 3. The pipes were modeled with the S4R element of ABAQUS (i.e., a four-node doubly curved thin or thick shell with finite membrane strains and reduced integration with the hourglass control option). Fully restrained boundary conditions (clamped) were assigned to both ends of the pipe by restraining the translational and rotational degrees of freedom

|	Pipe 1	Pipe 2		Carbon/epoxy	E-glass/epoxy
material	carbon/epoxy	E-glass/epoxy	E_{11} (GPa)	138	38.6
length	2	2	E_{22} (GPa)	8.96	8.27
outer diameter	0.1467	0.1545	ν_{12}	0.30	0.26
wall thickness	0.0036	0.0075	G_{12} (GPa)	7.10	4.14
lay-up	$[90/\pm45]_{3,s}$	$[90/\pm45]_{5,s}$	ρ (kg/m^3)	1600	1800

Table 3. Dimensions and lay-up of the FRP pipes (m) as well as mechanical properties of composite materials.
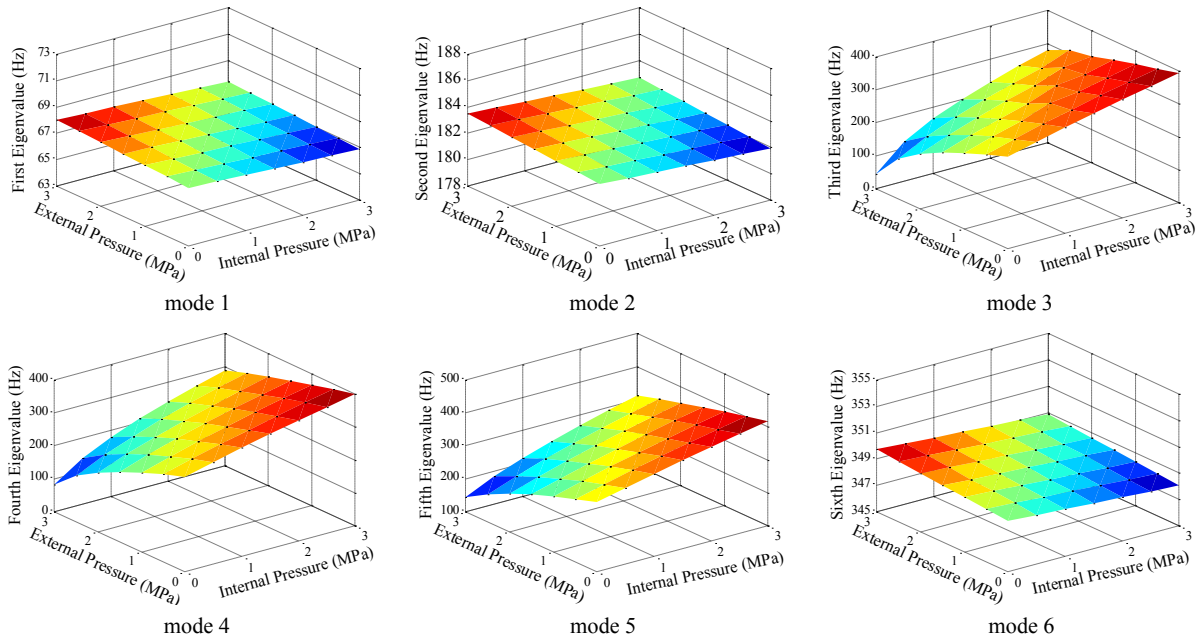
Figure 7. Variation in the eigenvalues of the submerged carbon/epoxy pipe varying due to external and/or internal pressures (design pressure = 15 MPa): mode 1 (bending), mode 2 (bending), mode 3 ($m = 1$, $n = 2$), mode 4 ($m = 2$, $n = 2$), mode 5 ($m = 3$, $n = 2$), and mode 6 (bending), where m is the number of longitudinal half-waves and n is the number of circumferential waves [Ustundag 2011].

of the corresponding nodes. A mesh convergence study was conducted for the pipes based on evaluating the pipes' natural frequencies with the criterion of yielding an acceptable convergence level of 95% with respect to the theoretical values. Accordingly, a total of 800 elements connected by 820 nodes were used to construct the pipe. The surrounding water domain was constructed by 8000 acoustic elements (AC3D8) connected by 9020 nodes.

The lay-up sequence for each pipe was selected such that the pipes could sustain a design pressure of 15 MPa (external/internal) with the same safety factor based on the Hashin damage criterion. Figures 7 and 8 illustrate the variations in the FRPC pipes' eigenvalues against the internal and/or external pressures. As seen, similar to the results obtained from the previous eigenvalue analysis, the bending and torsional modes' eigenvalues of the FRPC pipes experience negligible variations upon applying the net external and internal pressures. The internal pressure generates an effective compressive axial force (see Figure 9), which causes a decrease in the lateral stiffness of the pipe, thereby reducing the eigenvalues corresponding to the bending modes [DNV 2006]. Conversely, the external pressure generates an effective tensile axial force, thereby increasing the eigenvalues corresponding to the bending modes. The other modes' eigenvalues undergo significant variations upon applying the external and/or internal stresses. The trend in variation is also similar to what was observed for the steel pipe. However, the rate of increase/decrease in the eigenvalues is more severe in the case of the FRPC pipes. For instance, the third mode ($m = 1$, $n = 2$) of the FRPC pipe made of carbon/epoxy experiences 84% change in its eigenvalues (i.e., from 280
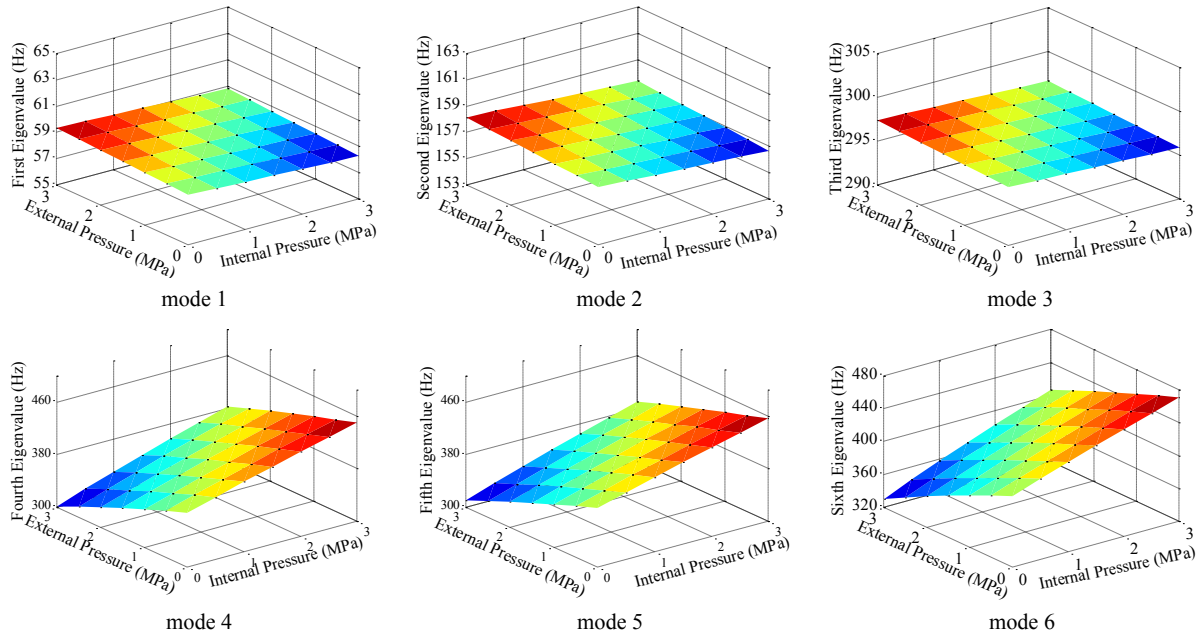
Figure 8. Variation in the eigenvalues of the submerged E-glass/epoxy pipe due to varying external and/or internal pressures (design pressure = 15 MPa): mode 1 (bending), mode 2 (bending), mode 3 (bending), mode 4 ($m = 1$, $n = 2$), mode 5 ($m = 2$, $n = 2$), and mode 6 ($m = 3$, $n = 2$), where m is the number of longitudinal half-waves and n is the number of circumferential waves [Ustundag 2011].

to 44 Hz) as the external pressure increases to 3 MPa (assuming an internal pressure of 0 MPa). For the FRPC pipe made of E-glass/epoxy, however, the variation in the eigenvalues is less severe. For instance, under the same loading condition, the corresponding mode's ($m = 1$, $n = 2$) eigenvalue undergoes 21% reduction (i.e., from 383 Hz to 301 Hz).

These observations imply that the variation in geometric stiffness produced by the presence of the external loads has variably affected the overall stiffness of the FRPC pipes. To explore this phenomenon further, the local stiffness (bending rigidity) of the FRPC pipes was calculated based on the classical laminate theory (CLT) according to the equation [Weisshaar and Foist 1985]

$$\text{EI} = b\left(D_{11} - \frac{D_{12}^2}{D_{22}} \right). \tag{16}$$
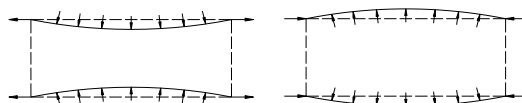
Figure 9. Free body diagrams of the pipe with clamped-clamped boundary conditions. Left: pipe under external pressure. Right: pipe under internal pressure.

FRP carbon/epoxy	98 Pa·m^4
FRP E-glass/epoxy	427 Pa·m^4
Steel pipe	2318 Pa·m^4

**Table 4.** Bending rigidity (EI) of the FRP and steel pipes.

Table 4 compares the regional bending rigidity of the two FRPC pipes and the steel pipe described in the previous section. The bending rigidity of the pipe made of E-glass/epoxy (wall thickness of 0.0075 m) is approximately four times that of the carbon/epoxy pipe (with wall thickness of 0.0036), which justifies the rate of reduction in the investigated modes' eigenvalue (i.e., 21% in contrast to 84% reduction in the eigenvalue of the mode ($m = 1$, $n = 2$) for the E-glass/epoxy and carbon/epoxy pipes, respectively). On the other hand, the relatively higher stiffness of the steel pipe explains the minor observed variations in the pipe's eigenvalues (i.e., approximately 2% in modes five ($m = 1$, $n = 2$) and six ($m = 2$, $n = 2$)).

The findings from this study can be summarized as follows.

- The accuracy of the frequency-based VB-SHM methods could be adversely affected by the presence of operational variability, depending on the stiffness of the pipe and the severity of variability.

- Accordingly, frequency-based VB-SHM of pipes with high stiffness (e.g., the steel pipe considered in this study) that are subject to operational variability could be successfully accomplished. On the other hand, the VB-SHM of less stiff pipes (such as the FRPC pipes considered in this study) should be conducted cautiously and diligently since their eigenvalues happen to be quite sensitive to the operational variation.

Effect of operational variability on the transient dynamic response of pipelines. The transient dynamic responses of pipes would also be affected as a result of a change in their stiffness. For instance, the same carbon/epoxy pipe examined earlier is subjected to an impact load in the form exhibited in Figure 10 under the conditions described in Figure 11. The pipe was impacted at 0.5 m from its left end, and the transient responses (i.e., acceleration (a_y), velocity (v_y), and displacement (d_y) time-histories) of a point along the pipe, located 0.6 m from the left end, were collected (see Figure 10). As can be seen in Figure 11, the existence of the external pressure (3 MPa) on the pipe tangibly alters the transient responses of the pipe, both in terms of the amplitude and energy.
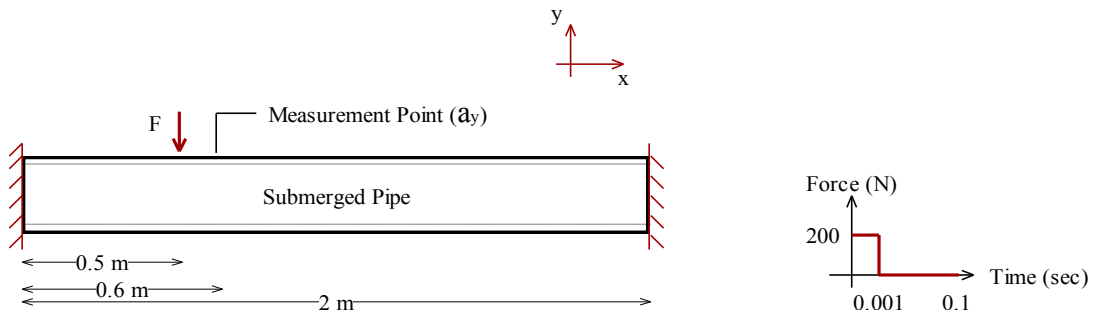
Figure 10. Left: schematic of the submerged pipe. Right: the transient applied load.
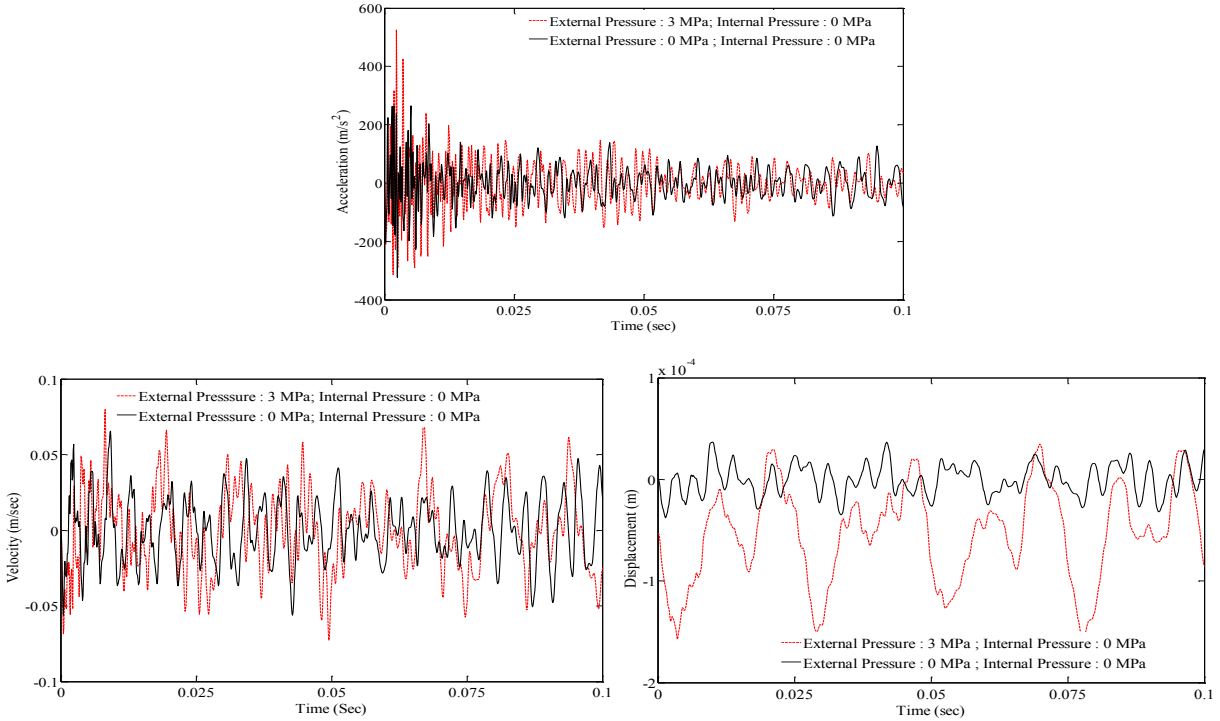
Figure 11. Acceleration (top), velocity (bottom left), and displacement (bottom right) time-histories of the selected point on the FRP pipe (made of carbon/epoxy) due to an impact load.

Several VB-SHM methods' damage-sensitive features are based on the time-domain vibration response of the system being monitored [Peng et al. 2012; Bao et al. 2013; 2011; Rezaei and Taheri 2010]. As demonstrated earlier, the vibration response of pipelines could be significantly affected as a result of operational variability (i.e., variation in either the internal fluid's pressure or external hydrostatic pressure or both). Neglecting such influential parameters could significantly affect the accuracy of VB-SHM methods. Therefore, since the SHM of interest to us is a coupled signal and vibration-based approach, it would be instructive to evaluate the degree of sensitivity of the methodology to such operational variability.

The VB-SHM technique that has been developed in our research group [Rezaei and Taheri 2010; Razi et al. 2013] is based on the examination of the energy of the first intrinsic mode function (IMF) of the time-domain vibration response of a given structure. This quantity is used as a damage-sensitive feature and is mathematically represented by the equation

$$E = \int_0^{t_0} (\text{IMF}\,1)^2 \, dt, \tag{17}$$

where t_0 is the signal duration. The IMFs of a typical vibration response can be obtained by applying the empirical mode decomposition (EMD), a signal-processing technique, to the time-domain vibration response of the system. Evaluation of the above term during a structures' service life enables detection
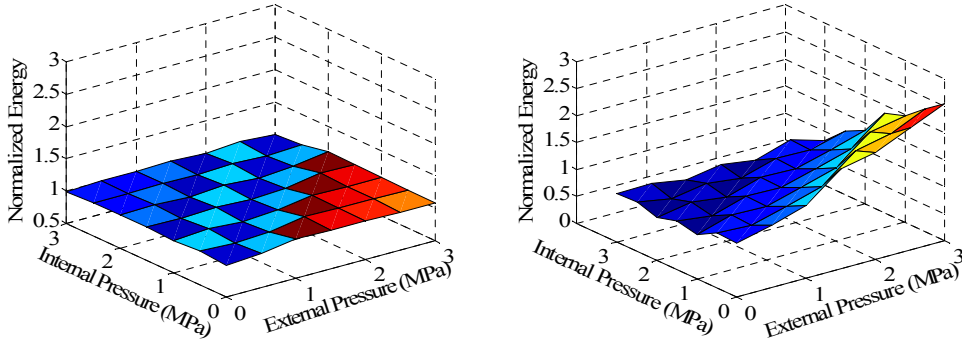
Figure 12. Variation in the energy of the acceleration time-history's first IMF as a function of external and internal pressures. Left: steel pipe. Right: FRPC (carbon/epoxy).

of damage within the structures by using the damage index formulation

$$\text{EMD\_EDI} = \left| \frac{E_{\text{healthy}} - E_{\text{damaged}}}{E_{\text{healthy}}} \right| \times 100, \tag{18}$$

where E_{healthy} and E_{damaged} correspond to the energy of the first IMF of the vibration response evaluated at the structure's healthy and damaged states. An index larger than 0 would indicate the presence of damage. As noted, however, the energy term, E, could be affected by the presence of operational variability, some of which was explained earlier, and the consequence could be false alarms in detection of damage.

To investigate the sensitivity of the EMD_EDI to the operational variability, the time-histories of the vibration responses of the FRPC and steel pipes due to an impact load (see Figure 10) were considered.

Figure 12 illustrates the variation of the energy term, E, for the steel pipe and the pipe with the lowest bending rigidity, namely FRPC (glass/epoxy), as a function of the applied external and internal pressures. Note that the values are normalized with respect to the energy of the pipes in their unpressurized state (i.e., $P_{\text{Internal}} = P_{\text{External}} = 0 \, \text{MPa}$).

The results indicate that the energy term corresponding to the steel pipe undergoes a very minor change (a maximum of 10%) over the entire pressure domain. In contrast, the FRPC pipe's vibration response shows considerable sensitivity to the variation in applied pressures (by as much as 150%). The sensitivity is believed to be because of the steel pipe's flexural stiffness, which was notably higher than the FRPC pipes' stiffness (see Table 4). As a result, the contribution of the geometric stiffness (K_G) to total stiffness was negligible in the case of the steel pipe. According to (18), the imposed variation in the energy of the pipes due to variation in the applied pressures could lead to false alarms in prediction of potential damages.

The authors [Razi and Taheri 2014] reported the result of a damage detection trial conducted on a submerged pipe based on the evaluation of the energy term described above (i.e., E). They considered SHM of a propagating notch in the girth-weld of two mating pipes. The notably large values of damage index reported in this study (i.e., from 25%, corresponding to the notch at 1 mm deep, up to 150% when the notch depth propagated to 4 mm) suggests that the result of damage detection on the steel pipe would remain insensitive to the disturbance caused by the variation in the external or internal pressure

considered in this study. On the other hand, SHM of pipes with relatively low bending rigidity (e.g., the carbon/epoxy pipe examined here) could lead to false alarms in the presence of such disturbance.

The results from this part of the study can be summarized as follows.

- When investigating the health of an offshore pipeline, the integrity of the energy-based (or signal-based) VB-SHM methodologies could be greatly affected depending by the pipe's stiffness and the extent of variation in the external and internal pressures that the pipe would experience during a VB-SHM trial.

- The VB-SHM of stiff submerged pipes (e.g., the steel pipe considered in this study) using the EMD_EDI method can be accomplished with a good level of confidence and accuracy. This accuracy would be met, provided the pipe experiences a sudden drop in its internal pressure (up to 3 MPa according to this study's result) or when the depth of submergence changes within 300 m (i.e., 3 MPa change in the external pressure). The results of the EMD_EDI method applied to less stiff pipes (i.e., the FRPC composite pipes considered here) indicate that SHM of such pipes would be a challenging task. This is mainly due to the fact that their vibration response could undergo a significant change under imposed operational variability.

Concluding remarks

The performance and accuracy of the two widely used approaches for modeling the dynamic response of submerged structures (namely, the "added mass" and "coupled acoustic-structural" approaches) in the context of VB-SHM were investigated. The investigation included the evaluation of the eigenvalues of an offshore pipeline modeled by the two approaches. The differences were limited to below 2% in the lateral modes whereas for the torsional mode the differences approached 20%. The large discrepancy was attributed to the restrictive assumption involved in the formulation of the "added mass" approach. It was therefore recommended to adopt the coupled acoustic-structural approach to conduct successful VB-SHM of submerged structures.

Subsequently, the effect of operational variability on the accuracy of a VB-SHM of offshore pipelines was studied. Such operational variability could rise due to the change in the pressure of the fluid with which the pipe is pressurized or the change in the external hydrostatic pressure upon submergence of the pipe in various depths. For this purpose, vibration response of a steel and two FRPC composite pipes was examined against incremental variations in the internal and external pressures. Our findings can be summarized as follows.

- The accuracy of VB-SHM of pipes could be adversely affected by operational variability. The adverse impact would be a function of the stiffness of the pipe.

- Accordingly, it was determined that VB-SHM of the steel pipe considered in this study could be successfully conducted under the examined operational variability. On the other hand, the VB-SHM trial should be conducted with diligence for less stiff pipes such as the FRPC composite pipes considered in this study as their vibration response showed notable sensitivity to the operational variability.

List of symbols

b	width	N_u	shape functions for displacement
C	speed of sound in the medium	N_p	shape functions for acoustic pressure
C	damping matrix	p_s	static pressure
$\widetilde{C}$	damping matrix for fluid	p	dynamic/acoustic pressure
D_{ij}	bending stiffness elements	$\tilde{p}$	acoustic pressure vector
E_{ij}	elastic moduli	Q	coupling matrix
EI	bending rigidity	r	radius
F	force vector	S	mass matrix for fluid
g	acceleration due to gravity	U	velocity in lateral direction
G_{ij}	shear moduli	u	displacement vector
h	height of the fluid	$\tilde{u}$	nodal displacements vector
H	stiffness matrix for fluid	V	velocity
OD	outer diameter	$X(t)$	displacement in x-direction
K	stiffness per unit length	Ω_f	fluid domain
K_G	geometric stiffness matrix	Γ_i	boundary domain
M	mass per unit length	ρ_f	fluid density
M	mass matrix	ϕ	velocity potential
n	unit normal vector	ν_{ij}	Poisson's ratio

Acknowledgements

References

[Bao et al. 2011] C.-X. Bao, H. Hao, and Z.-X. Li, "Vibration-based damage detection of pipeline system by HHT method", *Applied Mechanics and Materials* **99–100** (2011), 1067–1072.

[Bao et al. 2013] C.-X. Bao, H. Hao, and Z.-X. Li, "Vibration-based structural health monitoring of offshore pipelines: numerical and experimental study", *Structural Control and Health Monitoring* **20**:5 (2013), 769–788.

[Blevins 2001] R. D. Blevins, *Flow-induced vibration*, 2nd ed., Krieger, Malabar, FL, 2001.

[Cengel and Cimbala 2006] Y. A. Cengel and J. M. Cimbala, *Fluid mechanics: fundamentals and applications*, McGraw-Hill, New York, 2006.

[Chen et al. 2010] J. Chen, Z. Su, and L. Cheng, "Identification of corrosion damage in submerged structures using fundamental anti-symmetric Lamb waves", *Smart Materials and Structures* **19**:1 (2010), 015004.

[Cook 1995] R. D. Cook, *Finite element modeling for stress analysis*, Wiley, New York, 1995.

[DNV 2006] "Free spanning pipelines", recommended practice DNV-RP-F105, Det Norske Veritas, 2006, Available at http://exchange.dnv.com/publishing/codes/docs/2006-02/RP-F105.pdf.

[Kramer et al. 2013] M. R. Kramer, Z. Liu, and Y. L. Young, "Free vibration of cantilevered composite plates in air and in water", *Composite Structures* **95** (2013), 254–263.

[Na and Kundu 2002] W.-B. Na and T. Kundu, "Underwater pipeline inspection using guided waves", *Journal of Pressure Vessel Technology* **124**:2 (2002), 196–200.

[Ohayon 1979] R. Ohayon, "Symmetric variational formulation of harmonic vibrations problem by coupling primal and dual principles. Application to fluid-structure coupled systems", *La Recherche Aérospatiale* **3** (1979), 207–211.

[Peng and Hao 2012] X.-L. Peng and H. Hao, "A numerical study of damage detection of underwater pipeline using vibration-based method", *International Journal of Structural Stability and Dynamics* **12**:3 (2012), 1250021.

[Peng et al. 2012] X.-L. Peng, H. Hao, and Z.-X. Li, "Application of wavelet packet transform in subsea pipeline bedding condition assessment", *Engineering Structures* **39** (2012), 50–65.

[Rao 2011] S. S. Rao, *Mechanical vibrations*, 5th ed., Prentice Hall, Upper Saddle River, NJ, 2011.

[Razi and Taheri 2014] P. Razi and F. Taheri, "A vibration-based strategy for health monitoring of offshore pipelines' girth-welds", *Sensors* **14**:9 (2014), 17174–17191.

[Razi et al. 2013] P. Razi, R. A. Esmaeel, and F. Taheri, "Improvement of a vibration-based damage detection approach for health monitoring of bolted flange joints in pipelines", *Structural Health Monitoring* **12**:3 (2013), 207–224.

[Rezaei and Taheri 2010] D. Rezaei and F. Taheri, "Health monitoring of pipeline girth weld using empirical mode decomposition", *Smart Materials and Structures* **19**:5 (2010), 055016.

[Rizzo et al. 2010] P. Rizzo, J.-G. Han, and X.-L. Ni, "Structural health monitoring of immersed structures by means of guided ultrasonic waves", *Journal of Intelligent Material Systems and Structures* **21**:14 (2010), 1397–1407.

[Ross et al. 2007] C. T. F. Ross, P. Köster, A. P. F. Little, and G. Tewkesbury, "Vibration of a thin-walled prolate dome under external water pressure", *Ocean Engineering* **34**:3–4 (2007), 560–575.

[Ustundag 2011] B. Ustundag, *On the free vibration behavior of cylindrical shell structures*, master's thesis, Massachusetts Institute of Technology, Cambridge, MA, 2011, Available at http://hdl.handle.net/1721.1/67717.

[Weisshaar and Foist 1985] T. A. Weisshaar and B. L. Foist, "Vibration tailoring of advanced composite lifting surfaces", *Journal of Aircraft* **22**:2 (1985), 141–147.

[Zeinoddini et al. 2012] M. Zeinoddini, G. A. R. Parke, and S. M. Sadrossadat, "Free-spanning submarine pipeline response to severe ground excitations: water-pipeline interactions", *Journal of Pipeline Systems Engineering and Practice* **3**:4 (2012), 135–149.

[Zhu et al. 2008] X. Q. Zhu, H. Hao, and X.-L. Peng, "Dynamic assessment of underwater pipeline systems using statistical model updating", *International Journal of Structural Stability and Dynamics* **8**:2 (2008), 271–297.

[Zienkiewicz et al. 2005] O. C. Zienkiewicz, R. L. Taylor, and J. Z. Zhu, *The finite element method: its basis and fundamentals*, 6th ed., Butterworth–Heinemann, Oxford, 2005.

[Zou et al. 2005] G. P. Zou, N. Cheraghi, and F. Taheri, "Fluid-induced vibration of composite natural gas pipelines", *International Journal of Solids and Structures* **42**:3–4 (2005), 1253–1268.

PEJMAN RAZI: Pejman.razi@dal.ca
Department of Civil and Resource Engineering, Dalhousie University, 1360 Barrington Street, Halifax, NS B3H 4R2, Canada

FARID TAHERI: farid.taheri@dal.ca
Department of Civil and Resource Engineering, Dalhousie University, 1360 Barrington Street, Halifax, NS B3H 4R2, Canada

∎msp

NONUNIQUENESS AND INSTABILITY OF CLASSICAL FORMULATIONS OF NONASSOCIATED PLASTICITY, I: CASE STUDY

THOMAS PUČIK, REBECCA M. BRANNON AND JEFFREY BURGHARDT

A dynamic instability, which is relatively unexplored in the literature despite having been long ago previously asserted to exist for any conventional nonassociated plastic flow model, is illustrated by means of an example problem. This instability is related to a condition known as achronicity, in which the wave speed in plastic loading is greater than that in elastic unloading (making it absolutely not related to the well-studied phenomena of localization and flutter). The one-dimensional example problem initializes an elastic-plastic half-space to a initially quiescent uniform state of prestress that places it in an achronic condition if a nonassociated flow rule is used. The initial stress state is perturbed by an axial stress pulse applied at the surface. The problem is first solved analytically for the case of constant wave speeds, and it is shown to possess a two-parameter family of nonunique solutions. These solutions are unstable in that both the amplitude and the width of the propagating pulse increase linearly with time. The case-study problem technically represents spontaneous motion from a quiescent state, but it does not violate thermodynamics (as the energy driving the instability is available from elastic stored energy of the initial prestress). The example problem is additionally solved numerically for both constant and nonconstant plastic wave speeds, where the instability is observed in either case. Furthermore, it is shown that neither the constant nor the nonconstant wave speed solution converges with mesh refinement, which therefore represents a numerical inadmissibility associated with the underlying loss of uniqueness of solution. It is the nonuniqueness of the unstable solution, not the existence of the instability itself, that is of primary concern. Unlike conventional localization instability, this achronic instability is not yet known to be a real phenomenon. This case-study problem illustrates the need for novel laboratory testing methods sufficient to determine if the instability is truly physical, or merely an anomalous shortcoming of classical nonassociated plasticity formulations. Some guidance for appropriate laboratory testing is presented, with emphasis on why such testing is highly nontrivial as a result of irreducible uncertainty in direct validation of a regular flow rule.

1. Introduction

Plastic flow is said to be nonassociated if the plastic strain increments are not normal to the yield surface in stress space. This type of flow is of particular interest in applications involving geological materials, which often exhibit apparent nonassociated behavior in quasistatic laboratory tests. Nonassociated flow rules are also employed quite frequently in numerical simulations, because associated flow rules appear to significantly over-predict the amount of plastic dilatation for most materials [Spitzig et al. 1975; 1976; Lade et al. 1987; Shen et al. 2012], and because (by allowing a simple radial return for such materials) they are easier to implement than associated flow rules. In this century, it has been shown that a conventional associated flow rule also cannot describe the anisotropic behavior of rolled sheet metal [Stoughton 2002;

Cvitanic et al. 2008; Mohr et al. 2010; Taherizadeh et al. 2010]. Gao et al. [2011] have shown that a nonassociated flow rule more accurately describes the behavior of aluminum under a variety of loading conditions, but their loading conditions did not include the type of loading that we explore in this paper. Somewhat more recent work [Desmorat and Marull 2011; Dunand et al. 2012; Besse and Mohr 2012] has shown that a nonassociated flow rule is not necessary to describe the anisotropic plasticity of rolled sheet metal if other plasticity features are included.

The models discussed above are macroscopic phenomenological models, which do not directly account for a material's complex microstructure. Rousselier et al. [2012] have shown that in the case of metals plasticity, microstructural based models, which have a more complex formulation not compatible with classical macroscale phenomenological plasticity frameworks, are better suited to describe the complex evolution of a material undergoing plastic flow. Alternatives to traditional plasticity models are discussed and examined in more detail in the companion (part II) paper.

An assertion that nonassociated flow may stimulate instability and/or nonuniqueness is certainly not new, but the particular case of so-called "achronicity" (in which plastic stiffness exceeds elastic stiffness) seems to have been relatively unexplored in comparison to unrelated phenomena such as localization or flutter associated with a zero, negative, or complex plastic acoustic eigenvalue. Early initial concerns about achronicity were motivated by the observation that with nonassociated flow, it is possible to find closed loading cycles for which useful energy could be extracted from the material and the system of forces acting on it. This was first pointed out by Drucker [1949; 1950] for closed stress cycles, and later by Il'Yushin [1961] for closed strain cycles. This is not a violation of conservation of energy, since the released energy is merely liberated from stored strain energy associated with the ambient initial prestress. The major concern was that this might lead to an unstable release of energy under some conditions. However, no specific (and generally applicable) mechanisms for causing such unstable energy releases to occur were identified in this early work. For a more detailed discussion of these and other concerns about insufficient substantiation of a nonassociated flow rule (which is not tantamount to ruling it out altogether), see Brannon [2007].

The first concrete example of an actual plastic instability was a strain localization instability first identified by Rudnicki and Rice [1975]. This particular form of instability was found to result from a softening-like behavior caused by nonassociated flow. Rudnicki and Rice showed that, with nonassociated flow, this type of instability can occur even for positive values of the hardening modulus under certain conditions. With associated flow, on the other hand, it was shown that it can occur only for negative values of the hardening modulus (i.e., by putting explicit strain softening into the material model).

Another form of instability related to nonassociated plastic flow is called the flutter instability, first identified by Bigoni [1995]. The strain localization instability and the flutter instability result from the fact that the elastic-plastic tangent stiffness tensor loses positive definiteness when the yield function and flow potential function are not coincident. Strain localization is a result of the occurrence of a negative acoustic eigenvalue, whereas the flutter instability corresponds to complex eigenvalues. The "achronic" state, discussed in this paper, corresponds to *positive* plastic acoustic eigenvalues — but with a plastic eigenvalue being larger than any of the elastic eigenvalues, hence implying plastic wave speeds exceeding elastic wave speeds. For a complete derivation of conditions for all possible magnitudes of plastic wave speeds relative to elastic speeds, see Brannon and Drugan [1993].

Sandler and Rubin [1987], as well as Sandler and Pučik [1993], investigated the fundamentally different form of instability that has been virtually ignored in comparison to now-ordinary localization or flutter. The mechanism underlying this instability is, in many respects, the diametrical opposite of the softening mechanism investigated by Rudnicki and Rice. That is, it is found that nonassociated flow can also lead to excessive *stiffening* under certain conditions. This can cause the incremental modulus (and hence the wave speed) of the material to be greater in plastic loading than it is in elastic unloading. Under these loading conditions the eigenvalues of the tangent operator remain real and positive.

Sandler and Rubin used a simple case-study problem to show that this wave speed inversion, which is referred to in this paper as *achronicity*, is a dynamically unstable condition in that, when it occurs, there always exist loading paths for which the solution to the equations of motion becomes unstable in the sense that both the amplitude and width of a finite stress wave, no matter how small, grows without bound as it propagates into material at yield. This phenomenon is essentially spontaneous motion from a quiescent state, but not necessarily a violation of thermodynamics, since energy to drive the instability could come from elastic prestress.

The question remains, however, whether or not it is possible to observe such behavior in the laboratory. This paper (or its companion, part II) encourages such efforts by describing the expected character of achronic material response and its sensitivity to details of the flow rule. Additionally, Sandler and Rubin demonstrated that, for their simple case-study problem, the governing equations admit multiple solutions and are thus ill posed, which has significant implications for numerical modeling. In this paper, any instability that arises from achronicity is referred to as the Sandler–Rubin instability.

Unlike the localization and flutter instabilities, the Sandler–Rubin instability has been shown to emerge only under a specific class of initial boundary-value problems where both the elastic unloading and the elastic-plastic loading branch of the constitutive operator are exercised. Therefore, this instability is fundamentally different from the other instabilities mentioned in that it does not arise directly from the plastic flow itself.

Stoughton and Yoon [2008] have asserted that Sandler and Rubin's analysis is invalid since their solutions "do not generally solve the dynamic equations of motion unless the components of the constitutive models are such that the slope of the stress-strain relation, the gradient of the plastic potential and the gradient of the yield function are constant for a finite perturbation." The (flawed) rationale for this assertion is that "if C_L [the wave speed in plastic loading] is not constant to first order in the time step, then it is easy to see that the solution [the Sandler–Rubin solution] does not solve the equations of motion for any finite time step $\Delta t > 0$." It is true that Sandler and Rubin's solution becomes invalid for the case of nonconstant wave speeds, but that is because the *solution itself is specifically for the case of constant wave speeds* (more correctly, the solution is for piecewise constant wave speeds, depending on the plastic state of the wave characteristic). Almost as a tautology, the solution of problem should never be expected to apply without revision to cases that violate the original solution's assumptions. Since the assumption of a constant wave speed (a consequence of assuming nonhardening plasticity and linear elasticity) was made in the derivation of Sandler and Rubin's analytical solutions, one would not expect those solutions to solve the equations of motion under other conditions. This would be akin to deriving an elasticity solution while assuming a constant elastic modulus, then attempting to substitute a nonconstant elastic modulus into the resulting solution. It would be an enormous coincidence if the resulting expression still satisfied the governing equations. The fact that Sandler and Rubin's constant-wave-speed solution

does not solve the equations of motion for nonconstant wave speeds does not rule out the possibility of a similar instability and nonuniqueness in the nonlinear case (which has no analytical solution, to our knowledge). The present paper seeks to substantiate this point through a counterexample by solving a problem similar to the one solved by Sandler and Rubin, but with the addition of nonlinear hardening, which results in nonconstant plastic wave speeds but does not eliminate the instability or its associated nonuniqueness.

To our knowledge, only two studies have attempted to investigate the existence of this instability experimentally. In the first of these, Lade et al. [1987] performed a set of quasistatic triaxial compression tests using sand to investigate any possible instabilities arising from a violation of Drucker's postulate. The study found that no instabilities were observed even for loading directions which produce a negative inner product of the stress rate and plastic strain rate tensors. However, instability was defined in that work as "gross collapse". The Sandler–Rubin instability discussed in this paper is actually the result of a stiffening of the material, which (if real) might manifest as unstable waves that grow so slowly in amplitude that they can be quenched from boundary release waves before inducing "gross collapse". Thus, Lade's observations neither confirm nor rule out a Sandler–Rubin instability.

More recently, Brannon et al. [2009] conducted an extensive suite of quasistatic triaxial compression measurements within the loading regime where Sandler and Rubin's analysis would predict instability. As with Lade's study, no evidence of instability was observed, but the data were not extensive enough to firmly rule out a Sandler–Rubin instability either. Whether or not the Sandler–Rubin instability is actually a nonphysical mathematical anomaly remains unclear, as it has eluded direct laboratory efforts to date.

At least within classical plasticity formulations that neglect elastic-plastic coupling and other sources of so-called phantom nonassociativity [Brannon 2007], it can be proved mathematically that having a plastic flow direction different from the direction of the yield surface normal implies existence of loading modes for which achronicity occurs [Sandler and Pučik 1993; Brannon and Drugan 1993], even for infinitesimal strain increments. This includes any nonassociated material obeying the Prandtl–Reuss flow rule, which is the basis for the "radial return" algorithms employed in many of the material models used in numerical simulations (primarily because it is very easy to implement). Accordingly, one would expect achronicity to be very common in numerical simulations. Yet, nonassociated flow rules have been used in numerical calculations for more than three decades, and in most cases it is difficult to identify any obvious ill effects in the numerical results. A number of factors may account for achronic instability being subtle enough to miss despite being present in a simulation:

(1) Achronic instabilities are fairly weak, with growth rates that are typically only linear with time. Unlike exponential runaways, for example, they don't usually call attention to themselves by crashing a code through excessive deformation leading to "gross collapse".

(2) At least in our case-study simulations, achronic instabilities don't leave easily recognized signatures, such as the shear bands one typically gets with strain localization instabilities. The residual effects are much more spread out, and easily masked in complex problems.

(3) Achronic instabilities always entail characteristic deformation modes, most of which are three-dimensional, and hence are artificially disallowed in two-dimensional calculations. This situation is analogous to a 1-D bar compression simulation being incapable of manifesting a buckling instability.
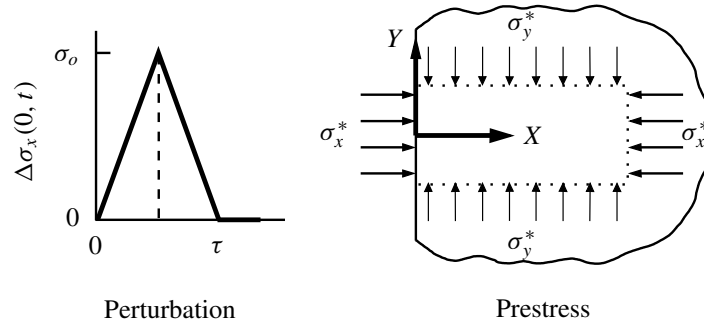
Figure 1. Geometry, loading, and coordinate system in the example problem.

(4) Nonuniqueness is very difficult to detect in numerical calculations. Even if many solutions are possible, a digital computer will always give one and only one answer. When nonuniqueness is associated with instability, nonconvergence and other forms of mesh sensitivity are typical symptoms of ill-posedness of governing equations.

Moreover, achronic instabilities weren't even known to exist until fairly recently. Most analysts have been (and still are) unfamiliar with their features, and may not be aware of what to look for, thus motivating this work. The purpose of part I of this paper is to illustrate some of these features by means of an example problem. Part II of this paper discusses possible ways that the instability may be influenced or eliminated altogether. The example problem is designed to be simple enough so that the effects of instability and nonuniqueness can easily be isolated, highlighted, and independently confirmed by any researcher with access to simple nonassociated plasticity codes (provided that the software allows a nonzero initial stress).

2. Problem description

In this section we present an example problem that exhibits achronicity. This problem is designed to be the simplest possible that exhibits achronicity. The primary reason for choosing such a simple problem is to allow an analytical solution to be derived. Examining achronicity via an analytical solution allows the nature of the instability and nonuniqueness to be made clear. Based solely on the simple example problem presented here it cannot be ruled out that the instability or nonuniqueness might be eliminated under a more complex model, but there is no reason to believe that the example presented here represents a special case. More complex models will be explored in part II. Despite its simplicity, the problem presented here is physically plausible and uses a model that is a member of a widely used class of traditional plasticity models. The parameters used in the problem are within typical ranges for geologic materials.

The example is a one-dimensional problem of an elastic/plastic half-space that is initially quiescent, but in a uniform state of prestress placing it in an achronic condition, which is subsequently perturbed by an axial stress pulse applied at the surface. The geometry, loading, and coordinate system are illustrated in Figure 1. The material properties and initial stress state, denoted by σ_{ij}^*, are chosen so that achronicity is satisfied with respect to longitudinal wave propagation in the x-direction.

The applied axial stress perturbation $\Delta\sigma_x(0, t)$ at the surface is a triangular pulse designed to produce plastic loading followed by elastic unloading.[1] Because the material is in an achronic state, the loading ramp travels faster than the unloading ramp as the pulse propagates to the right. This causes the two ramps to separate, which has two important consequences. First, the pulse width increases with time. Second, the region between the two ramps, which initially consists of just a single point (the apex of the triangle), opens up into a finite region. The solution in this region is indeterminate in that it is not dictated by either the initial or the boundary conditions, as is normally the case in well-posed initial/boundary value problems for hyperbolic equations. As a result, the solution in this region is unstable and nonunique.

In the following discussion, the example problem is analyzed both analytically and numerically. First, an analytical solution similar to Sandler and Rubin's is derived assuming perfect plasticity, which results in a constant plastic wave speed. For this case, it is shown that it is possible to derive a two-parameter family of nonunique solutions to this problem. These solutions are also shown to be unstable in that both the width and the amplitude of the pulse increase linearly with time. The constant-plastic-wave speed problem is then analyzed numerically using the finite-element method, and the results are shown to be consistent with the analytical solutions in the sense that the numerical solutions appear to belong to the infinite set of nonunique analytical solutions.

The problem is also solved numerically using a nonlinear hardening law, which results in a nonconstant plastic wave speed. For both the constant and nonconstant wave speed case, it is shown that the numerical solution does not converge as the mesh is refined, but that the numerical solution becomes more noticeably unstable with mesh refinement. Specifically, the instability magnitude grows even as the time step is reduced to values much lower than that required for ordinary Courant time integrator stability. This lack of convergence with mesh refinement is, we believe, the result of the ill-posedness of the underlying equations of motion. The link between ill-posed governing equations and nonconvergence of numerical solutions has been likewise well established for other — *but unrelated* — sources of ill-posedness such as localization (cf. [de Borst et al. 1993]).

We begin the discussion of the Sandler–Rubin case study by first completing the problem definition, and demonstrating that achronicity does indeed exist for the specified material properties and initial state.

2.1. *Material properties.* Except as discussed below, the material properties are based on representative values for limestone rock. The elastic properties are taken as

$$\rho = 2500\,\text{kg/m}^3,$$
$$E = 30\,\text{GPa},$$
$$\nu = 0.25,$$

where ρ is the mass density, E is Young's modulus, and ν is Poisson's ratio. For the *analytical* solution, only ideal linearized plasticity is assumed. Section 5 shows that *numerical* solutions, including both linear and nonlinear hardening, likewise exhibit the same general characteristics as the analytical solution

---

[1]The first leg of this axial stress pulse is tensile in the sense that it causes a reduction in the compressive stresses relative to their prestress values. Even though the first leg of this pulse reduces the stresses (in absolute value), it is referred to as "loading" because it induces plastic flow. The second leg, which increases the stress magnitude, is termed an unloading leg because it corresponds to elastic deformation driving the final stress state to a point inside the yield surface.

(namely, instability and nonconvergence, which is symptomatic of nonuniqueness/ill-posedness of the governing equations in the presence of achronicity).

To construct the simplest possible case study exhibiting achronistic instability, the yield surface is taken to be of Drucker–Prager form,

$$f(\boldsymbol{\sigma}) = \sqrt{J_2} + \alpha I_1 - k = 0, \tag{1}$$

where $I_1 = \mathrm{Tr}(\boldsymbol{\sigma})$ is the first invariant of the stress tensor, and $J_2 = \frac{1}{2}\boldsymbol{S} : \boldsymbol{S}$ is the second invariant of the deviatoric stress tensor $\boldsymbol{S}$. Stresses are taken to be positive in tension, so the preconfinement stresses (defined below) will be negative. The values for the constant material parameters, α and k, are in a typical range for limestone:

$$\alpha = 0.315,$$
$$k = 5.066\,\mathrm{MPa}.$$

These values correspond to a friction angle of 40° and a cohesion of 4.5 MPa.[2]

The flow rule, typical of what is adopted in engineering applications of phenomenological rock plasticity, is

$$\dot{\boldsymbol{\epsilon}}^p = \dot{\lambda}\widehat{\boldsymbol{M}}, \tag{2}$$

where $\dot{\lambda}$ is the magnitude of the plastic strain rate tensor, and $\widehat{\boldsymbol{M}}$ is a second-order unit tensor in the direction of the gradient of the plastic potential function

$$g(\boldsymbol{\sigma}) = \sqrt{J_2} + \alpha_p I_1. \tag{3}$$

If α_p is chosen to be equal to α, then the flow rule is said to be associated. The solutions hereafter presented are for the case when $\alpha_p = 0$, which corresponds to the Prandtl–Reuss flow rule.

2.2. *Initial and boundary conditions.* The region is initially quiescent but in a uniform state of pre-stress, $\boldsymbol{\sigma}^*$, which is a state of conventional triaxial compression in the x-direction. The values for the initial state are taken as

$$\sigma_x^* = -100.00\,\mathrm{MPa}, \tag{4}$$
$$\sigma_y^* = \sigma_z^* = -17.55\,\mathrm{MPa}, \tag{5}$$

and zero shear stress. Noting that these values are both negative, this initial stress is in a state of compression. For the assumed values of α and k, this state is on the yield surface defined by (1).

---

[2]The friction angle, ϕ, and cohesion, c, are related to the constants α and k. However, there is more than one definition that may be used. The one assumed in this discussion is based on a conventional triaxial compression loading condition, which results in the following expressions:

$$\alpha = \frac{2\sin\phi}{\sqrt{3}(3 - \sin\phi)} \quad \text{and} \quad k = \frac{6c\cos\phi}{\sqrt{3}(3 - \sin\phi)}.$$
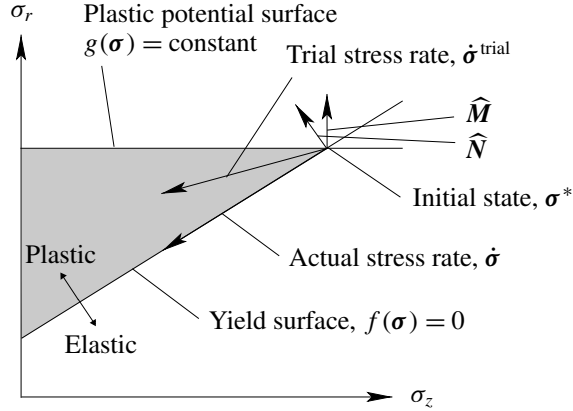
Figure 2. Illustration of the initial state with the yield surface, defined by $f(\boldsymbol{\sigma}) = 0$, and plastic flow potential isosurface $g(\boldsymbol{\sigma})$ shown in the meridional profile defined by Lode stress invariants ($\sigma_r = \|\boldsymbol{S}\|$ and $\sigma_z = -\text{Tr}(\boldsymbol{\sigma})/\sqrt{3}$, which are similar to the q and p invariants commonly used in geomechanics, but scaled to make this plot isomorphic to stress space). $\widehat{\boldsymbol{M}}$ is the direction of the plastic strain rate, which is normal to the plastic flow potential isosurface. The vector labeled $\dot{\boldsymbol{\sigma}}^{\text{trial}}$ is defined to be the elastic stiffness acting on the total strain rate, which is the stress rate that would result if the material response were elastic under the same total strain rate. The vector labeled $\dot{\boldsymbol{\sigma}}$ is the actual stress rate, which remains on the yield surface.

The axial stress perturbation (applied at the surface of the half-space) is a triangular pulse characterized by a peak axial stress σ_o and a pulse duration τ, as illustrated in Figure 1. The values for these quantities are taken as

$$\sigma_o = 10\,\text{MPa} \tag{6}$$

and

$$\tau = 2\,\text{ms}. \tag{7}$$

Since σ_o is positive, this perturbation is actually tensile (i.e., it slightly reduces the initial precompression). Accordingly, the motion at the surface is initially outward (to the left) followed by a restoring motion that is inward (to the right).

2.3. *Loading in stress space.* The initial state and the elastic perturbation are illustrated in Figure 2, as viewed in the meridional (constant Lode angle) plane of the isomorphic stress invariants. The principal stresses σ_1, σ_2, and σ_3 correspond to the actual stresses σ_{xx}, σ_{yy}, and σ_{zz}, respectively.

The trial elastic stress rate $\dot{\boldsymbol{\sigma}}^{\text{trial}}$ is defined to be the elastic stiffness acting on the total strain rate tensor.[3] For a stress state at yield, a loading increment is plastic if and only if the trial elastic stress rate

---

[3]The trial elastic stress rate is not generally equivalent to the so-called "test" elastic stress rate that corresponds to a purely elastic solution consistent with boundary conditions. As pointed out by Brannon [2007], the two are equivalent only under conditions of prescribed strain (as is the case in constitutive models called by finite element codes, where traction boundary conditions are enforced as explicit contributions to the boundary integral of the weak form of the equations of motion, not as stress constraints in the constitutive model).

has a positive inner product with the normal to the yield surface. Figure 2 shows that plastic loading (for a nonassociative model like this one) does not require the trial elastic stress rate to have a positive inner product with the flow direction. In particular, our case study is specifically designed to be a uniaxial-strain wave-propagation problem for which the axial stress rate at the boundary generates a *trial* stress rate pointing into the shaded wedge in Figure 2, which is above the yield surface (hence plastic) but below the flow surface. The direction of trial elastic stress rate, cast as a vector in principal stress space, is determined from the fact that the deformation mode associated with the perturbation is a uniaxial strain increment in the x-direction, which implies the following relationship between the lateral and axial elastic increments:

$$\dot{\sigma}_2^{\text{trial}} = \dot{\sigma}_3^{\text{trial}} = \frac{\nu}{1-\nu}\dot{\sigma}_1^{\text{trial}}, \tag{8}$$

where ν is Poisson's ratio. This determines the direction of $\dot{\boldsymbol{\sigma}}^{\text{trial}}$ to within a sign. The sign is determined by demanding that $\dot{\boldsymbol{\sigma}}^{\text{trial}}$ be directed outward from the yield surface, so that the response is plastic rather than elastic. As seen in Figure 2, this requires $\dot{\sigma}_1^{\text{trial}}$ to be positive, which corresponds to a tensile axial stress increment. The magnitude of $\dot{\boldsymbol{\sigma}}^{\text{trial}}$ is set by requiring the axial stress perturbation $\dot{\sigma}_1^{\text{trial}}$ to equal 10 MPa (as selected in (6)).

By design, and as can be seen in Figure 2, the trial elastic stress perturbation falls within the shaded, wedge-shaped region above the yield surface but below the plastic potential surface. This type of loading causes work done on the material in a closed strain cycle to be negative — i.e., the material does net positive work on its surroundings [Sandler and Rubin 1987; Sandler and Pučik 1993]. As might be expected, there is a close relationship between negative work and achronicity. Unfortunately, this relationship is difficult to demonstrate in general due to the complexity of the deformation modes typically needed to induce it. These loading paths are generally difficult to attain in the laboratory as well [Brannon et al. 2009], and always involve nonproportional loading. However, for the special case of longitudinal wave propagation considered in the example problem, it can easily be seen. Because the deformation mode in this case is uniaxial strain in both loading and unloading, it is easily shown that the work ΔW done in a closed strain cycle $\pm\epsilon_1$ is given by

$$\Delta W = -\tfrac{1}{2}(M_L - M_U)(\Delta\epsilon_1)^2, \tag{9}$$

where M_L and M_U are the constrained moduli[4] in loading and unloading, respectively. Accordingly, it follows that $\Delta W < 0$ if and only if $M_L > M_U$. In other words, negative net work in this closed strain cycle will occur if the modulus (and hence the wave speed) in loading is greater than that in unloading. The values of the moduli and wave speeds are derived in the next section, and it is shown that this condition is, in fact, satisfied for the example problem.

From Figure 2, it is also apparent that, for the type of loading considered in this problem, plastic loading (i.e., a trial stress rate pointing above the yield surface) actually corresponds to physical unloading (i.e., a reduction in the magnitude of stress). The elastic unloading phase (which has a trial stress rate pointing below the yield surface) actually corresponds to physical loading (i.e., an increase in the magnitude of stress). In this paper (unless otherwise indicated), "loading" and "unloading" always refer to plastic loading and elastic unloading relative to the yield surface. As previously indicated, plastic loading for this case study occurs during a stress-releasing increment.

---

[4]i.e., slopes of the axial stress-strain plot in uniaxial strain conditions.

3. Proof of achronicity

This section demonstrates that the case study's initial state and specified boundary loading conditions induce an achronistic condition (where plastic stiffness exceeds elastic stiffness). The loading and unloading wave speeds, c_L and c_U, are given by

$$c_L = \sqrt{M_L/\rho}, \tag{10}$$

$$c_U = \sqrt{M_U/\rho}, \tag{11}$$

where M_L and M_U are the constrained moduli in loading and unloading and ρ is the mass density. For the unloading (elastic) case, the constrained modulus is given by the well-known expression

$$M_U = \frac{E(1-\nu)}{(1+\nu)(1-2\nu)}, \tag{12}$$

where E is Young's modulus and ν is Poisson's ratio.

To derive an equivalent expression for M_L, consider a uniaxial strain increment de_1 in the plastic loading (i.e., tensile) direction, with all other incremental strain components being zero. The volume strain increment $d\epsilon_{ii}$ is then given by $d\epsilon_{ii} = d\epsilon_{ii}^e + d\epsilon_{ii}^p = d\epsilon_1$. However, for the Prandtl–Reuss flow rule ($\alpha_p = 0$), the plastic volume strain increment $d\epsilon_{ii}^p$ is zero. Accordingly, the constitutive relation governing the elastic volume change can be written as

$$d\epsilon_1 = \frac{1-2\nu}{E}(d\sigma_1 + 2d\sigma_2), \tag{13}$$

which has used the fact that $d\sigma_2 = d\sigma_3$.

An additional constraint is provided by the fact that, during plastic flow, the stress state remains on the yield surface. As illustrated in Figure 2, this implies a linear relationship between the axial and lateral normal stress increments, $d\sigma_1$ and $d\sigma_2$. Using (1), this relationship is given by

$$d\sigma_1 = \frac{1-\sqrt{3}\alpha}{1+2\sqrt{3}\alpha}d\sigma_2, \tag{14}$$

where we have again exploited the fact that $d\sigma_2 = d\sigma_3$. Substituting (14) into (13) then leads to an incremental relationship of the form

$$d\sigma_1 = M_L d\epsilon_1, \tag{15}$$

where

$$M_L = \frac{E}{3(1-2\nu)}(1 + 2\sqrt{3}\alpha), \tag{16}$$

which is the desired expression for the loading modulus. Using a finite-element code that supports this simple nonassociated model, single-element uniaxial-strain testing of a closed strain path from the prestressed state will easily confirm both of these formulas for the loading and unloading moduli (as well as negative net work for a closed strain path). Such verification testing is an essential prerequisite before attempting to solve the more complicated wave-propagation problem (cf. Kamojjala et al. 2015).

The loading and unloading moduli and wave speeds for the example problem with the Prandtl–Reuss flow rule can be computed using (10), (11), (12) and (16), together with the previously specified material

properties. The values that are obtained are

$$M_L = 41.8\,\text{GPa}, \quad c_L = 4.09\,\text{km/s},$$
$$M_U = 36.0\,\text{GPa}, \quad c_U = 3.79\,\text{km/s}.$$

As seen, the loading modulus is sixteen percent greater than the unloading modulus, and the loading wave speed is eight percent greater than the unloading wave speed. Although the difference in the wave speeds may seem small, it will be shown in the next section that if there is *any* degree of achronicity at all, no matter how small, it can lead to arbitrarily large instabilities for this case study.

From (12) and (16), it is seen that $M_L > M_U$ if and only if

$$\alpha > \frac{1 - 2\nu}{\sqrt{3}(1 + \nu)}. \tag{17}$$

For $\nu = 0.25$, this corresponds to $\phi > 30°$. Accordingly, for friction angles below this value, achronicity does not occur for longitudinal plane wave propagation with this particular flow rule. It can be shown that achronicity itself does still occur for many other modes of plane wave propagation, but the deformation modes that are involved are much more complex and multidimensional. The main reason for choosing a relatively high friction angle (40 degrees) for the example problem was to allow some of the features of achronicity to be illustrated with a deformation mode that is as simple as possible (uniaxial strain in both loading and unloading).
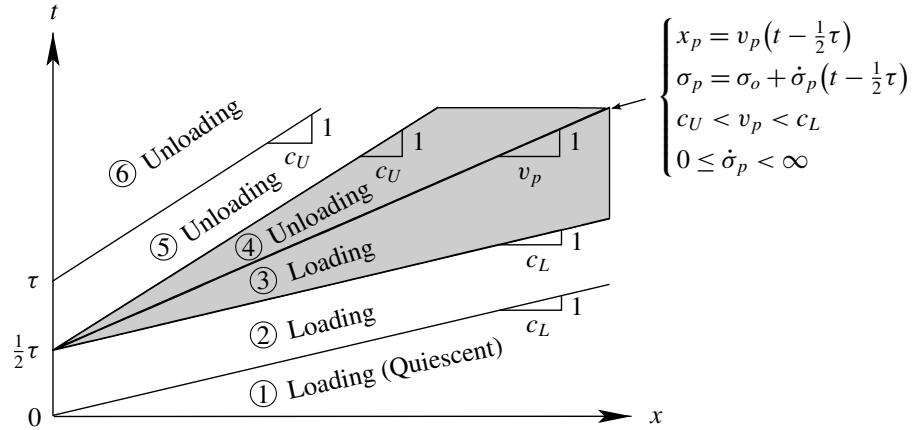
4. Analytical solutions

In this section, we show that the example problem can be solved analytically, resulting in infinitely many possible solutions. This is done by first deriving a family of solutions having two independent free parameters. The nonunique and unstable nature of these solutions is then illustrated by considering some example solutions chosen from this family.

One of the consequences of nonuniqueness is that there are many possible *families* of solutions having different functional forms. In the following discussion, we focus on only one such family, with a specific assumed functional form. Accordingly, the example solutions that are presented are not necessarily representative of all possible solutions, but merely sufficient to demonstrate nonuniqueness. However, as will later be seen, the features of these solutions are very similar to those of the numerical verification simulations in Section 5.

4.1. *Derivation.* The approach is similar to the one employed by Sandler and Rubin [1987]. We begin by first dividing the (x, t) plane into six regions, as illustrated in Figure 3. The boundaries of these regions are characteristics, along which the stress is constant in time. With perfect plasticity or linear hardening, all of the characteristics form straight lines in the (x, t) plane whose slope is equal to the wave speed. With nonlinear hardening the characteristics for plastic loading are no longer straight lines since the wave speed is no longer constant. The case of nonconstant plastic wave speed will be discussed in Section 5.

In each region, the material is assumed to be undergoing either plastic loading or elastic unloading, as indicated in the figure. (Note that region 1, which is the quiescent region ahead of the pulse, could be taken as either loading or unloading; for definiteness, we label it to be loading.)

Figure 3. Regions in the (x, t) plane employed in constructing an analytical solution. The difference between the loading and unloading wave speeds is exaggerated for clarity. The shaded region is where the solution is nonunique.

Within each region, i, the equations of motion in the x-direction can then be expressed as

$$\rho \frac{\partial v}{\partial t} = \frac{\partial \sigma}{\partial x}, \tag{18}$$

$$\frac{\partial \sigma}{\partial t} = \rho c_i^2 \frac{\partial v}{\partial x}, \tag{19}$$

$$c_i = \begin{cases} c_L & \text{if } i = 1, 2, 3, \\ c_U & \text{if } i = 4, 5, 6, \end{cases} \tag{20}$$

where $\sigma(x, t)$ and $v(x, t)$ represent the changes in axial stress and velocity in the x-direction due to the perturbation, and are defined by

$$\sigma(x, t) = \sigma_{xx}(x, t) - \sigma_x^*, \tag{21}$$

$$v(x, t) = v_x(x, t). \tag{22}$$

As illustrated in the figure, region 2 represents the portion of the (x, t) plane swept out by the loading ramp propagating at the loading wave speed, c_L. Similarly, region 5 represents the portion swept out by the unloading ramp propagating at the unloading wave speed, c_U. Because $c_L > c_U$, the loading ramp travels faster than the unloading ramp, which causes the two ramps to separate. As noted earlier, this has two important consequences. The first is that the pulse width increases linearly with time. (The reason for this is readily apparent from the figure.) The second is that the region between these two ramps, which initially consists of a single point, opens up into a finite region (the region indicated by the shaded area). The solution in this region is indeterminate in that it is not dictated by either the initial conditions or the boundary conditions, as is normally the case for well-posed initial/boundary value problems for hyperbolic equations. As a result, it is unstable and nonunique. Another useful way of thinking about the origin of the nonuniqueness in this region is that there is no characteristic information in this region, making the wave speed indeterminate. A nearly identical phenomenon is well known to occur for other hyperbolic equations such as a rarefaction Riemann problem with the inviscid Burger's equation. In that

case and ours, there are multiple ways to construct characteristics for the region in question, resulting in multiple solutions. For details, see [LeVeque 1992, p. 28] and [Thomas 1999, p. 82].

Here we demonstrate one method of filling in the missing characteristic information in the shaded region of Figure 3. To do this we have divided the separated (shaded) region into two regions shown in the figure. In region 3, the material is assumed to undergo continued loading, while in region 4 it is assumed to be unloading. Accordingly, the boundary between the two regions represents the path followed by the peak axial stress perturbation in the (x, t) plane. The position and value of the peak axial stress perturbation are assumed to be given by

$$x_p(t) = v_p\big(t - \tfrac{1}{2}\tau\big), \tag{23}$$

$$\sigma_p(t) = \sigma_o + \dot{\sigma}_p\big(t - \tfrac{1}{2}\tau\big), \tag{24}$$

where $t \geq \tfrac{1}{2}\tau$, and where v_p and σ_p represent the propagation velocity and time rate of change of the peak axial stress perturbation, respectively. The latter two quantities are both assumed to be constant, and are treated as free parameters, subject only to the following restrictions:

$$c_U < v_p < c_L, \tag{25}$$

$$0 \leq \dot{\sigma}_p < \infty. \tag{26}$$

Note that the first inequality implies that the dashed line must lie somewhere inside the shaded region, but the precise location within this region is arbitrary. The second inequality ensures that the axial stress perturbation along this line, σ_p, does not decrease with time; however, the rate of increase, $\dot{\sigma}_p$, may have an arbitrarily large positive value.

The preceding assumptions would normally be considered improper for well-posed initial/boundary value problems. For well-posed problems, the solution is uniquely determined by the field equations, initial conditions, and boundary conditions. Prescribing values for the solution along an arbitrary line in the (x, t) plane represents an over-specification, which usually results in the problem having no solution (except, of course, for the special case where the values that are prescribed happen to agree with the solution that would have been obtained anyway). However, because the solution to the example problem is nonunique, it will be seen that it is always possible to obtain a solution for this "over-specified" problem for any values of the free parameters, v_p and $\dot{\sigma}_p$, in the ranges given in the inequalities (25) and (26).

To demonstrate this, we begin by assuming that the solution in each region, i, can be expressed in the functional form

$$\sigma(x, t) = \sigma^{(i)}(x, t) = A_i x + B_i\big(t - \tfrac{1}{2}\tau\big) + D_i, \tag{27}$$

$$v(x, t) = v^{(i)}(x, t) = \frac{B_i}{\rho c_i^2}x + \frac{A_i}{\rho}\big(t - \tfrac{1}{2}\tau\big) + \frac{E_i}{\rho}, \tag{28}$$

where A_i, B_i, D_i and E_i are constants that are yet to be determined. Since these expressions are linear in x and t, the solution surfaces for σ and v, which can be visualized in the third dimension above the (x, t) plane, are composed of planar surfaces above each region. These surfaces are assumed to join continuously along the boundaries between the regions, but the partial derivatives may be (and typically are) discontinuous at the boundaries.

It is easily verified that the functional forms assumed in (27) and (28) automatically satisfy the field equations given in (18) and (19) within each region, i, for any values of the unknown coefficients A_i, B_i, D_i and E_i. Accordingly, the values of these coefficients are dictated by the various conditions that are specified, which can be summarized as follows:

Initial conditions:

$$\sigma(x, 0) = v(x, 0) = 0 \quad \text{for } 0 \leq x < \infty. \tag{29}$$

Boundary conditions:

$$\sigma(0, t) = \begin{cases} (2\sigma_o/\tau)t, & 0 \leq t \leq \frac{1}{2}\tau, \\ (2\sigma_o/\tau)(\tau - t), & \frac{1}{2}\tau \leq t \leq \tau, \\ 0, & \tau \leq t \leq \infty. \end{cases} \tag{30}$$

Peak axial stress condition:

$$\sigma(x, t) = \sigma_o + \dot{\sigma}_p\left(t - \frac{1}{2}\tau\right) \quad \text{on } x = v_p\left(t - \frac{1}{2}\tau\right), \ \frac{1}{2}\tau \leq t < \infty. \tag{31}$$

Continuity conditions:

$$\left.\begin{array}{l} \sigma^{(i+1)}(x, t) = \sigma^{(i)}(x, t) \\ v^{(i+1)}(x, t) = v^{(i)}(x, t) \end{array}\right\} \quad \text{on } x = v_b^{(i)}(t - t_b^{(i)}), \ t_b^{(i)} \leq t < \infty, \ i = 1, \ldots, 5. \tag{32}$$

Loading conditions:

$$\frac{\partial \sigma}{\partial t} \geq 0 \quad \text{for } i = 1, 2, 3, \qquad \frac{\partial \sigma}{\partial t} \leq 0 \quad \text{for } i = 4, 5, 6. \tag{33}$$

Consistent with (21), σ and v represent the changes in axial stress and velocity in the x-direction due to the applied perturbation. In (32), the quantity $v_b^{(i)}$ represents the propagation velocity of the boundary between regions i and $i + 1$, and $t_b^{(i)}$ represents its intercept on the t-axis, as illustrated in Figure 3. Also, the conditions given in the inequalities (33) ensure consistency with the assumption that the material is undergoing plastic loading in regions 1–3 and elastic unloading in regions 4–6.

Obtaining a solution to the above equations is straightforward but tedious, and a detailed derivation will not be given here. Instead, we simply state the solution, which is given by the set of coefficients shown in Table 1. It can be verified that these coefficients, the axial stress σ, and velocity v, defined in equations (27)–(28) satisfy (29)–(33) for any values of the free parameters v_p and $\dot{\sigma}_p$ in the ranges given by the inequalities (25)–(26). The existence of free parameters (having values not determined from the problem data) demonstrates that the governing equations have no unique solution. Following a few general observations about these solutions, the next subsection provides some representative examples illustrating the nonuniqueness and unstable nature of the solution.

As noted earlier, σ and v are continuous along the boundaries between regions, but their derivatives might be (and typically are) discontinuous. This so-called "weak" discontinuity does *not* violate any physical or mathematical law. In fact, similar propagating weak discontinuities would occur for a purely elastic material subjected to the same initial and boundary conditions. The equations of motion are satisfied in integral form across any control volume containing only weak discontinuities in stress and velocity (i.e., where σ and v themselves are both continuous; cf. Chapter 2 of [Drumheller 1998]).

| i	c_i	A_i	B_i	D_i	E_i
1	c_L	0	0	0	0
2	c_L	$-\dfrac{2\sigma_o}{c_L\tau}$	$\dfrac{2\sigma_o}{\tau}$	σ_o	$-\dfrac{\sigma_o}{c_L}$
3	c_L	$-\dfrac{\dot{\sigma}_p}{c_L-v_p}$	$\dfrac{c_L\dot{\sigma}_p}{c_L-v_p}$	σ_o	$-\dfrac{\sigma_o}{c_L}$
4	c_U	$\dfrac{(c_Lv_p+c_U^2)\dot{\sigma}_p}{c_L(v_p^2-c_U^2)}$	$-\dfrac{c_U^2(c_L+v_p)\dot{\sigma}_p}{c_L(v_p^2-c_U^2)}$	σ_o	$-\dfrac{\sigma_o}{c_L}$
5	c_U	$\dfrac{2\sigma_o}{c_U\tau}+\dfrac{(c_L-c_U)\dot{\sigma}_p}{cL(v_p+c_U)}$	$-\dfrac{2\sigma_o}{\tau}$	σ_o	$-\dfrac{\sigma_o}{c_L}$
6	c_U	$\dfrac{(c_L-c_U)\dot{\sigma}_p}{c_L(v_p+c_U)}$	0	0	$\dfrac{(c_L-c_U)\sigma_o}{c_Lc_U}$

Table 1. Coefficients in the analytical solution.

One interesting difference between this case and the elastic case is that, in the elastic case (governed by the simple wave equation), discontinuities in derivatives can propagate only along characteristic lines in the (x, t) plane, the slope of which is uniquely determined from material properties. However, in the above solution, the discontinuity at the location of the peak stress propagates along a line that does *not* correspond to a characteristic of either the loading properties or unloading properties, but is somewhere in between. Such behavior is impossible with the simple wave equation, and may seem suspicious at first glance. The reason that it is possible here is that the material properties at any point on this line are undefined (or, more precisely, they are double-valued, and depend on which region one approaches the point from). A similar observation applies for ordinary associative elastic-plastic materials, but with the crucial difference that associativity of the flow rule ensures uniqueness of the velocity of the peak stress point, v_p. Such uniqueness is not the case for nonassociated flow rules.

It is also possible to derive an analytical solution for the case in which the perturbation applied to the surface of the region consists of a triangular *velocity* pulse rather than a triangular axial stress pulse. The form and features of this solution are very similar to those of the example problem discussed here, with one notable difference. With an axial stress pulse, the external forces may continue to do work on the region after the pulse is completed if the front surface has a nonzero velocity (which it generally does). However, with a velocity pulse, the external forces do no work after the pulse is completed, and the ambient forces (those associated with the prestress σ_{ij}^*) do no net work during the pulse. Accordingly, for purposes of illustrating the overall energy balance, a velocity pulse is actually more desirable than a stress pulse. The main reason for choosing a stress pulse for the example problem is that it provides a better illustration of some of the unusual characteristics of the nonassociated material response.

4.2. *Example solutions.* Example solutions corresponding to three different choices of the free parameters v_p and $\dot{\sigma}_p$ are illustrated in Figures 4, 5, and 6. The value of v_p is the same in all three cases (3.98 km/s), while $\dot{\sigma}_p$ ranges over three different values (0, 0.15, and 0.25 MPa/ms). For each case, the
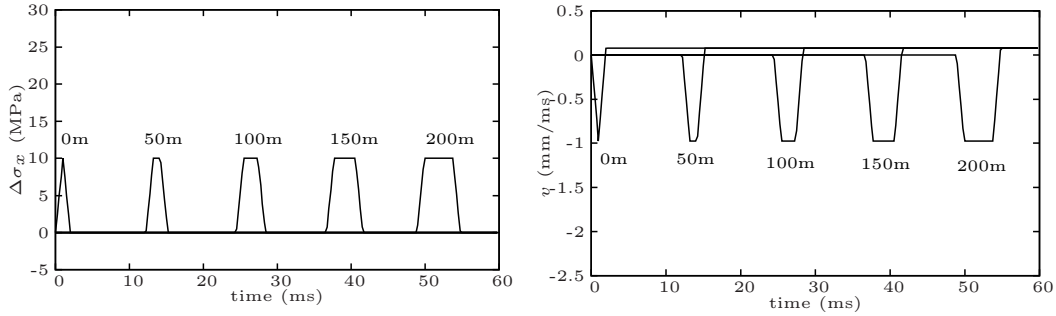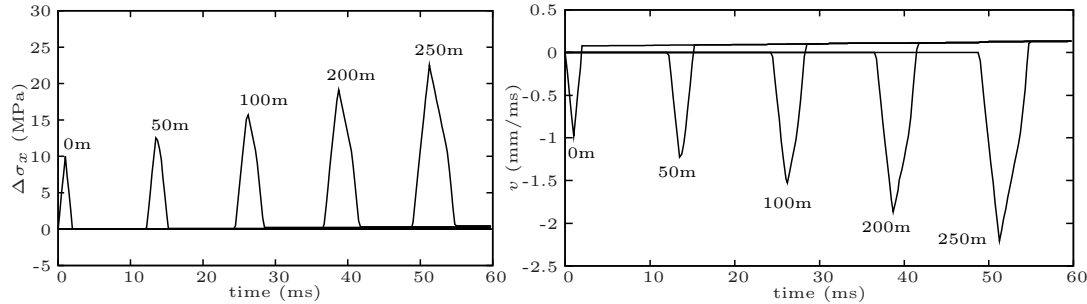
Figure 4. Time histories of axial stress and velocity with the free parameter $\dot\sigma_p = 0.0$ MPa/ms, with the free parameter v_p equal to 3.98 km/s. The width of the wave is increasing linearly in time.
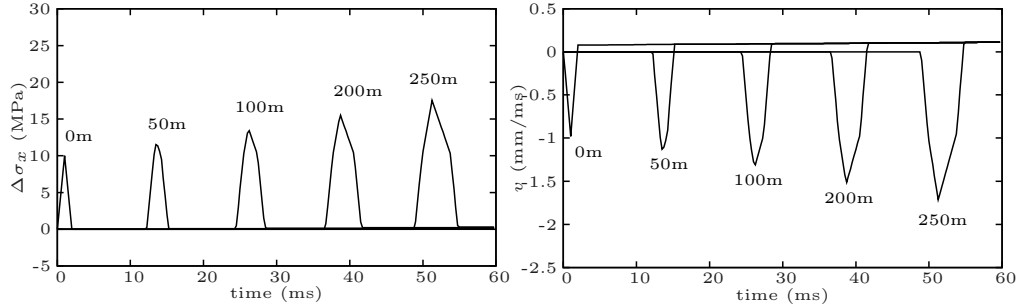
Figure 5. Time histories of axial stress and velocity with the free parameter $\dot\sigma_p = 0.15$ MPa/ms, with the free parameter v_p equal to 3.98 km/s. This solution exhibits an increase in both the width and amplitude of the wave.

figure shows time histories of axial stress and velocity at various axial locations. The unstable nature of these solutions is readily apparent in that both the widths and the amplitudes of the pulses increase linearly with time (except for the special case where $\dot\sigma_p = 0$, where the amplitude remains constant). Nonuniqueness is thus demonstrated by fact that these three different results each represent solutions to the original initial/boundary value problem. Later, numerical results will be shown to corroborate this purely analytical conclusion.

The case $\dot\sigma_p = 0$ can be viewed as a baseline solution in which the pulse widens with time but does not grow in amplitude. The widening results from the fact that the loading ramp is traveling faster than the unloading ramp. Since $\dot\sigma_p = 0$, the solution is constant in the separated region between the two ramps. Accordingly, the initially triangular pulse evolves into a trapezoidal pulse that grows wider with time, at a rate proportional to $c_L - c_U$. The other two cases illustrate the effect of progressively increasing the peak stress growth rate $\dot\sigma_p$. The linear growth in peak stress with time (and also with distance) is evident in the figure. The main effect of this growth is to superimpose a triangular pulse on top of the flat top of the baseline solution. The base of this triangle grows with time at a rate proportional to $c_L - c_U$, while the height grows at a rate proportional to $\dot\sigma_p$.

Figure 6. Time histories of axial stress and velocity with the free parameter $\dot{\sigma}_p = 0.250\,\mathrm{MPa/ms}$. This solution exhibits an increase in both the width and amplitude of the wave. The rate of increase of the magnitude of the wave may be specified to be arbitrarily large.

Since the rate at which the pulse widens is proportional to $c_L - c_U$, it follows that reducing the degree of achronicity (i.e., reducing the difference between c_L and c_U) would likewise reduce widening of the pulse. However, the growth in the *amplitudes* of the pulses would be unaffected, since they are proportional to the independent free parameter $\dot{\sigma}_p$. In fact, since $\dot{\sigma}_p$ may have an arbitrarily large value, it follows that any degree of achronicity, no matter how small, still admits an instability that is arbitrarily large in magnitude.

After the main pulse has passed over a given material particle, the particle is left with a residual velocity. This can be seen in the velocity plots in Figures 4, 5, and 6. This is a common occurrence in inelastic wave propagation problems, and may not seem surprising at first glance. However, upon closer inspection, it is found that this velocity is in the *opposite direction* from what would normally be expected (i.e., in the negative x-direction, whereas the particle velocity for the main wave is in the positive x-direction).

The unstable nature of these solutions is further illustrated in Figure 7, which shows the total kinetic energy (per unit cross-sectional area) vs. time for the three example solutions shown in Figure 4. The kinetic energy generated while the surface perturbation is being applied (from 0 to 2 ms) is roughly $3.4\,\mathrm{kJ/m^2}$, which is comparable to the energy that would be generated if the material response were purely elastic (about $3.5\,\mathrm{kJ/m^2}$). However, in the elastic case, the kinetic energy would remain constant after the perturbation is over. For the elastic-plastic solution shown here, kinetic energy continues to increase. In contrast, the kinetic energy for an associated flow rule would decrease in time. For the special case $\dot{\sigma}_p = 0$, the kinetic energy is linear with time, which is consistent with the fact that the pulse width grows at a constant rate, but the amplitude remains constant. For the other two solutions, the amplitude also increases at a constant rate, which introduces quadratic and cubic terms.

A simple way of understanding the growth in kinetic energy is to consider what happens to an individual particle (i.e., an infinitesimal element of material). As noted earlier, for a regular nonassociated flow rule, it is always possible to find closed strain cycles for which the work done on a material particle is negative, i.e., the particle does work on its surroundings. This occurs for any strain cycle that corresponds to a trial elastic stress increment lying in the wedge-shaped region shown in Figure 2. In these solutions, as the propagating pulse passes over each material particle, it puts the particle through a loading cycle that

is close to (although not precisely) a closed strain cycle, with a trial elastic stress increment that is in the wedge. As a result, the particle does work on its surroundings, thus liberating some stored elastic energy, much of which shows up in the form of kinetic energy. Kinetic energy in these solutions can increase without bound even if the boundary stimulus is infinitesimal. Even though this behavior technically corresponds to spontaneous motion from a quiescent state, it does *not* violate thermodynamics, since energy is not being created; prestored strain energy is merely being released in an unstable manner. As this process continues, the total kinetic energy continues to increase as long as there is material in an achronic state for the pulse to propagate into. Of course, for real specimens of finite dimension, an infinite kinetic energy would never be realized. As discussed later, observable characteristics of this instability (if real) in finite samples remains are unclear, but its potential existence merits much expanded laboratory investigation as well as first-principles theories to provide a microphysical basis for the behavior (if real). Novel experimental methods are needed to determine if the phenomenon of unstable liberation of elastic stored energy is physically possible, or merely an anomalous artifact of insufficient sophistication of classical nonassociated regular plastic flow rules.

Although most of the growth in kinetic energy comes from the release of prestored strain energy, there is a relatively small contribution from work done by traction acting on the surface of the half-space. From Figure 4, it can be seen that there is a small positive residual velocity at the surface after the perturbation has been completed. Since the ambient stresses from the prestress are compressive, this means that they continue to do positive work on the region. These instabilities are not somehow being fueled by this ever-increasing boundary work after the axial stress pulse has been applied. In fact, the continual rise in kinetic energy is entirely consistent with (a violation of) Drucker's stability postulates, which state that, for a stable plastic material, useful energy cannot be extracted from a material *and the system of forces acting on it* over a closed loading cycle [Drucker 1949; 1950]. Moreover, as mentioned earlier, analytical solutions can also be derived for problems in which the perturbation applied at the surface is a triangular velocity pulse rather than a triangular axial stress pulse, in which case the results are very similar to the results shown here even though *the post-pulse boundary loads do no work whatsoever*. The main difference is that the residual stress and velocity behind the main pulse are slightly different, and the kinetic energy vs. time curves are reduced by about 10 percent.[5]

5. Numerical solutions

An interesting question is whether the instabilities exhibited by these analytical solutions actually occur in numerical simulations. There are some legitimate reasons to think they might not. For example, since they emanate from a single point in space and time, they must always pass through a phase where they are too small to be resolved (spatially and/or temporally) in most numerical schemes. Also, most numerical simulations incorporate some form of viscosity (real and/or artificial), which introduces higher-order terms into the equations that Sandler and Rubin [1987] conjectured might cause the solutions to become unique. Of course, even if it turned out that instability and nonuniqueness *were* ruled out for these (or any

---

[5] Although the boundary tractions have little effect on the kinetic energy, the amount of work they do is nontrivial. For the three solutions shown in Figure 4, boundary work is of the order of $500 \, \text{kJ/m}^2$ at $t = 60 \, \text{ms}$. However, when compared to the corresponding solutions for velocity perturbations, it is found that almost all of this work ends up as residual strain energy rather than as kinetic energy. To put this in perspective, a change in the residual strain energy of this magnitude corresponds to a change in residual stress of less than 1 MPa.
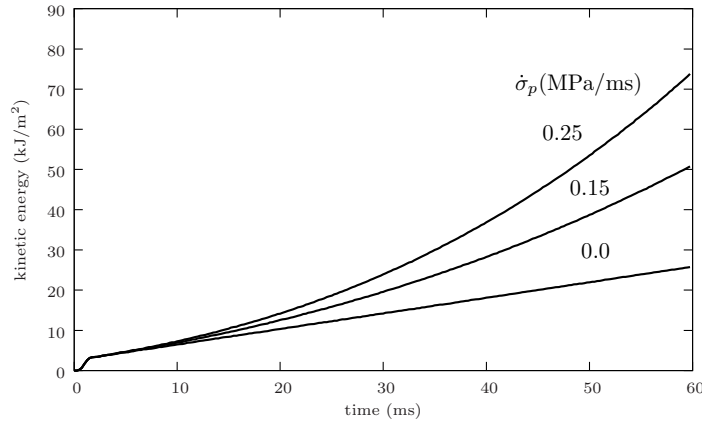
Figure 7. Total kinetic energy per unit cross-sectional area (i.e., $\int_0^\infty \frac{1}{2}\rho v \cdot v \, dx$) for the three analytical solutions shown in Figures 4, 5, and 6.

other) reasons, it would not justify the answers one gets using these simulations if the reasons were purely numerical, or lacked a physical basis. Nevertheless, it does raise some interesting numerical issues.

Even if instabilities do occur, it is not clear what form they might take. The family of solutions considered in the preceding section is only one of many possible families, and is itself doubly infinite (i.e., there are two free parameters, each of which may take on an infinite number of values). Yet, a digital computer will always give one and only one answer. Moreover, since the arithmetic operations it performs are completely deterministic, it will always give *exactly* the same answer no matter how many times you rerun the calculation, as long as the inputs (and computing hardware) are *exactly* the same. This raises some obvious questions: Which instability (if any) does the computer select? How does nonuniqueness manifest itself in numerical simulations?

To explore these questions, some numerical simulations were carried out using several finite-element codes (DYNA3D, ABAQUS, and a one-dimensional code of our own writing), as well as the explicit material point method (MPM) code Uintah. The results from the analysis using all of these codes were similar, but, as would be expected from the lack of unique solution to this problem, the numerical solutions differed slightly from code to code. The numerical solutions shown here are all those from the Uintah MPM code. For a comprehensive discussion of the MPM, and the similarities and differences between it and the finite-element method, the reader is referred to Sadeghirad et al. [2011]. A detailed description of how the problem was set up for the MPM will be given here, along with some comments on how the problem was solved with the various finite-element codes.

For the Uintah simulations the problem domain was discretized into a 700 meter long line of 3D rectangular cells with two MPM particles per cell. For the two commercial codes a single line of hexahedral elements was used. Although the strain increments associated with the perturbation involve pure uniaxial strain, the initial state σ^* is not a uniaxial strain state. Two approaches have been used to attain the initial conditions for this problem. The ABAQUS simulations began at a unstressed state with the loads gradually being increased to the desired stress state. After the desired conditions were reached, further lateral displacement was constrained and the axial stress perturbation was applied. In the DYNA3D and Uintah simulations, the constitutive model was modified so that stresses and strains
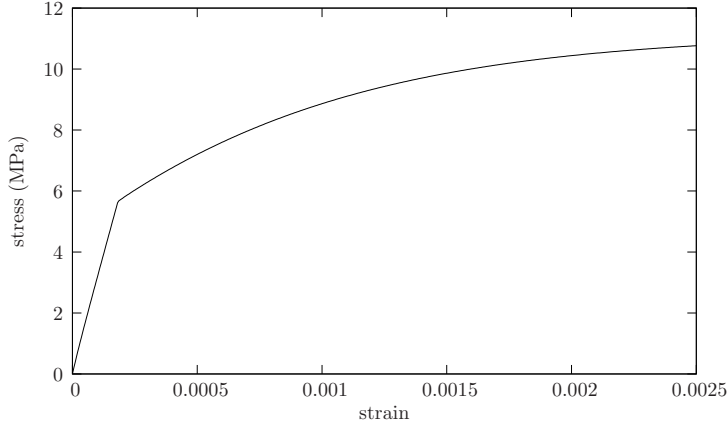
Figure 8. Uniaxial stress versus strain plot for the nonlinear hardening model used for numerical solutions.

would be measured relative to the prestressed state, rather than the unstressed state. This eliminated the need for the initialization phase, and the lateral (y- and z-faces) boundaries are constrained to have zero lateral displacement throughout the simulation. In accordance with the problem description given in Section 2, one x-face of the domain had an applied traction boundary condition given by (4)–(7), and the opposite x-face of the domain is specified to have zero displacement in the x-direction.

The case-study problem was solved using both the perfect-plasticity constitutive model used for the analytical solutions derived in Section 4 as well as a similar linear Drucker–Prager model with the nonlinear hardening yield function

$$f = \sqrt{J_2} + \alpha I_1 - k_{\text{limit}} - (k_o - k_{\text{limit}})e^{-z/z_{\text{ref}}}, \tag{34}$$

where k_{limit} is the maximum value of the yield strength, z is the cumulative equivalent plastic strain, and z_{ref} is a parameter that controls the rate at which the maximum yield strength is approached.

The nonlinear hardening parameters were chosen to be $k_{\text{limit}} = 10$ MPa and $z_{\text{ref}} = 0.001$. Figure 8 shows axial stress versus axial strain for a uniaxial stress loading path with the nonlinear hardening model with the chosen parameter values. As the plot clearly indicates, the plastic tangent modulus (and thus the plastic wave speed) is continually changing with plastic loading.

5.1. *Temporal and spatial convergence.* An initial element length of 0.5 m was chosen for use in a temporal convergence study. The Courant–Friedrichs–Lewy (CFL) time step was calculated from the elastic properties as is commonly done in explicit finite-element codes. It was discovered that the solution became unstable for time steps greater than 0.8 times the CFL time step calculated from the elastic properties. This was to be expected since the plastic wave speed is greater than the elastic wave speed for this problem. Figure 9 is a plot of the peak change in axial stress caused by the propagating wave at a point 600 meters into the problem domain for various time step factors. The time step factor is defined as the ratio of the actual time step used in a simulation to the CFL time step calculated from the elastic wave speed. As the figure shows, the numerical simulation converged with respect to the time step size with a time step of approximately 10% of the CFL time step.
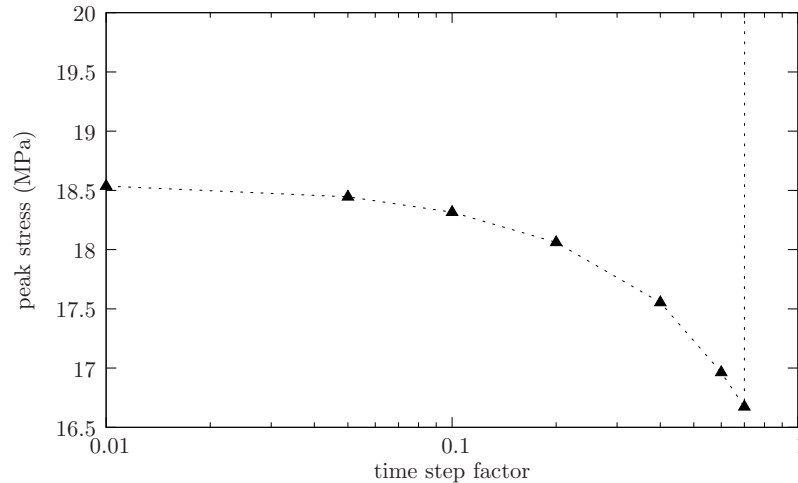
Figure 9. Plot of the change in axial stress caused by the stress wave at a location 600 meters into the problem domain for various time step factors. The time step factor is the ratio of the actual time step used int he simulation to the CFL time step calculated from the elastic properties of the material. The peak axial stress appears to have converged at approximately 10% of the elastic CFL time step.

In accordance with the temporal convergence study, several simulations were performed with the time step set to 10% of the CFL time step and a progressively smaller element length. Figure 10 shows some numerical solutions of the example problem. As the plots show, the solutions with a mesh resolution of 0.5 m and 0.25 m appear very similar, giving the impression that the solution has converged. However, if the mesh spacing is reduced again, the solution changes considerably, with secondary peaks forming approximately 500 meters into the domain. These secondary peaks grow at a more rapid rate than the primary peak. If the mesh is refined further these secondary peaks form earlier and earlier, and grow at an increased rate without bound. While we have only shown solutions from the Uintah MPM code, the results from the ABAQUS and DYNA3D exhibited the same trends with mesh refinement.

For the simulations performed in DYNA3D, it was found that two simulations with identical input parameters but with a different number of time history output blocks produced dramatically different solutions. It was found that the preprocessor had altered the seventh or eighth digit of the initial locations of approximately 10% of the nodes. It appears that the numerical solution is very sensitive to small changes in the initial conditions of the simulation. This chaos appears to be a manifestation of the nonuniqueness discussed in Section 4.

Stoughton and Yoon [2008] have asserted that the Sandler–Rubin instability cannot exist if the plastic tangent modulus is not constant to first order. The basis for this assertion is that, if nonconstant wave speeds are substituted into the Sandler–Rubin solution, the resulting expressions fail to satisfy the governing equations. However, as discussed above, this does not mean that the Sandler–Rubin instability cannot exist if the wave speed is not constant — it simply means that the Sandler–Rubin analytical solution was limited to the special case of a constant wave speed. Accordingly, there is no reason to expect that such a solution should apply to a nonconstant wave speed.
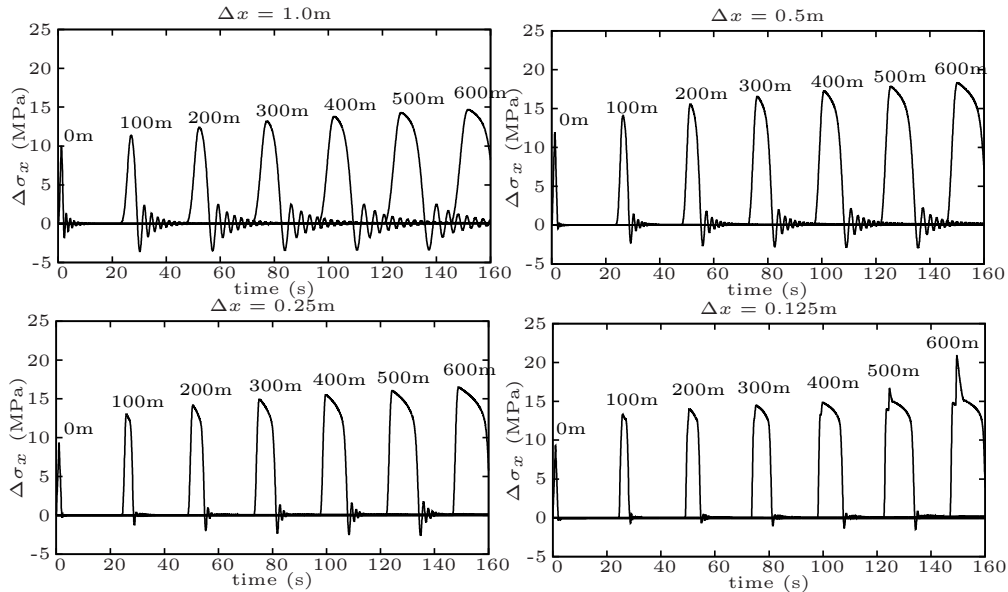
Figure 10. Numerical solutions to the case study problem with perfect plasticity and 1 m, 0.5 m, 0.25 m, and 0.125 m cell widths, illustrating the lack of convergence with mesh refinement. As the axial stress histories with $\Delta x = 0.125$ m indicate, as the mesh is refined additional peaks in the waveform appear that grow rapidly in time. These additional peaks form at earlier and earlier times as the mesh is refined further.

Stoughton defines several classes of plasticity models that do not result in a constant plastic tangent modulus, and therefore were claimed not to admit the Sandler–Rubin instability. One class of models that has this attribute is any model with nonlinear hardening. Although somewhat counterintuitive, it is shown in the companion paper that, for achronic loading conditions, hardening actually reduces the wave speed, and softening increases the wave speed, as compared to a perfectly plastic response. Therefore, hardening would be expected to reduce the degree of achronicity (i.e., the degree to which the plastic wave speed is faster than the elastic wave speed) when the material initially yields. However, with most nonlinear hardening functions, including the one chosen for this example, the tangent hardening modulus decreases as the material undergoes plastic deformation, which will cause the plastic wave speed to approach the perfect plasticity wave speed as plastic flow continues. For the purpose of the example problem considered here, in the x-t diagram for the nonlinear hardening case the characteristics for the head of the wave, which are undergoing plastic deformation, will still diverge from the characteristics for the tail of the wave, which is undergoing elastic deformation. The primary difference is that characteristics on the head of the wave will not be parallel, since at each point of the wave the material will have undergone a different amount of plastic deformation and will therefore have a different plastic tangent modulus and hence a different wave speed. However, for all points on the head of the wave, the wave speed will exceed the elastic wave speed, which will cause the development of the region between the head and tail of the wave to form, which has no uniquely defined characteristics and hence no unique solution.
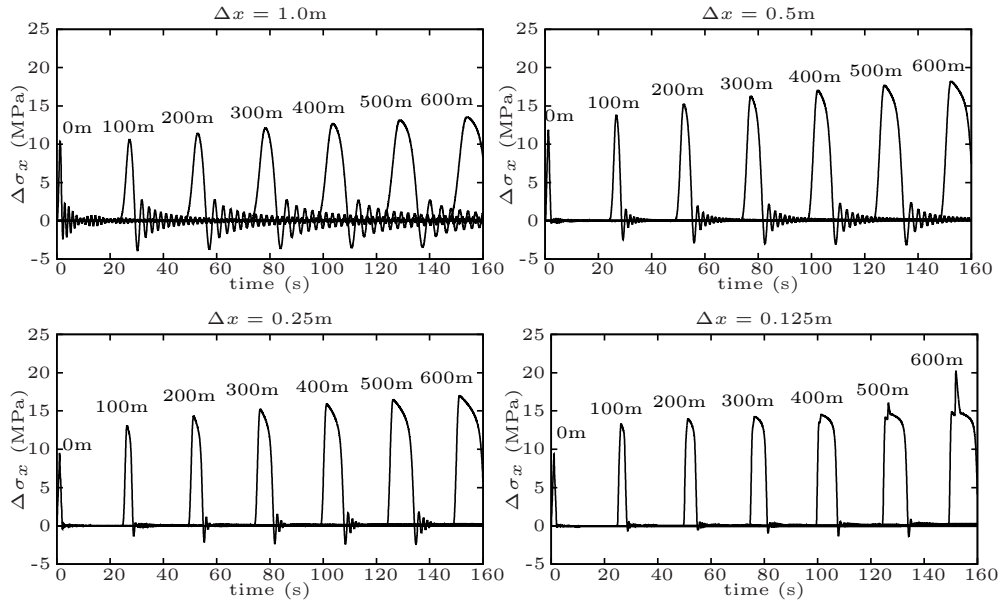
Figure 11. Numerical solutions to the case study problem with the nonlinear hardening model given in (34) and 1 m, 0.5 m, 0.25 m, and 0.125 m element lengths, illustrating the lack of convergence with mesh refinement even with the nonlinear hardening model for which the plastic wave speed is not constant. As with the nonhardening case, additional peaks in the waveform and an increase in instability develop with a mesh spacing of 0.125 m. Further mesh refinement results in these additional peaks occurring even earlier and growing more rapidly.

To illustrate that a nonlinear hardening model does admit the Sandler–Rubin instability, the same case study problem was solved with the nonlinear hardening Drucker–Prager model given in (34). The axial stress histories found using this model and mesh spacings of 1 m, 0.5 m, 0.25 m, and 0.125 m are shown in Figure 11. To assuage any lingering concerns that this instability is the result of time-integration instability, for these results we used a time step of one one-hundredth of the CFL time step calculated using the elastic stiffness, which is an order of magnitude smaller than the time step used to generate the plots in Figure 10. As the axial stress histories indicate, just as with the nonhardening case, the instability remains and the solution does not converge with mesh refinement, suggesting that the governing equations remain ill-posed for this case.

6. Conclusion

In this paper we have introduced a simple case study that illustrates an instability that has long been known to be caused by nonassociated plastic flow, but which has been largely overlooked in the literature in comparison to better-known instabilities such as localization or flutter. The mathematical origin of this instability is referred to as achronicity, in which the wave speed in plastic loading exceeds that in elastic unloading. A key goal of this work is to call attention to the lack of experimental evidence

validating or invalidating existence of achronicity, which is predicted for *any* nonassociated regular flow rule. It was shown that this condition can lead to both instability and nonuniqueness of solutions to the equations of motion. This assertion was demonstrated analytically by showing that the problem has a two-parameter family of nonunique solutions, which are unstable in that both the width, amplitude, and kinetic energy of the pulse all increase with time. It was then demonstrated that similar instabilities also occur in numerical calculations, where thorough attention was paid to ensuring that the instability was *not* caused by an insufficiently small time step. The nonuniqueness of nonassociative plasticity causes the numerical solutions to fail to converge with mesh refinement. The solutions are, in some cases, chaotically sensitive to small changes in the inputs. The mechanism that drives these instabilities is an unstable conversion of prestored strain energy into kinetic energy. The loading paths in this problem are similar in character to those discussed by Drucker [1949; 1950] and Il'Yushin [1961] in their discussions of stability of plasticity models more than fifty years ago, so the novel and worthwhile aspect of this work lies in the formulation of the illustrative case study itself. The case study demonstrates that this anomaly (which is not known to be real or merely a symptom of an insufficiently sophisticated model) still exists today in simple constitutive models commonly available in production finite-element codes, thus calling into question the mathematical well-posedness of any engineering application of such models.

The instabilities are very mild. Their growth rate is only linear with time, and only a small fraction of the prestored strain energy is actually converted into energy of motion. However, it is *precisely* these characteristics that cause them to be among the most insidious forms of instability. They can grow large enough to affect the answer, while staying small enough to not cause obvious problems such as code crashes from excessive deformation.

This achronic instability can be contrasted with other well-known forms of instability, such as time-stepping instabilities in explicit numerical calculations, which grow exponentially with time. Although time step instabilities are more serious in principle, they could be viewed as less serious in practice, precisely because they grow rapidly enough to quickly call attention to themselves. Achronic instabilities, on the other hand, are much less catastrophically disruptive, and much more difficult to detect in complex calculations. However, it is possible to detect achronicity by monitoring certain easily evaluated directional invariants of the elastic-plastic tangent stiffness tensor [Brannon and Drugan 1993].

A key purpose of this paper has been to reveal gaps in experimental data that prevent ascertaining if the Sandler–Rubin instability is real, or just a numerical and theoretical artifact of an ill-posed constitutive model. Part II of this paper explores the influence of various nonclassical constitutive model features on the instability, but the question of whether or not the instability is realistic remains open, pending careful experimental investigations of loading into the Sandler–Rubin wedge. Stoughton and Yoon [2008; 2012] conjectured what might serve as possible physical mechanisms and symptoms of the instability if it is indeed real (e.g., Lüders bands or serrated flow observed in some aluminum alloys at room temperature range). Again, these are conjectures for which systematic laboratory investigations of material response in the Sandler–Rubin wedge are warranted, but not yet achieved. Direct observations of material response (especially detection of negative net work in closed strain cycles) for loading into the Sandler–Rubin wedge would be a natural first focus area for laboratory testing. As discussed by Brannon et al. [2009], such experimental efforts are highly nontrivial because a statistically significant number of experiments must be conducted to identify the yield surface and apparent flow direction at a given stress state so that the location of the Sandler–Rubin wedge can be determined. For this reason,

exploratory *numerical* modeling of realistic microstructures (such as computed-tomography images of rock) might be appropriate because, unlike real laboratory testing, the material state can be *exactly* reset to probe path-dependent responses to various loading directions.

Acknowledgments

References

[Besse and Mohr 2012] C. C. Besse and D. Mohr, "Plasticity of formable all-metal sandwich sheets: Virtual experiments and constitutive modeling", *Int. J. Solids Struct.* **49**:19–20 (2012), 2863–2880.

[Bigoni 1995] D. Bigoni, "On flutter instability in elastoplastic constitutive models", *Int. J. Solids Struct.* **32**:21 (1995), 3167–3189.

[de Borst et al. 1993] R. de Borst, L. Sluys, H. Muhlhaus, and J. Pamin, "Fundamental issues in finite element analyses of localization of deformation", *Eng. Computation.* **10**:2 (1993), 99–121.

[Brannon 2007] R. M. Brannon, "Elements of phenomenological plasticity: Geometrical insight, computational algorithms, and topics in shock physics", pp. 225–274 in *ShockWave science and technology reference library*, edited by Y. Horie, Springer, Berlin, 2007.

[Brannon and Drugan 1993] R. M. Brannon and W. J. Drugan, "Influence of nonclassical elastic-plastic constitutive features on shock wave existence and spectral solutions", *J. Mech. Phys. Solids* **41**:2 (1993), 297–330.

[Brannon et al. 2009] R. Brannon, J. Burghardt, D. Bronowski, and S. Bauer, "Experimental assessment of unvalidated assumptions in classical plasticity theory", Report SAND2009-0351, Sandia National Laboratory, 2009, Available at http://www.mech.utah.edu/~brannon/pubs/7-BrannonBurghardtSAND-Report2009-0351.pdf.

[Cvitanic et al. 2008] V. Cvitanic, F. Vlak, and Z. Lozina, "A finite element formulation based on non-associated plasticity for sheet metal forming", *Int. J. Plast.* **24**:4 (2008), 646–687.

[Desmorat and Marull 2011] R. Desmorat and R. Marull, "Non-quadratic Kelvin modes based plasticity criteria for anisotropic materials", *Int. J. Plast.* **27**:3 (2011), 328–351.

[Drucker 1949] D. C. Drucker, "Relation of experiments to mathematical theories of plasticity", *J. Appl. Mech.* (*ASME*) **16** (1949), 349–357.

[Drucker 1950] D. C. Drucker, "Some implications of work hardening and ideal plasticity", *Quart. Appl. Math.* **7** (1950), 411–418.

[Drumheller 1998] D. S. Drumheller, *Introduction to wave propagation in nonlinear fluids and solids*, Cambridge Univ. Press, 1998.

[Dunand et al. 2012] M. Dunand, A. P. Maertens, M. Luo, and D. Mohr, "Experiments and modeling of anisotropic aluminum extrusions under multiaxial loading, I: Plasticity", *Int. J. Plast.* **36** (2012), 34–49.

[Gao et al. 2011] X. Gao, T. Zhang, J. Zhou, S. M. Graham, M. Hayden, and C. Roe, "On stress-state dependent plasticity modeling: Significance of the hydrostatic stress, the third invariant of stress deviator and the non-associated flow rule", *Int. J. Plast.* **27**:2 (2011), 217–231.

[Il'Yushin 1961] A. Il'Yushin, "On postulate of plasticity", *J. Appl. Math. Mech.* **25**:3 (1961), 746–752.

[Kamojjala et al. 2015] K. Kamojjala, R. Brannon, A. Sadeghirad, and J. Guilkey, "Verification tests in solid mechanics", *Eng. Comput.* **31**:2 (2015), 193–213.

[Lade et al. 1987] P. V. Lade, R. B. Nelson, and Y. M. Ito, "Nonassociated flow and stability of granular materials", *J. Eng. Mech. (ASCE)* **113**:9 (1987), 1302–1318.

[LeVeque 1992] R. J. LeVeque, *Numerical methods for conservation laws*, 2nd ed., Birkhäuser, Basel, 1992.

[Mohr et al. 2010] D. Mohr, M. Dunand, and K.-H. Kim, "Evaluation of associated and non-associated quadratic plasticity models for advanced high strength steel sheets under multi-axial loading", *Int. J. Plast.* **26**:7 (2010), 939–956.

[Rousselier et al. 2012] G. Rousselier, M. Luo, and D. Mohr, "Macroscopic plasticity modeling of anisotropic aluminum extrusions using a Reduced Texture Methodology", *Int. J. Plast.* **30–31** (2012), 144–165.

[Rudnicki and Rice 1975] J. Rudnicki and J. R. Rice, "Conditions for the localization of deformation in pressure-sensitive dilatant materials", *J. Mech. Phys. Solids* **23**:6 (1975), 371–394.

[Sadeghirad et al. 2011] A. Sadeghirad, R. M. Brannon, and J. Burghardt, "A convected particle domain interpolation technique to extend applicability of the material point method for problems involving massive deformations", *Int. J. Numer. Methods Eng.* **86**:12 (2011), 1435–1456.

[Sandler and Pučik 1993] I. S. Sandler and T. A. Pučik, "Non-uniqueness in dynamic rate-independent non-associated plasticity", Technical Report DNA-TR-92-108, Defense Nuclear Agency, 1993, Available at http://tinyurl.com/qg92z3k.

[Sandler and Rubin 1987] I. S. Sandler and D. Rubin, "The consequences of non-associated plasticity in dynamic problems", pp. 345–353 in *Constitutive laws for engineering materials* (Tucson, AZ), edited by C. Desai, Elsevier, Amsterdam, 1987.

[Shen et al. 2012] W. Shen, J. Shao, D. Kondo, and B. Gatmiri, "A micro-macro model for clayey rocks with a plastic compressible porous matrix", *Int. J. Plast.* **36** (2012), 64–85.

[Spitzig et al. 1975] W. A. Spitzig, R. J. Sober, and O. Richmond, "Pressure dependence of yielding and associated volume expansion in tempered martensite", *Acta Metall.* **23**:7 (1975), 885–893.

[Spitzig et al. 1976] W. A. Spitzig, R. J. Sober, and O. Richmond, "The effect of hydrostatic pressure on the deformation behavior of maraging and HY-80 steels and its implications for plasticity theory", *Metall. Trans. A* **7**:11 (1976), 1703–1710.

[Stoughton 2002] T. B. Stoughton, "A non-associated flow rule for sheet metal forming", *Int. J. Plast.* **18**:5–6 (2002), 687–714.

[Stoughton 2012] T. Stoughton, Informal communication, 2012. Email dated Jan. 13, 2012.

[Stoughton and Yoon 2008] T. Stoughton and J. W. Yoon, "On the existence of indeterminate solutions to the equations of motion under non-associated flow", *Int. J. Plast.* **24**:4 (2008), 583–613.

[Taherizadeh et al. 2010] A. Taherizadeh, D. E. Green, A. Ghaei, and J.-W. Yoon, "A non-associated constitutive model with mixed iso-kinematic hardening for finite element simulation of sheet metal forming", *Int. J. Plast.* **26**:2 (2010), 288–309.

[Thomas 1999] J. W. Thomas, *Numerical partial differential equations: Conservation laws and elliptic equations*, Texts in Applied Mathematics **33**, Springer, New York, 1999.

THOMAS PUČIK: *(Deceased) Pučik Consulting, 2057 Brixham Dr., Roseville, CA 95747, United States*

REBECCA M. BRANNON: rebecca.brannon@utah.edu
University of Utah, 50 S. Campus Dr., Salt Lake City, UT 84108, United States

JEFFREY BURGHARDT: jburghardt@slb.com
Schlumberger, 1935 S. Fremont Dr., Salt Lake City, UT 84104, United States

msp

NONUNIQUENESS AND INSTABILITY OF CLASSICAL FORMULATIONS OF NONASSOCIATED PLASTICITY, II: EFFECT OF NONTRADITIONAL PLASTICITY FEATURES ON THE SANDLER–RUBIN INSTABILITY

JEFFREY BURGHARDT AND REBECCA M. BRANNON

In the companion article a case study problem was presented that illustrated a dynamic instability related to nonassociated plastic flow. This instability allows stress waves to grow in both amplitude and width as they propagate. In addition to this physically implausible behavior, multiple solutions to the equations of motion were shown to exist, which causes numerical solutions not to converge with mesh refinement. Reformulation of some aspects of traditional plasticity theory is necessary since associated models over-predict the amount of plastic dilatation, and nonassociated models may result in this physically unrealistic behavior. The case study solutions in the companion paper were limited to a few relatively simple plastic models. The purpose of this paper is to investigate the effects of various traditional and nontraditional plasticity features on the existence of the instability and resulting nonuniqueness. The instability and nonuniqueness are shown to persist with both hardening and softening. An incrementally nonlinear model is shown to eliminate the instability and result in mesh-independent solutions. A viscoplastic model is shown to lead to unstable solutions for all loading rates. However, mesh-independent numerical solutions are found when the loading timescale is much less than the plastic relaxation time. A nonlocal plasticity model is shown to produce solutions that are both unstable and mesh-dependent. Therefore, of the models considered, only the incrementally nonlinear model was capable of eliminating this nonphysical instability. This work provides much needed direction for laboratory investigations of the validity of incrementally nonlinear flow rules.

1. Introduction

An associated plasticity model is one for which the plastic strain rate tensor is proportional to the normal to the yield surface. While associated models have been shown to lead to unique solutions to boundary value problems [Hill 1958], several studies have demonstrated that associated flow rules are incompatible with experimental data.

Specifically, Spitzig et al. [1976] showed that associated models over-predict the amount of plastic dilatation in triaxial compression tests of metals. Lade et al. [1987] and Shen et al. [2012] found a similar problem with associated flow rules for geologic materials. More recently, it has been shown that nonassociated flow rules describe the anisotropic plastic flow of sheet metals better than associated flow rules [Stoughton 2002; Cvitanic et al. 2008; Mohr et al. 2010; Taherizadeh et al. 2010]. Additionally, Gao et al. [2011] have developed a plasticity model for aluminum 5083 and shown that, under a variety of loading conditions, a nonassociated model is in closer agreement with experimental data than is an associated model. However, several recent papers [Desmorat and Marull 2011; Dunand et al. 2012; Besse

and Mohr 2012] have shown that a nonassociated flow rule is not necessary to describe the anisotropic plasticity of rolled sheet metal if other plasticity features are included. Popov and Lagoudas [2007] and Saint-Sulpice et al. [2009] found it necessary to use a nonassociated flow rule to describe the inelastic behavior of shape memory alloys, but more recently Saleeb et al. [2011] have developed and validated a shape memory alloy model utilizing an associated flow rule.

While these studies clearly represent a significant improvement upon more traditional metal plasticity models, Paquet et al. [2011] and Rousselier et al. [2012] describe several phenomena relating to the evolution of plastic anisotropy that are not well-described by even advanced macroscopic phenomenological plasticity models. Rousselier demonstrated that a model based on polycrystalline metal plasticity is capable of describing these complex behaviors. As noted in this recent work, when the material microstructure is accounted for, the yield surface can take on complex shapes, including the formation of vertices. At a vertex in the yield surface, the plastic flow direction depends upon the direction of loading and is therefore an irregular flow rule.

Many of these studies have demonstrated that certain nonassociated models are more compatible with experimental data than are similar associated models. This may be attributed to the additional mathematical flexibility of nonassociated models rather than to any physical arguments. This is well illustrated by the recent microscopically-based models discussed above.

Despite the fact that nonassociated models often fit experimental data better, the adoption of a nonassociated model brings with it a host of possible problems. For example, nonassociated models do not satisfy Drucker's stability postulate [1950] for all loading directions. Of course, Drucker's stability postulate is merely a sufficient, but not necessary, condition for stability and uniqueness. As discussed in detail below, nonassociated models have been shown to result in instability and a loss of uniqueness for certain loading conditions.

A well-known loading condition that results in both the loss of uniqueness of solution and instability with a nonassociated flow rule was discovered by Rudnicki and Rice [1975]. They showed that, under certain loading directions, a nonassociated model could result in a localization instability even while the material remained in the hardening regime. This localization instability has been shown to result in a loss of uniqueness of solution for local rate-independent plasticity models. This instability and nonuniqueness have been extensively studied over the years [Bažant 1976; de Borst et al. 1993; Dorgan 2006; Valanis 1998]. While the softening-like behavior of nonassociated models is consistent with experimental data, the governing equations are nevertheless ill-posed with the occurrence of this behavior and must be regularized in some way. The current leading regularization approaches appear to be nonlocal plasticity and gradient plasticity.

A related form of instability and loss of uniqueness of solution related to nonassociated plastic flow is the flutter instability [Bigoni 1995]. Whereas the localization instability occurs when a negative eigenvalue of the constitutive operator arises, the flutter instability occurs when a complex eigenvalue arises. For a more detailed discussion of the effect of nonassociated flow rules on the eigenvalues of the constitutive operator, see [Brannon and Drugan 1993]

Another, and fundamentally different, source of instability and nonuniqueness caused by nonassociated plastic flow was first observed by Sandler and Rubin [1987]. They showed that with any degree of nonassociativity there exist loading directions for which the wave speed in plastic loading exceeds the wave speed in elastic unloading. This over-stiffening occurs any time the trial stress rate tensor

has a positive inner product with the normal to the yield surface, but a negative inner product with the plastic strain rate tensor. This region of stress space, which lies above the yield surface, but below the plastic flow potential surface, will be herein referred to as the Sandler–Rubin wedge. Sandler and Rubin showed that the existence of these so-called "fast plastic" waves causes a loss of uniqueness of solutions and that solutions are admitted for which an infinitesimal stress perturbation can nonphysically grow in amplitude and width as it propagates. This phenomenon is essentially equivalent to spontaneous motion from a quiescent state, which can be construed as an implausible behavior for a passive material. Under these conditions all of the eigenvalues of the plastic tangent stiffness tensor are real and positive, so this phenomenon is not related to the localization or flutter instability previously discussed.

Nonetheless, the numerical manifestation of the ill-posedness caused by the Sandler–Rubin instability is remarkably similar to that caused by localization. Specifically, when a local model is used to solve a localization problem, the strain in the localization region becomes unbounded with mesh refinement. For localization problems, the region of unbounded strain is stationary in a Lagrangian sense. For the Sandler–Rubin instability, the region of unbounded strain lies at the peak of a propagating stress wave. As the head and tail of the wave diverge because of the inversion in plastic wave speeds, the region of unbounded strain expands linearly in time. In the one-dimensional problem considered in the companion paper, the solution in this region of space was shown to be subject to only two constraints:

$$0 \leq \dot{\sigma} \tag{1}$$

and

$$C_E < v < C_P, \tag{2}$$

where $\dot{\sigma}$ is the axial component of the stress rate, C_E is the elastic wave speed, v is the wave speed in the region of nonuniqueness, and C_P is the plastic wave speed.

In a pair of relatively recent articles on plastic stability, Stoughton and Yoon [2006; 2008] have expressed some concerns about the range of validity of the Sandler–Rubin instability. In the second of these articles they suggest that the Sandler–Rubin instability is permitted by only a very small and simple subset of nonassociated plasticity models, and that any model with a nonconstant plastic wave speed will not be subject to the problems identified by Sandler and Rubin. In the companion paper it was shown via a numerical example that a model with nonlinear hardening, which produces a nonconstant plastic wave speed, results in the same problems that result with linear hardening.

In light of both the loss of uniqueness of solution and the physically implausible behavior permitted under the Sandler–Rubin instability, it seems that traditional nonassociated models must be rejected. However, as discussed previously, associated models also must be rejected since they are incompatible with experimental data. Clearly a resolution to this problem lies outside of traditional plasticity theories. The purpose of this paper is to investigate several nontraditional theories to determine which, if any, of these theories are capable of matching experimental data while at the same time eliminating the physically implausible Sandler–Rubin instability and resulting in unique solutions.

In part I of our paper, the existence and characteristics of the Sandler–Rubin instability were illustrated using both analytical and numerical solutions to a simple one-dimensional wave-propagation problem. To illustrate the instability in the simplest possible context, the companion paper employed a rate-independent, perfectly plastic, and nonlinear hardening model. In this paper we solve this same case study problem with a variety of generalizations of this simple model.

The case study problem of the companion paper is briefly described in Section 2. In Section 4, we examine various generalizations of the simple plasticity model considered in the companion article. The first of these generalizations discussed is a more detailed examination of hardening and softening than was presented in the companion paper. The second reformulation considered is the adoption of an incrementally nonlinear flow rule, which allows the plastic flow direction to change based on the incremental loading direction. The third alternative theory considered is the adoption of rate-dependence. The final reformulation of traditional plasticity theory considered here is an integral-type nonlocal plasticity theory.

2. Description of the case study problem from part I

In this section, a simple numerical case study problem is described that elicits the Sandler–Rubin instability. This case study problem, originally developed by Thomas Pučik, is described in greater detail in the companion article. The case study problem consists of a semi-infinite elastic/plastic half-space as shown in Figure 1. The axial component of the initial stress state σ_X^* is chosen to be -100 MPa, while the lateral component, $\sigma_Y^* = \sigma_Z^*$, is chosen to be -17.55 MPa, where stresses are taken to be positive in tension. The material is also assumed to be in a quiescent initial state. The linear Drucker–Prager yield function used in this case study is

$$f = \sqrt{J_2} + \alpha I_1 - k_o, \tag{3}$$

where $J_2 = \frac{1}{2} S : S$, S is the deviatoric stress tensor, $I_1 = \mathrm{Tr}(\sigma)$, and α and k_o are material parameters whose values are chosen to be 0.315 and 5.066 MPa respectively. With these parameters, and the chosen initial stress state, the material is at incipient yield in its initial condition. The dilatation angle is chosen to be zero, meaning that the plastic strain rate tensor is proportional to the deviatoric part of the stress tensor and therefore has no volumetric part. Various generalizations of this simple model will be considered and are discussed in detail below. This model was contrived to simplistically demonstrate the existence and character of the instability. In what follows, various enhancements to this model are systematically explored for the effect on the instability in this case study.

The surface traction at the free surface is initially -100 MPa, which places the material in equilibrium in the initial state. A small perturbation is applied to the surface traction as shown in Figure 1. The perturbation is characterized by the peak change in stress $\sigma_o = 10$ MPa, and the duration of the pulse $\tau = 2$ ms. Since the axial component of stress changes from -100 MPa to -90 MPa, this is a tensile stress increment that reduces both the confining pressure and the magnitude of the stress deviator and induces plastic flow. This loading increment is reversed by returning the axial component of the stress tensor to its initial value in what can be shown to be an elastic recompression increment. This loading sequence results in the triangular-shaped time-history of the perturbation shown in Figure 1, with the front of the triangular pulse placing the material in a plastic loading state and the tail of the pulse placing the material in an elastic unloading state. Here loading refers to an increment that induces plastic flow and unloading refers to an increment that is purely elastic, even though the plastic loading increment represents a decrease in the applied load.

This perturbation causes a longitudinal wave to propagate through the half-space. As shown in the companion article, this loading condition places the trial stress rate in the Sandler–Rubin wedge and results in a plastic wave speed that exceeds the elastic wave speed. In the companion article this case study problem was shown to possess a two-parameter family of nonunique analytical solutions. The
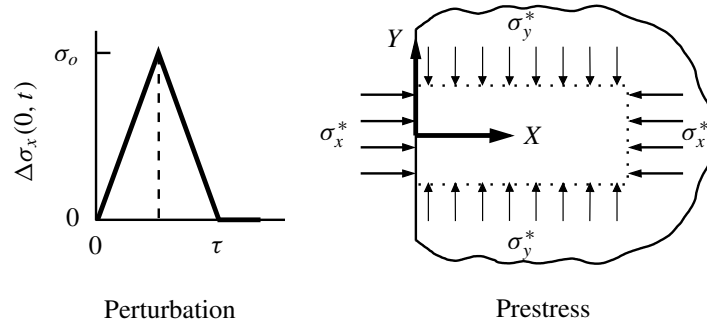
Figure 1. Geometry and loading for the case study problem.

problem was also solved numerically using the finite-element and material point methods. Figure 2 shows an example of the numerical solutions presented in the companion paper, which were found using the Uintah material point method (MPM) code [de St. Germain et al. 2000; Sulsky et al. 1994; Bardenhagen and Kober 2004], which is also used in the simulations presented in this paper.

As these solutions illustrate, the head of the wave (left-hand portion of the stress wave history) and the tail of the wave (right-hand portion of the stress wave history) are diverging from each other due to the plastic wave speed exceeding the elastic wave speed. This causes what is initially a single point at the top of the triangular stress pulse to open up into a finite region. It is in this region that the solution is nonunique. This nonuniqueness becomes apparent in analytical solutions by the presence of free parameters in the solution. In contrast, nonuniqueness can be much more subtle in numerical solutions. As with the nonuniqueness that occurs in localization problems, the numerical manifestation of the Sandler–Rubin instability occurs primarily though a mesh-dependency of the solution. This can be observed by comparing the coarse resolution plot on the left-hand side of Figure 2 with the finer resolution on the right-hand side of the same figure. At late times in the more resolved solution, secondary peaks in the stress wave begin to form, which grow much more rapidly than the primary peak. As the mesh is further
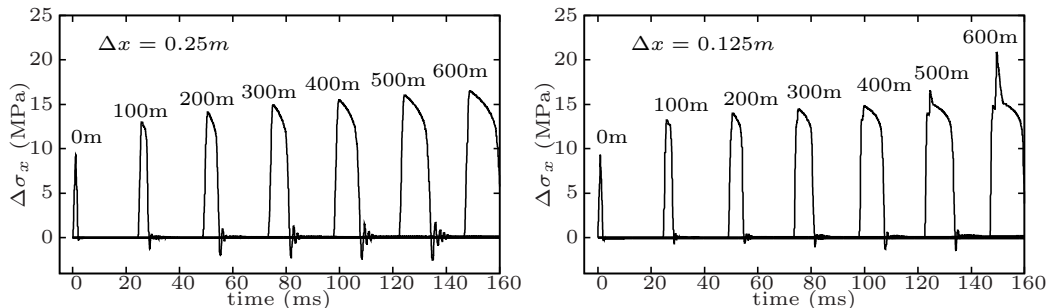
Figure 2. Stress histories at various locations throughout the problem domain using a local plasticity model, no hardening, and a mesh resolution of $\Delta x = 0.25$ m (left) and $\Delta x = 0.125$ m (right). This result was found using the Uintah MPM code and has been independently confirmed via analytical solutions and numerical solutions using a variety of FEM codes, as described in the companion paper.
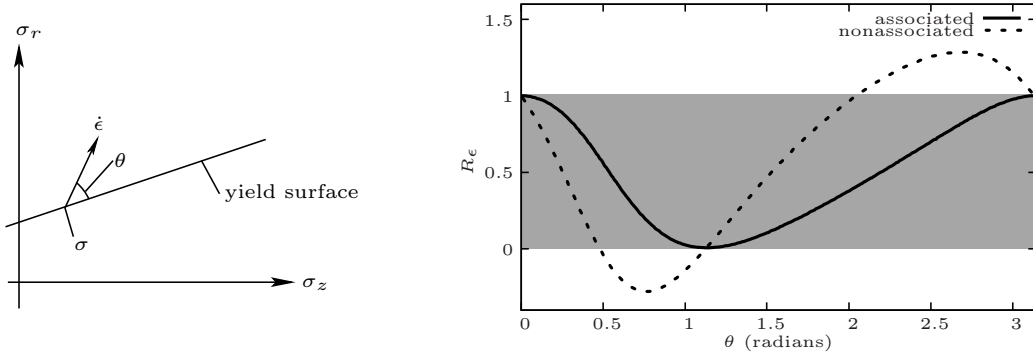
Figure 3. Directional stiffness ratio for nonhardening, associated and nonassociated linear Drucker–Prager models for all axisymmetric loading directions. Here $\sigma_z = -(1/\sqrt{3})\operatorname{Tr}(\boldsymbol{\sigma})$ and $\sigma_r = \|\boldsymbol{\sigma} - (1/3)\operatorname{Tr}(\boldsymbol{\sigma})\|$.

refined, these secondary peaks begin to form at earlier and earlier times and also grow at an increasingly rapid rate, with the result being that the numerical solution diverges with mesh refinement. The same trend was observed using several commercial finite-element codes, including DYNA3D and ABAQUS, though the formation of the secondary peaks began at a different mesh resolution with the FEM.

3. Directional stiffness

The concept of directional stiffness as developed by Runesson and Mroz [1989] is a convenient method for studying the stiffness properties of a plasticity model. The directional stiffness S_ϵ is defined so that

$$\dot{\sigma}_\epsilon = S_\epsilon \dot{\epsilon}, \tag{4}$$

where $\dot{\sigma}_\epsilon$ is the projection of the stress rate $\dot{\sigma}$ onto the direction of $\dot{\epsilon}$. The directional stiffness ratio is defined as the ratio of the plastic and elastic directional stiffness:

$$R_\epsilon = \frac{S_\epsilon}{S_\epsilon^{\mathrm{e}}} = \frac{\dot{\epsilon} : \mathbb{T} : \dot{\epsilon}}{\dot{\epsilon} : \mathbb{C} : \dot{\epsilon}}, \tag{5}$$

where S_ϵ^{e} is the elastic directional stiffness, $\mathbb{T}$ is the fourth-order elastic-plastic tangent stiffness tensor, and $\mathbb{C}$ is the fourth-order elastic tangent stiffness tensor. This quantity provides a scalar measure of the stiffness of a plasticity model relative to the corresponding elastic stiffness for a given loading direction. As shown in Figure 3, the loading direction is quantified by the loading angle θ, which is defined so that it is zero when the strain rate tensor is tangent to the yield surface. Of the two tangent directions, θ is measured from the directional tangent tensor having a negative trace (compressive).

The right-hand side of Figure 3 is a plot of the directional stiffness ratio for both associated and nonassociated, perfectly plastic, linear Drucker–Prager models for $0 \le \theta \le \pi$.

As shown in the figure, the directional stiffness ratio for an associated model is always greater than zero and less than one. However, with a nonassociated model, the directional stiffness ratio is negative for some loading directions and greater than one for others. This results in the nonassociated model exhibiting a softening-like behavior for certain loading directions, and an over-stiffening behavior for

others. The softening-like behavior occurs when the plastic directional stiffness ratio is less than zero, and corresponds to the onset of localization even while the material remains in the hardening regime [Rudnicki and Rice 1975].

In contrast to the softening-like behavior, the over-stiffening behavior of nonassociated models has seen much less study, and its effects are much more subtle. As discussed in Section 2, when the over-stiffening behavior occurs, the plastic wave speed exceeds the elastic wave speed, resulting in a loss of uniqueness of solution and the existence of a physically implausible instability. The loss of uniqueness of solution itself is problematic from a practical standpoint as it can result in mesh-dependent numerical solutions, or solutions that are very sensitive to small changes in the input parameters, as is the case with localization problems. However, in contrast to the instability seen in localization problems, the Sandler–Rubin instability is not physically plausible. Therefore, resolving the mesh-dependency arising from the Sandler–Rubin instability is not a matter of only restoring the well-posedness, but rather the plasticity model must be modified to preclude the existence of the instability.

Therefore, we draw a conclusion that a realistic plasticity model will have a directional stiffness ratio that is less than zero for some loading directions (and therefore admits localization in the hardening regime), but is never greater than one (and therefore does not admit the Sandler–Rubin instability). We now examine various modifications to the elastic perfectly plastic model considered thus far to determine which, if either, of these requisite properties each model exhibits.

4. Use of alternative theories

In what follows the case study problem is solved using the MPM with various modifications to the non-hardening plasticity model considered in the companion article. Both isotropic hardening and softening are considered, as well as three nontraditional plasticity model formulations. Each subsection describes the model reformulation as well and its effect upon the existence and characteristics of the Sandler–Rubin instability.

4.1. *Hardening and softening.* The companion paper considered only perfect plasticity and nonlinear hardening models. In this section we examine in more detail the effect of hardening, and additionally consider the effect of softening upon the Sandler–Rubin instability. Figure 4 shows the directional stiffness ratio for the modified constitutive model, including both hardening and softening. As has been pointed out by Runesson and Mroz [1989] and as witnessed by the increase in the minimum value of the directional stiffness ratio with hardening shown in Figure 4, hardening serves to diminish the softening-like behavior exhibited by nonassociated models. In fact, there exists a critical amount of hardening necessary to eliminate the possibility of attaining a negative value for the plastic directional stiffness, which in turn eliminates the possibility of localization. As would be expected, the figure shows that strain softening serves to increase the softening behavior of a nonassociated model (the minimum value of the directional stiffness ratio decreases with strain softening).

As shown in Figure 4, the maximum value of the directional stiffness ratio increases when the model includes softening. This means that the spurious stiffening caused by nonassociated models is exacerbated by softening. Therefore, softening would be expected to exacerbate the Sandler–Rubin instability. Hardening serves to slightly decrease the maximum value of the directional stiffness ratio. Therefore, hardening would be expected to ameliorate the Sandler–Rubin instability.
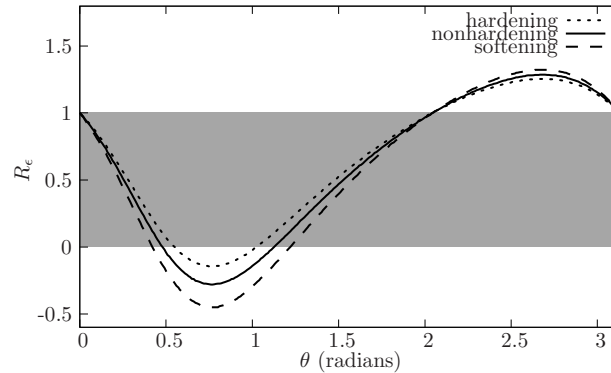
Figure 4. Directional stiffness ratio for a nonassociated model with softening, nonhardening (perfect plasticity) and hardening.

Figure 5 shows numerical solutions to the case study problem with hardening and softening. For reference, the perfect plasticity solution is also shown with dashed lines. As suggested by the increase in the maximum value of the directional stiffness ratio with softening shown in Figure 4, the plastic wave speed has increased as compared to the perfect plasticity solution. With this increase in plastic wave speed with softening, the degree of instability has also increased. In contrast, the solution with hardening shows a decrease in the plastic wave speed and a decrease in the degree of instability. It can be shown that only as the hardening modulus approaches infinity does the plastic wave speed approach the elastic wave speed. Therefore, in contrast to what was found with the localization instability, there is no critical amount of hardening or softening that eliminates the Sandler–Rubin instability. As mentioned above, in the companion paper it is shown that these same trends, along with the instability and nonuniqueness, persist with nonlinear hardening as well.

4.2. *Incrementally nonlinear plasticity.* While a large body of evidence suggests that the use of an associated flow rule is inappropriate for many materials [Spitzig et al. 1976; Lade et al. 1987], the physically implausible instability illustrated above is inherent in all nonassociated flow rules. Since both an associated and nonassociated flow rule seem to be at odds with experimental data, we ought to question the validity of the assumptions upon which both of these flow rules rest.
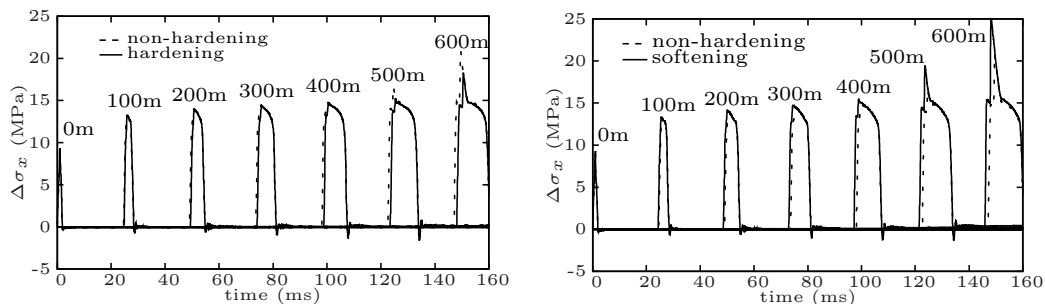
Figure 5. Stress histories for the numerical solution using hardening (left) and softening (right).

One such assumption is the existence of a *regular* flow rule. A regular flow rule is defined as one for which the direction of the plastic strain rate is independent of the direction of the strain rate itself. Of the very few studies to investigate the validity of this assumption, most have cast considerable doubt on the validity of a regular flow rule for general loading conditions [Anandarajah 1995; Tamagnini et al. 2005; Nicot and Darve 2007]. As noted above, the recent work by Rousselier et al. [2012] in polycrystalline metals plasticity, which can lead to an irregular flow rule, shows a significant improvement over macroscopic phenomenological models that use a regular flow rule. In addition to microscopic polycrystalline metals plasticity models, several macroscopic phenomenological incrementally nonlinear flow rules have been proposed in the literature [Hashiguchi 1997; Bauer 1996; Gudehus 1996; Ito 1979; Nicot and Darve 2007]. One of these, the "extended flow rule" (EFR) proposed by Hashiguchi [1997], is investigated as a possible alternative to the use of a regular rule. This flow rule was chosen since it may be easily incorporated within the basic framework of classical plasticity. The only difference is that the direction of the plastic strain rate is permitted to change based on the direction of the strain rate tensor. For this flow rule, the direction of the plastic strain rate $\boldsymbol{M}$ is given by

$$\boldsymbol{M} = \hat{\boldsymbol{N}} \|\dot{\boldsymbol{e}}^*\| + P_t^v \dot{e}_v \boldsymbol{I} + P_t^* \dot{\boldsymbol{e}}^*, \tag{6}$$

where $\hat{\boldsymbol{N}}$ is the unit normal to the yield surface, $\| : \|$ represents the Euclidean norm of its argument, $\dot{\boldsymbol{e}}^*$ is the deviatoric part of the strain rate tensor, $\dot{e}_v$ is the volumetric part of the strain rate tensor, $\boldsymbol{I}$ is the identity tensor, and P_t^v and P_t^* are fitting parameters that control the degree to which the direction of plastic strain rate will be influenced by the direction of the strain rate tensor. Taking P_t^v and P_t^* to be zero would result in a regular, associated flow rule. By selecting nonzero values for one or both of these parameters the constitutive model may be calibrated so that it accurately predicts the volumetric strain observed in triaxial compression tests, while at the same time preventing the Sandler–Rubin instability by precluding the plastic wave speed from exceeding the elastic wave speed for any loading direction.

This flow rule was implemented using the Drucker–Prager constitutive model used in the example problem, with $P_t^v = 0.5$ and $P_t^* = 0$. With these values, a triaxial compression test will result in very little volumetric plastic strain, as would be expected from a triaxial compression test on a rock-like material. The directional stiffness ratio for this model, and a perfectly plastic Drucker–Prager yield function, is shown on the left-hand side of Figure 6. For all loading directions, the directional stiffness ratio is less than one, indicating that no spurious stiffening is possible with this flow rule. The right-hand portion of this figure shows the stress histories for the case study problem with this flow rule. As expected by the boundedness of the directional stiffness ratio, no instability is evident with this flow rule. In fact the stress wave dissipates, rather than grows, as it propagates. Like a nonassociated flow rule, there are loading directions for which the directional stiffness ratio is negative. This means that this flow rule and choice of parameters will still admit localization for some loading directions. As mentioned above, the ability to localize while in the hardening regime is a desirable feature of a plasticity model.

While the EFR has the desirable attributes of disallowing the Sandler–Rubin instability, being capable of matching triaxial compression data and admitting the localization instability, such flow rules have undergone relatively little validation. Since an incrementally nonlinear flow rule is capable of *exactly* duplicating the triaxial compression response of a standard nonassociated model, triaxial compression tests alone will not validate or invalidate the EFR. The experimental measurements necessary to validate an incrementally nonlinear model are not straightforward. Additional data that measure the plastic strain
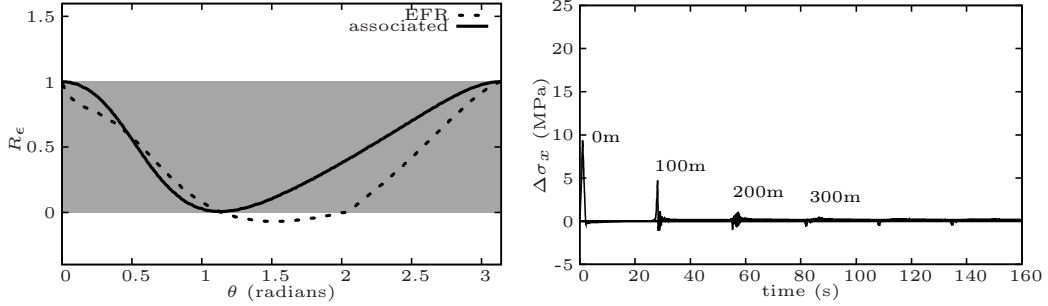
Figure 6. Left: stress histories every 100 meters through the problem domain using the extended flow rule (EFR) [Hashiguchi 1997] with $P_v = 0.5$. The wave rapidly dissipates since the plastic wave speed is less than the elastic. Right: The directional stiffness with the EFR for all axisymmetric directions. The stiffness is never greater than the elastic, but the stiffness is negative for some directions.

increments resulting from a variety of loading directions would be necessary to determine if the EFR is in fact valid. As discussed in our concluding remarks, such measurements may be critical to resolving the problems discussed in this paper, but performing such tests introduces irreducible uncertainty in the data. In the absence of such data, it would seem most prudent to choose a flow rule which disallows any nonphysical instabilities and can be fit to existing data.

4.3. *Rate-dependent plasticity.* In this section, we consider the effect of rate dependency on the existence and characteristics of the Sandler–Rubin instability. In their original work, Sandler and Rubin suggested that rate dependence might eliminate the nonphysical behavior caused by nonassociated plastic flow. The context of their suggestion was a discussion of the impacts of the Sandler–Rubin instability for quasistatic problems. The instability is inherently dynamic, but it is rational to demand that the quasistatic solution be admissible only if it is stable under infinitesimal dynamic perturbations. The conclusion is that, if a nonassociated flow rule is inappropriate for dynamic problems involving infinitesimal perturbations, then it also ought to be rejected for quasistatic problems. If rate dependence were shown to be capable of eliminating the instability for dynamic problems, then there would be no concern in using current rate-independent plasticity models for quasistatic problems.

With this motivation, the case study problem discussed above was solved using a rate-dependent generalized Duvaut–Lions overstress model. The generalized Duvaut–Lions model is an "overstress" model, meaning that, under high-rate loading, it allows the stress state to fall outside the yield surface. The "overstress" is quantified by

$$\boldsymbol{\sigma}^{\text{over}} = \boldsymbol{\sigma} - \boldsymbol{\sigma}^{\text{qs}}, \tag{7}$$

where $\boldsymbol{\sigma}^{\text{qs}}$ is the corresponding quasistatic stress state. The strain rate $\dot{\boldsymbol{\epsilon}}$ is additively decomposed into elastic ($\dot{\boldsymbol{\epsilon}}^{\text{e}}$) and viscoplastic ($\dot{\boldsymbol{\epsilon}}^{\text{vp}}$) components:

$$\dot{\boldsymbol{\epsilon}} = \dot{\boldsymbol{\epsilon}}^{\text{e}} + \dot{\boldsymbol{\epsilon}}^{\text{vp}}. \tag{8}$$

The elastic strain rate is defined to be the same as in rate-independent theory. The viscoplastic strain

rate is governed by

$$\dot{\epsilon}^{\mathrm{vp}} = \frac{1}{\tau_{\mathrm{mat}}} \mathbb{C}^{-1} : \sigma^{\mathrm{over}}, \tag{9}$$

where τ_{mat} is the plastic relaxation time, and $\mathbb{C}^{-1}$ is the inverse of the elastic tangent stiffness tensor (elastic tangent compliance tensor). The basis for this type of model is that plastic deformation requires a finite amount of time to develop. The time-scale associated with plastic deformation is quantified by τ_{mat}. For a detailed description of this model see [Brannon 2007]. For rate-dependent models it is convenient to use the nondimensional Deborah number (De) to describe the loading rate. The Deborah number is defined as

$$\mathrm{De} = \frac{\tau_{\mathrm{mat}}}{\tau_{\mathrm{load}}}, \tag{10}$$

where τ_{mat} is the material relaxation time constant, and τ_{load} is a time-scale associated with the loading. A large De indicates that the loading time-scale is short compared to the material relaxation time-scale, which would produce an elasticity-dominated response. A small De indicates that the loading time-scale is long compared to the material relaxation time-scale, which would produce a plasticity-dominated response. In the limit as $\mathrm{De} \to 0$, a viscoplastic material model would predict a material response similar to a rate-independent model. In the limit as $\mathrm{De} \to \infty$, a viscoplastic material model would predict a response that is purely elastic. Whereas, at high De, the rate-dependency will cause a viscoplastic material model to predict a more elastic-like response.

Figure 7 shows a series of plots of the stress history at various locations in the problem domain using several values of De. As discussed above, for low De, the material behavior would be expected to be similar to the rate-independent response. However, for this case study problem the solution is nonunique across the peak of the wave. This fact allows the solution in this region to change dramatically with even small changes in the material response. This is evident in the stress histories for $\mathrm{De} = 0.01$ shown in Figure 7. As would be expected, the head and tail of the wave are propagating with essentially the same speed as with the rate-independent solution (dashed line). However, the numerical solution across the peak of the wave is dramatically different than with the rate-independent model, and has become much more unstable. Again, this should not be cause for concern since no unique solution exists for this region of (x, t) space. As discussed in Section 2, the only constraints on the solution in this region are that the stress rate be greater than or equal to zero, and that the wave speed be greater than the elastic wave speed and less than the plastic wave speed. The numerical solution for $\mathrm{De} = 0.01$ shown in Figure 7 satisfies both of these constraints.

When the relaxation time is nearly the same as the loading rate, the material behavior would be expected to become more elastic. This can be seen in the stress history plots for $\mathrm{De} = 1$ shown in Figure 7. For this solution the head and tail of the wave are diverging at a much lower rate, and are propagating with a wave speed that lies between the elastic and plastic wave speeds. Because the actual stress state can transiently lie outside the yield surface with the viscoplasticity formulation used, the viscoplastic strain rate can be nonzero even when the quasistatic stress state is within the yield surface. After the quasistatic stress state enters the yield surface, the overstress will exponentially decay to zero so that the actual stress state will approach the quasistatic stress state as it moves to an elastic state. The rate at which this approach occurs depends upon the relaxation time. Therefore, when the relaxation time is of the same order as the loading rate, a large part of the tail of the wave may still be undergoing
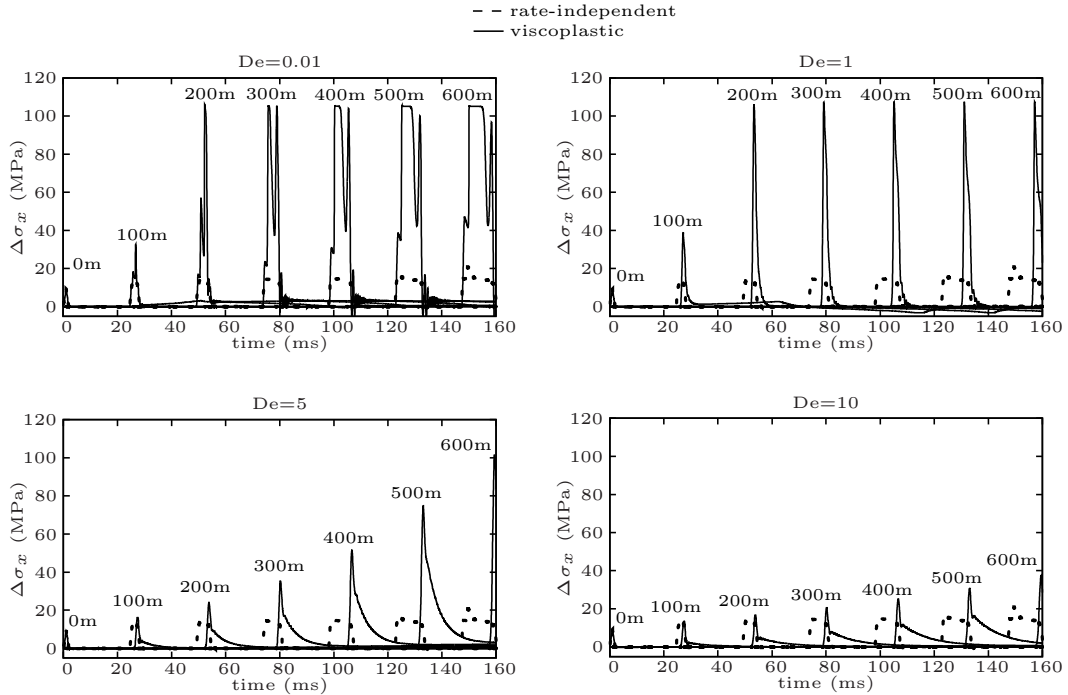
Figure 7. Stress histories for a Duvaut–Lions viscoplasticity model for De = 0.01 (top left), De = 1 (top right), De = 5 (bottom left), and De = 10 (bottom right).

viscoplastic deformation, even though the quasistatic stress state is within the yield surface. This is why the tail of the wave becomes increasingly dispersed as De increases, as seen in Figure 7. This also causes an increasing portion of the tail of the wave to be in a viscoplastic state as De increases. This also reduces the rate at which the head and tail of the wave diverge at high De, thereby decreasing the degree of instability in the solution. Also, for the mesh resolutions considered ($\Delta x = 2\,\mathrm{m}$ to $\Delta x = 0.125\,\mathrm{m}$), the numerical solutions for De > 5 seemed to converge to a unique solution, although the instability remains.

4.4. *Nonlocal plasticity.* As was mentioned in Section 1, there are two known instabilities that may arise from nonassociated plasticity models: a localization instability and the Sandler–Rubin instability. As was mentioned previously, despite the fact that these two instabilities arise from essentially opposite effects (softening-like behavior versus excessive stiffening behavior), their numerical manifestations have some similarities. With both the localization and the Sandler–Rubin instability the strain becomes unbounded inside a discrete region of space. In both cases the governing equations become ill-posed.

In the case of the localization, the instability is an actual phenomenon that a realistic model ought to admit. Nonetheless, to achieve unique solutions to localization problems, some modification of the model is required to regularize the governing equations. Two commonly used approaches to regularizing localization problems are nonlocal plasticity and gradient plasticity. Both of these modifications to traditional plasticity theory cause wave propagation to become dispersive, which means that waves of different frequencies propagate at different velocities. Dispersive wave propagation behavior has been

shown to be critical to allowing these types of models to lead to mesh-independent numerical solutions to localization problems [Sluys et al. 1993; Di Luzio and Bažant 2005].

In this section, we investigate the effect of nonlocal plasticity and the resulting dispersive wave propagation behavior on the Sandler–Rubin instability. This is done by solving our case study problem using an integral-type overlocal plasticity model as described by Strömberg and Ristinmaa [1996]. An overlocal model includes both local hardening/softening and nonlocal hardening/softening. The overlocal Drucker–Prager yield function is given by

$$f = \sqrt{J_2} + \alpha I_1 - k_o - (1-m)\eta + m\zeta, \qquad (11)$$

where η is the local hardening/softening function, ζ is the nonlocal hardening/softening function, and m is the overlocal parameter. For $m = 0$, a purely local model is obtained, and for $m = 1$ a purely nonlocal model is obtained. As discussed by both Strömberg and Ristinmaa [1996] and Di Luzio and Bažant [2005], the best localization limiting properties are obtained with the overlocal choice, $m > 1$. In this paper we use $m = 2$. The hardening/softening functions evolve according to

$$\dot{\eta}(\boldsymbol{x}) = h\dot{\lambda}(\boldsymbol{x}) \qquad (12)$$

and

$$\dot{\zeta}(\boldsymbol{x}) = \frac{h}{V_\alpha} \int_\Omega \alpha(\boldsymbol{x} - \boldsymbol{s})\dot{\lambda}(\boldsymbol{s}) \, dV, \qquad (13)$$

where $\boldsymbol{x}$ is the position vector of a given material particle, h is the hardening/softening modulus (here taken to be a constant material parameter), $V_\alpha = \int_\Omega \alpha(\boldsymbol{s}) \, dV$, and $\alpha(\boldsymbol{x})$ is the nonlocal weighting function, here chosen to be the Gaussian distribution function given by

$$\alpha(\boldsymbol{x}) = \mathrm{Exp}\big[(-k\|\boldsymbol{x}\|/l)^2\big], \qquad (14)$$

where $k = (6\sqrt{\pi})^{1/3}$, and l is the nonlocal length scale. With the nonlocal term, the yield function at each material point becomes coupled with all material points within the support of $\alpha(\boldsymbol{x})$. To solve this coupled set of equations, a new fixed-point iteration scheme (to be documented in a separate article) was developed and implemented into the MPM solution procedure.

A perturbation analysis technique described by Di Luzio and Bažant [2005], was adapted to solve for the frequency-dependent wave propagation velocity for the uniaxial strain wave propagation problem in this paper. The left-hand side of Figure 8 shows the resulting wave propagation velocity versus frequency for the nonlocal Drucker–Prager model. Unlike the dispersion relations for localization problems reported in the literature which focused on low values of the directional stiffness ratio, with the overlocal Drucker Prager model at high directional stiffness ratios no localization occurs. Hence there is no critical wave frequency at which the propagation speed is zero. This is due to the over-stiffening behavior of the nonassociated model for the loading directions involved in this problem. The wave propagation velocity is bounded by the purely local softening wave speed (upper bound) and by the purely local wave speed (lower bound). This is because with low frequencies (and therefore small gradients) the nonlocal average of the plastic strain approaches the local value, so the nonlocal model results in little change as compared to a purely local softening model. For high frequency waves the nonlocal average for a material particle will be much less than the local value since neighboring "elastic" particles, whose plastic strain rate
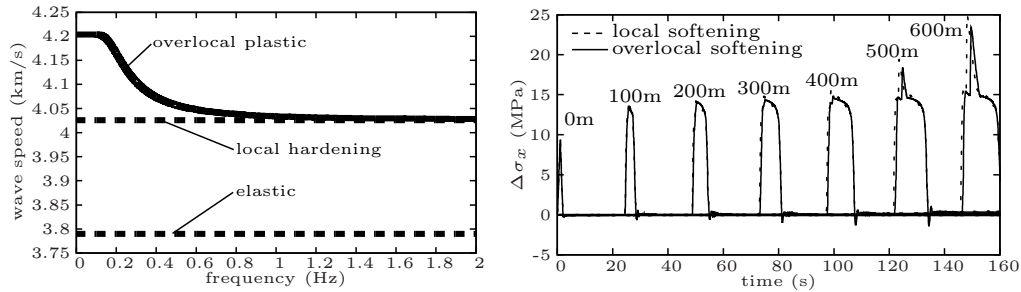
Figure 8. A plot of the frequency-dependent wave propagation velocity for the case study problem with an overlocal plasticity model, with the elastic and local hardening wave speeds shown for reference (left). Stress histories using an overlocal plasticity model with a nonlocal length scale of 1 m and a mesh resolution of 0.125 m (right).

tensor is zero, are included in the average. Therefore, for high frequencies, the local term of the overlocal hardening/softening dominates, and the response approaches that of a local hardening model.

The case study was solved using a nonlocal length scale of $l = 1.0$ m. The internal length scale is proportional to the length scale associated with a critical material microstructure. The critical material length scale depends upon the length scale associated with the problem geometry and the wave length of the solution. This case study problem is meant to represent a stress wave propagating through geologic strata. For the length scales involved and the frequency of the solution, the critical material structure driving the nonlocal length scale would likely be the thickness of bedding planes or similar geologic structures. With this in mind a nonlocal length scale of one meter would be reasonable.

The right-hand side of Figure 8 shows the stress histories at various locations in the problem domain using the overlocal model discussed above. For reference, the local softening solution is shown with a dashed line. Consistent with the dispersion plot in the same figure, the overlocal model has resulted in a reduction in the plastic wave speed relative to the local softening solution; nevertheless, the instability and nonuniqueness persist. As can be seen by the horizontal separation of the curves in Figure 8, the difference in arrival time is greater for the secondary pulse that it is for the primary pulse. This is due to the higher frequency of the secondary pulse, which, according to the dispersion relation for this problem, results in a decrease in wave speed as compared to lower frequency waves.

From the dispersion relation and the overlocal case study solution, we conclude that a nonlocal plasticity model eliminates neither the Sandler–Rubin instability nor the resulting ill-posedness.

5. Concluding remarks

Of the models considered, only Hashiguchi's incrementally nonlinear extended flow rule (EFR) [Hashiguchi 1997] eliminated the Sandler–Rubin instability. The viscoplastic model considered here resulted in mesh-independent solutions for high loading rates, but the nonphysical instability was present for all loading rates considered. Both the instability and the mesh dependency of the numerical solution were observed with both hardening and softening. Hardening was shown to diminish, but not eliminate, the instability, while softening tended to exacerbate it. The nonlocal plasticity solutions were very similar to the local plasticity solutions. Therefore, of the models considered here, the incrementally nonlinear

flow rule is the only one that may eliminate the instability while maintaining the desirable aspects of a nonassociated model.

As discussed in Section 4.2, Hashiguchi's EFR model introduces new material parameters that must be calibrated to a material of interest. To choose these parameters for a given material, the plastic strain increment must be measured for several loading directions. To measure the plastic strain increments, laboratory tests much include unloading increments. Furthermore, to measure these increments at the same material state for a different loading direction requires nonproportional loading. A limited amount of such data is available in the literature, and collecting such data is complicated by the loading-history dependent nature of plastic loading [Brannon et al. 2009].

Measuring the components of any tensor (in our case the tangent stiffness) requires measuring the response to more than one loading direction. In measuring the plastic strain increment for one loading direction, however, the material is permanently altered, making it impossible to know how the material would have responded to a different loading direction from the same initial state. Any further loading of the material with a loading increment in a different direction begins at a different material state, therefore it is impossible to measure the tangent stiffness in the laboratory with certainty. Stoughton [2002, p. 689] pointed out a few additional problems with making such measurements. Specifically, he mentioned that many materials of interest do not exhibit a "sharp" yield point, but instead the material gradually transitions from elastic to elastic/plastic deformation. This makes detecting the onset of yield difficult. Several techniques have been used to ameliorate the these problem, each with its own drawbacks [Anandarajah 1995; Tamagnini et al. 2005; Brannon et al. 2009].

The flow rule validation studies from the sheet metal forming community [Mohr et al. 2010; Dunand and Mohr 2011; Taherizadeh et al. 2010] have performed a best-fit parametrization of associated and nonassociated regular flow rule models to a subset of their experimental data. The models were then used to generate predictions for other experimental data that were not used for model calibration. As mentioned previously, these studies have shown that a nonassociated flow rule is better able to match the experimental data. Although these tests were performed for a wide variety of loading directions, none of these tests explicitly measured the plastic strain increments by including unloading increments. These and other tests already mentioned do provide a compelling case against an associated flow rule, but they do not provide any evidence for or against the validity of a regular flow rule.

To our knowledge, no study has conclusively validated or invalidated the existence of a regular flow rule. Therefore, the validity of the incrementally nonlinear approach is a critical topic for future experimental work. It is suggested that future validation efforts include incrementally nonlinear models as a possible alternative to traditional regular flow rules. Until such experimental evidence becomes available, it seems prudent to choose a model that fits known data while at the same time disallowing the nonphysical instabilities evident in traditional nonassociated plasticity. Therefore, analysts may consider adopting an incrementally nonlinear approach if an analysis involves loading paths in the directions which could potentially excite the Sandler–Rubin instability.

6. Acknowledgments

References

[Anandarajah 1995] A. Anandarajah, "Incremental stress-strain behavior of granular soil", *J. Geotech. Eng.* (*ASCE*) **121**:1 (1995), 57–68.

[Bardenhagen and Kober 2004] S. G. Bardenhagen and E. M. Kober, "The generalized interpolation material point method", *Comput. Model. Eng. Sci.* **5**:6 (2004), 477–495.

[Bauer 1996] E. Bauer, "Calibration of a comprehensive hypoplastic model for granular materials", *Soils Found.* **36**:1 (1996), 13–26.

[Bažant 1976] Z. P. Bažant, "Instability, ductility, and size effect in strain-softening concrete", *J. Eng. Mech. Div.* (*ASCE*) **102**:2 (1976), 331–344.

[Besse and Mohr 2012] C. C. Besse and D. Mohr, "Plasticity of formable all-metal sandwich sheets: Virtual experiments and constitutive modeling", *Int. J. Solids Struct.* **49**:19-20 (2012), 2863–2880.

[Bigoni 1995] D. Bigoni, "On flutter instability in elastoplastic constitutive models", *Int. J. Solids Struct.* **32**:21 (1995), 3167–3189.

[de Borst et al. 1993] R. de Borst, L. J. Sluys, H. B. Muhlhaus, and J. Pamin, "Fundamental issues in finite element analyses of localization of deformation", *Eng. Computation.* **10**:2 (1993), 99–121.

[Brannon 2007] R. M. Brannon, "Elements of phenomenological plasticity: Geometrical insight, computational algorithms, and topics in shock physics", pp. 225–274 in *Shockwave science and technology reference library*, edited by Y. Horie, Springer, Berlin, 2007.

[Brannon and Drugan 1993] R. M. Brannon and W. J. Drugan, "Influence of nonclassical elastic-plastic constitutive features on shock wave existence and spectral solutions", *J. Mech. Phys. Solids* **41**:2 (1993), 297–330.

[Brannon et al. 2009] R. Brannon, J. Burghardt, D. Bronowski, and S. Bauer, "Experimental assessment of unvalidated assumptions in classical plasticity theory", Report SAND2009-0351, Sandia National Laboratory, 2009, Available at http://tinyurl.com/brannon2009.

[Cvitanic et al. 2008] V. Cvitanic, F. Vlak, and Z. Lozina, "A finite element formulation based on non-associated plasticity for sheet metal forming", *Int. J. Plast.* **24**:4 (2008), 646–687.

[Desmorat and Marull 2011] R. Desmorat and R. Marull, "Non-quadratic Kelvin modes based plasticity criteria for anisotropic materials", *Int. J. Plast.* **27**:3 (2011), 328–351.

[Di Luzio and Bažant 2005] G. Di Luzio and Z. P. Bažant, "Spectral analysis of localization in nonlocal and over-nonlocal materials with softening plasticity or damage", *Int. J. Solids Struct.* **42**:23 (2005), 6071–6100.

[Dorgan 2006] R. J. Dorgan, "A mixed finite element implementation of a gradient-enhanced coupled damage–plasticity model", *Int. J. Damage Mech.* **15**:3 (2006), 201–235.

[Drucker 1950] D. C. Drucker, "Some implications of work hardening and ideal plasticity", *Quart. Appl. Math.* **7** (1950), 411–418.

[Dunand and Mohr 2011] M. Dunand and D. Mohr, "On the predictive capabilities of the shear modified Gurson and the modified Mohr–Coulomb fracture models over a wide range of stress triaxialities and Lode angles", *J. Mech. Phys. Solids* **59**:7 (2011), 1374–1394.

[Dunand et al. 2012] M. Dunand, A. P. Maertens, M. Luo, and D. Mohr, "Experiments and modeling of anisotropic aluminum extrusions under multiaxial loading Part I: Plasticity", *Int. J. Plast.* **36** (2012), 34–49.

[Gao et al. 2011] X. Gao, T. Zhang, J. Zhou, S. M. Graham, M. Hayden, and C. Roe, "On stress-state dependent plasticity modeling: Significance of the hydrostatic stress, the third invariant of stress deviator and the non-associated flow rule", *Int. J. Plast.* **27**:2 (2011), 217–231.

[Gudehus 1996] G. Gudehus, "Comprehensive constitutive equation for granular materials", *Soils Found.* **36**:1 (1996), 1–12.

[Hashiguchi 1997] K. Hashiguchi, "The extended flow rule in plasticity", *Int. J. Plast.* **13**:1–2 (1997), 37–58.

[Hill 1958] R. Hill, "A general theory of uniqueness and stability in elastic-plastic solids", *J. Mech. Phys. Solids* **6**:3 (1958), 236–249.

[Ito 1979] K. Ito, "New flow rule for an elastic-plastic solid based on KBW model with a view to lowering the buckling stresses of plates or shells", *Tech. Rep. Tohoku Univ.* **44**:2 (1979), 199–232.

[Lade et al. 1987] P. V. Lade, R. B. Nelson, and Y. M. Ito, "Nonassociated flow and stability of granular materials", *J. Eng. Mech. (ASCE)* **113**:9 (1987), 1302–1318.

[Mohr et al. 2010] D. Mohr, M. Dunand, and K.-H. Kim, "Evaluation of associated and non-associated quadratic plasticity models for advanced high strength steel sheets under multi-axial loading", *Int. J. Plast.* **26**:7 (2010), 939–956.

[Nicot and Darve 2007] F. Nicot and F. Darve, "Basic features of plastic strains: From micro-mechanics to incrementally nonlinear models", *Int. J. Plast.* **23**:9 (2007), 1555–1588.

[Paquet et al. 2011] D. Paquet, P. Dondeti, and S. Ghosh, "Dual-stage nested homogenization for rate-dependent anisotropic elasto-plasticity model of dendritic cast aluminum alloys", *Int. J. Plast.* **27**:10 (2011), 1677–1701.

[Popov and Lagoudas 2007] P. Popov and D. C. Lagoudas, "A 3-D constitutive model for shape memory alloys incorporating pseudoelasticity and detwinning of self-accommodated martensite", *Int. J. Plast.* **23**:10–11 (2007), 1679–1720.

[Rousselier et al. 2012] G. Rousselier, M. Luo, and D. Mohr, "Macroscopic plasticity modeling of anisotropic aluminum extrusions using a reduced texture methodology", *Int. J. Plast.* **30–31** (2012), 144–165.

[Rudnicki and Rice 1975] J. Rudnicki and J. R. Rice, "Conditions for the localization of deformation in pressure-sensitive dilatant materials", *J. Mech. Phys. Solids* **23**:6 (1975), 371–394.

[Runesson and Mroz 1989] K. Runesson and Z. Mroz, "A note on nonassociated plastic flow rules", *Int. J. Plast.* **5**:6 (1989), 639–658.

[Saint-Sulpice et al. 2009] L. Saint-Sulpice, S. A. Chirani, and S. Calloch, "A 3D super-elastic model for shape memory alloys taking into account progressive strain under cyclic loadings", *Mech. Mater.* **41**:1 (2009), 12–26.

[Saleeb et al. 2011] A. F. Saleeb, S. A. P. II, and A. Kumar, "A multi-axial, multimechanism based constitutive model for the comprehensive representation of the evolutionary response of SMAs under general thermomechanical loading conditions", *Int. J. Plast.* **27**:5 (2011), 655–687.

[Sandler and Rubin 1987] I. S. Sandler and D. Rubin, "The consequences of non-associated plasticity in dynamic problems", pp. 345–353 in *Constitutive laws for engineering materials* (Tucson, AZ), edited by C. Desai, Elsevier, Amsterdam, 1987.

[Shen et al. 2012] W. Q. Shen, J. F. Shao, D. Kondo, and B. Gatmiri, "A micro-macro model for clayey rocks with a plastic compressible porous matrix", *Int. J. Plast.* **36** (2012), 64–85.

[Sluys et al. 1993] L. J. Sluys, R. de Borst, and H. B. Huhlhaus, "Wave propagation, localization and dispersion in a gradient-dependent medium", *Int. J. Solids Struct.* **30**:9 (1993), 1153–1171.

[Spitzig et al. 1976] W. A. Spitzig, R. J. Sober, and O. Richmond, "The effect of hydrostatic pressure on the deformation behavior of maraging and HY-80 steels and its implications for plasticity theory", *Metall. Trans. A* **7**:11 (1976), 1703–1710.

[de St. Germain et al. 2000] J. D. de St. Germain, J. McCorquodale, S. G. Parker, and C. R. Johnson, "Uintah: A massively parallel problem solving environment", pp. 33–41 in *Ninth IEEE international symposium on high performance and distributed computing* (Pittsburgh, PA, 2000), edited by B. Werner, IEEE, Piscataway, NJ, 2000.

[Stoughton 2002] T. B. Stoughton, "A non-associated flow rule for sheet metal forming", *Int. J. Plast.* **18**:5–6 (2002), 687–714.

[Stoughton and Yoon 2006] T. B. Stoughton and J. W. Yoon, "Review of Drucker's postulate and the issue of plastic stability in metal forming", *Int. J. Plast.* **22**:3 (2006), 391–433.

[Stoughton and Yoon 2008] T. B. Stoughton and J. W. Yoon, "On the existence of indeterminate solutions to the equations of motion under non-associated flow", *Int. J. Plast.* **24**:4 (2008), 583–613.

[Strömberg and Ristinmaa 1996] L. Strömberg and M. Ristinmaa, "FE-formulation of a nonlocal plasticity theory", *Comput. Methods Appl. Mech. Eng.* **136**:1-2 (1996), 127–144.

[Sulsky et al. 1994] D. Sulsky, Z. Chen, and H. L. Schreyer, "A particle method for history-dependent materials", *Comput. Methods Appl. Mech. Eng.* **118**:1-2 (1994), 179–196.

[Taherizadeh et al. 2010] A. Taherizadeh, D. E. Green, A. Ghaei, and J.-W. Yoon, "A non-associated constitutive model with mixed iso-kinematic hardening for finite element simulation of sheet metal forming", *Int. J. Plast.* **26**:2 (2010), 288–309.

[Tamagnini et al. 2005] C. Tamagnini, F. Calvetti, and G. Viggiani, "An assessment of plasticity theories for modeling the incrementally nonlinear behavior of granular soils", *J. Eng. Math.* **52**:1-3 (2005), 265–291.

[Valanis 1998] K. C. Valanis, "Diffusion potential and well-posedness in non-associative plasticity", *Int. J. Solids Struct.* **35**:36 (1998), 5173–5188.

JEFFREY BURGHARDT: `jburghardt@slb.com`
Schlumberger, 1935 S. Fremont Dr., Salt Lake City, UT 84104, United States

REBECCA M. BRANNON: `rebecca.brannon@utah.edu`
University of Utah, 50 S. Campus Dr., Salt Lake City, UT 84108, United States

msp

PERIDYNAMICS FOR ANTIPLANE SHEAR AND TORSIONAL DEFORMATIONS

SELDA OTERKUS AND ERDOGAN MADENCI

A rod or beam is one of the most widely used members in engineering construction. Such members must be properly designed to resist the applied loads. When subjected to antiplane (longitudinal) shear and torsional loading, homogeneous, isotropic, and elastic materials are governed by the Laplace equation in two dimensions under the assumptions of classical continuum mechanics, and are considerably easier to solve than their three-dimensional counterparts. However, when using the finite element method in conjunction with linear elastic fracture mechanics, crack nucleation and its growth still pose computational challenges, even under such simple loading conditions. This difficulty is mainly due to the mathematical structure of its governing equations, which are based on the local classical continuum theory. However, the nonlocal peridynamic theory is free of these challenges because its governing equations do not contain any spatial derivatives of the displacement components, and thus are valid everywhere in the material. This study presents the peridynamic equation of motion for antiplane shear and torsional deformations, as well as the peridynamic material parameters. After establishing the validity of this equation, solutions for specific components that are weakened by deep edge cracks and internal cracks are presented.

1. Introduction

Prediction of structural failure loads due to crack nucleation and propagation is still a challenging area of solid mechanics. Many different techniques are proposed and widely used within the scope of classical continuum mechanics. The traditional approaches to predict failure usually employ concepts from linear elastic fracture mechanics (LEFM). The major drawback of LEFM is the requirement of a preexisting initial crack in the structure. Hence, it is not capable of predicting crack nucleation. Furthermore, the mathematical formulation results in unphysical (singular) stress values at the crack tips. To overcome these problems, cohesive zone models (CZM) and extended finite element methods (XFEM) are widely accepted as an alternative and implemented in the commercially available finite element analysis programs.

Although relatively new, peridynamics (PD), introduced by Silling [2000] by reformulating the classical continuum mechanics equations, is very suitable for failure analysis of structures because it allows cracks to grow naturally without resorting to external crack growth laws. PD is based on integrodifferential equations as opposed to the partial differential equations of classical continuum mechanics. An extensive literature survey on peridynamics is given by Madenci and Oterkus [2014]. A comparison study between peridynamics, CZM, and XFEM techniques by Agwai et al. [2011] highlights the capability of the PD theory. They showed that the crack speeds obtained from all three approaches are of the same order; however, the fracture paths obtained through the PD theory are much closer to the experimental results than those of the other two techniques.
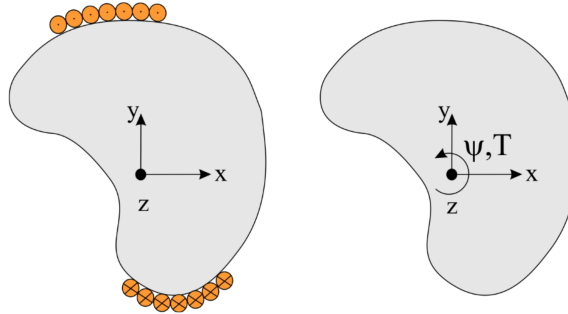
Figure 1. A beam under (left) antiplane shear and (right) torsion.

The numerical simulation of three-dimensional structures can be computationally costly. Although all structures are three-dimensional in nature, they can be idealized under certain assumptions. Under such idealization, a rod or a beam subjected to antiplane (longitudinal) shear and torsional loading can be analyzed in two dimensions. However, the PD equation of motion and the PD material parameter must reflect these idealizations. In connection to Linear Elastic Fracture Mechanics (LEFM), Lipton [2014] investigated Mode III fracture in the context of antiplane shear deformation.

As shown in Figure 1, this study presents the derivation of the PD equation of motion for antiplane shear and torsional deformations of beams with arbitrary cross-sections along with the implementation of boundary conditions. Also, it describes the determination of peridynamic material parameter in terms of shear modulus, and critical stretch in terms of critical energy release rate for tearing mode. After establishing its validity by comparing against benchmark solutions, a study of components that are weakened by deep edge cracks and internal cracks is presented.

In multiphysics analysis, many the field equations concern the solution of diffusion equation. This study also provides the framework to consider such equations with defects and stationary or moving dissimilar material interface. The partial differential equations of the classical theory cannot be applied directly to defects. This incompatibility has led to a variety of patches in the finite element method. They are entirely unnecessary with peridynamics.

2. Kinematics for antiplane shear and torsional deformation

Due to the nature of loading and the geometry of the components, the deformation of the cross-section on the z-plane is dependent only on the x- and y-coordinates. Also, the cross-section of the component remains uniform. At any instant of time, every point in the material denotes the location of a material particle, and these infinitely many material points (particles) constitute the continuum. In the undeformed state of the body, each material point is identified by its coordinates, $\boldsymbol{x}_{(k)}$ with ($k = 1, 2, \ldots, \infty$), and is associated with an incremental volume, $V_{(k)}$, and a mass density of $\rho(\boldsymbol{x}_{(k)})$. Each material point can be subjected to prescribed body loads, displacement, or velocity, resulting in motion and deformation.

According to the PD theory introduced by Silling [2000], the motion of a body is analyzed by considering the interaction of a material point, $\boldsymbol{x}_{(k)}$, with the other, possibly infinitely many, material points, $\boldsymbol{x}_{(j)}$, with ($j = 1, 2, \ldots, \infty$), in the body. Therefore, an infinite number of interactions may exist between the material point at location $\boldsymbol{x}_{(k)}$ and other material points. However, the influence of the material points
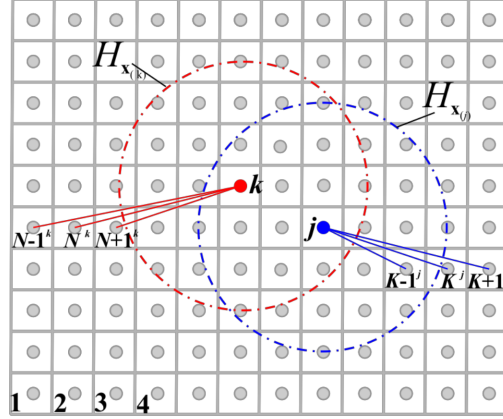
Figure 2. Peridynamic material points and their interaction with each other.

interacting with $x_{(k)}$ is assumed to vanish beyond a local region (horizon), denoted by $H_{x_{(k)}}$, shown in Figure 2. Similarly, the material point $x_{(j)}$ interacts with the other material points in its own family, $H_{x_{(j)}}$. The range of the material point $x_{(k)}$ is defined by δ, referred to as the "horizon." Also, the material points within a distance δ of $x_{(k)}$ are called the family of $x_{(k)}$, $H_{x_{(k)}}$. The interaction of material points is prescribed through the micropotentials that depend on the deformation and constitutive properties of the material.

As shown in Figure 2, material point $x_{(k)}$ interacts with its family of material points, $H_{x_{(k)}}$, and is influenced by the collective deformation of all these material points. Similarly, the material point $x_{(j)}$ is influenced by deformation of the material points, $H_{x_{(j)}}$, in its own family. In Figure 2, the material points, $x_{(k)}$ and $x_{(j)}$ associated with designated as N^k and K^j with N and K denoting the sequence of material points in the domain.

With respect to a Cartesian coordinate system, the material point $x_{(k)}^T = \{x_{(k)}, y_{(k)}, z_{(k)}\}$ experiences displacement, $u_{(k)}^T = \{u_{(k)}, v_{(k)}, w_{(k)}\}$, and its location is described by the position vector $y_{(k)} = x_{(k)} + u_{(k)}$ in the deformed state, as shown in Figure 3. The body load vector at material point $x_{(k)}$ is represented by $b_{(k)}^T = \{0, 0, b_{z(k)}\}$, respectively. The motion of a material point conforms to the Lagrangian description. In the deformed configuration, the material points $x_{(k)}$ and $x_{(j)}$ experience displacements $u_{(k)}$ and $u_{(j)}$, respectively. Their initial relative position vector $(x_{(j)} - x_{(k)})$ prior to deformation becomes $(y_{(j)} - y_{(k)})$ after deformation.

Under antiplane and torsional loadings, the initial position of material points $x_{(j)}$ and $x_{(k)}$ for $z = z_{(j)} = z_{(k)}$ can be defined as $x_{(j)}^T = \{x_{(j)}, y_{(j)}, z\}$ and $x_{(k)}^T = \{x_{(k)}, y_{(k)}, z\}$. Their initial relative position can then be expressed as

$$(x_{(j)}^T - x_{(k)}^T) = \{(x_{(j)} - x_{(k)}), (y_{(j)} - y_{(k)}), 0\}. \tag{1}$$

For antiplane shear deformation, these material points experience the displacements $u_{(j)}^T = \{0, 0, u_{z(j)}\}$ and $u_{(k)}^T = \{0, 0, u_{z(k)}\}$. Their relative position in the deformed state becomes

$$y_{(j)} - y_{(k)} = x_{(j)} - x_{(k)} + (u_{z(j)} - u_{z(k)})e_z. \tag{2}$$
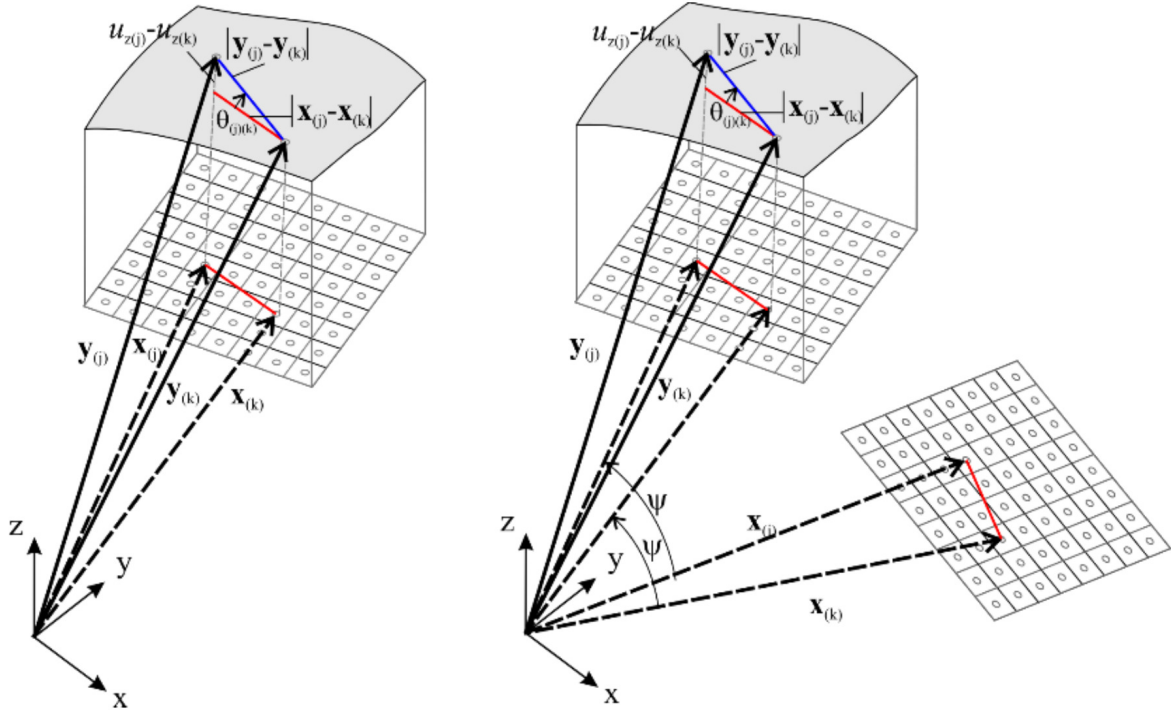
Figure 3. Kinematics of peridynamic material points on the cross-section: (left) anti-plane shear deformation, and (right) torsional deformation.

For torsional deformation, these material points experience the displacements $\boldsymbol{u}^T_{(j)} = \{-\psi z y_{(j)}, \psi z x_{(j)}, u_{z(j)}\}$ and $\boldsymbol{u}^T_{(k)} = \{-\psi z y_{(k)}, \psi z x_{(k)}, u_{z(k)}\}$, in which ψ represents the angle of twist. Their relative position can be expressed as

$$\boldsymbol{y}_{(j)} - \boldsymbol{y}_{(k)} = \boldsymbol{x}_{(j)} - \boldsymbol{x}_{(k)} + \Omega \times (\boldsymbol{x}_{(j)} - \boldsymbol{x}_{(k)}) + (u_{z(j)} - u_{z(k)})\boldsymbol{e}_z, \tag{3}$$

in which $\Omega^T = \{0, 0, \psi z\}$, and the product term $\Omega \times (\boldsymbol{x}_{(j)} - \boldsymbol{x}_{(k)})$ represents the rotation of $(\boldsymbol{x}_{(j)} - \boldsymbol{x}_{(k)})$ around the z-axis, resulting in no deformation.

As shown in Figure 3, the relative out-of-plane displacement (elevation) of material points $\boldsymbol{x}_{(j)}$ and $\boldsymbol{x}_{(k)}$ is defined as

$$e_{(k)(j)} = u_{z(j)} - u_{z(k)}. \tag{4}$$

Also, under small deformations, the slope of this elevation (change in angle) between material points $\boldsymbol{x}_{(k)}$ and $\boldsymbol{x}_{(j)}$ is defined as

$$r_{(k)(j)} = \frac{e_{(k)(j)}}{\xi_{(k)(j)}} = \frac{u_{z(j)} - u_{z(k)}}{\xi_{(k)(j)}} \tag{5}$$

where $\xi_{(k)(j)} = |\boldsymbol{x}_{(j)} - \boldsymbol{x}_{(k)}|$ represents the distance between these material points.

3. Ordinary state-based peridynamics

Due to the interaction between material points $x_{(k)}$ and $x_{(j)}$, a scalar-valued micropotential, $w_{(k)(j)}$, develops; it depends on the material properties, as well as the elevation, $e_{(k)(j)}$, between point $x_{(k)}$ and all other material points in its family. Note that $w_{(j)(k)} \neq w_{(k)(j)}$ because $w_{(j)(k)}$ depends on the state of material points within the family of material point $x_{(j)}$. These micropotentials can be expressed as

$$w_{(k)(j)} = w_{(k)(j)}(e_{(1^k)(k)}, e_{(2^k)(k)}, \dots) \quad \text{and} \quad w_{(j)(k)} = w_{(j)(k)}(e_{(1^j)(j)}, e_{(2^j)(j)}, \dots), \tag{6}$$

in which $e_{(j)(k)} = u_{z(j)} - u_{z(k)}$ represents elevation between material points $x_{(k)}$ and $x_{(j)}$. The change in elevation, $e_{(m^k)(k)}$, is measured between point $x_{(k)}$ and the m-th material point that interacts with point $x_{(k)}$. Similarly, $e_{(m^j)(j)}$ is measured between point $x_{(j)}$ and the m-th material point that interacts with point $x_{(j)}$, as shown in Figure 2. The strain energy density, $W_{(k)}$, of material point $x_{(k)}$ can be expressed as a summation of all the micropotentials, $w_{(k)(j)}$, arising from the interaction of material point $x_{(k)}$ and the other material points, $x_{(j)}$, within its horizon in the form

$$W_{(k)} = \frac{1}{2} \sum_{j=1}^{\infty} \frac{1}{2} \Big[w_{(k)(j)}(e_{(1^k)(k)}, e_{(2^k)(k)}, \dots) + w_{(j)(k)}(e_{(1^j)(j)}, e_{(2^j)(j)}, \dots) \Big] V_{(j)}, \tag{7}$$

in which $w_{(k)(j)} = 0$ for $k = j$.

The PD equation of motion at material point $x_{(k)}$ can be derived by applying the principle of virtual work, i.e.,

$$\delta \int_{t_0}^{t_1} (T - U)\, dt = 0, \tag{8}$$

where T and U represent the total kinetic and potential energies in the body. This principle is satisfied by solving for the Euler–Lagrange equation

$$\frac{d}{dt}\left(\frac{\partial L}{\partial \dot{u}_{z(k)}} \right) - \frac{\partial L}{\partial u_{z(k)}} = 0 \tag{9}$$

where the Lagrangian L is defined as $L = T - U$.

The total kinetic and potential energies in the body can be obtained by summation of kinetic and potential energies of all material points, respectively,

$$T = \sum_{i=1}^{\infty} \frac{1}{2}\rho_{(i)} \dot{u}_{z(i)} \dot{u}_{z(i)} V_{(i)} \quad \text{and} \quad U = \sum_{i=1}^{\infty} W_{(i)} V_{(i)} - \sum_{i=1}^{\infty} (b_{z(i)} u_{z(i)}) V_{(i)}. \tag{10a}$$

Substituting for the strain energy density, $W_{(i)}$, of material point $x_{(i)}$ from (7), the potential energy can be rewritten as

$$U = \sum_{i=1}^{\infty} \left\{ \frac{1}{2} \sum_{j=1}^{\infty} \frac{1}{2} \Big[w_{(i)(j)}(e_{(1^i)(i)}, e_{(2^i)(i)}, \dots) + w_{(j)(i)}(e_{(1^j)(j)}, e_{(2^j)(j)}, \dots) \Big] V_{(j)} - (b_{z(i)} u_{z(i)}) \right\} V_{(i)}. \tag{11}$$

The Lagrangian can be written in an expanded form by showing only the terms associated with the material point $x_{(k)}$ as

$$L = \cdots + \tfrac{1}{2}\rho_{(k)}\dot{u}_{z(k)}\dot{u}_{z(k)}V_{(k)} + \cdots$$

$$\cdots - \frac{1}{2}\sum_{j=1}^{\infty}\left\{\tfrac{1}{2}\big[w_{(k)(j)}(e_{(1^k)(k)}, e_{(2^k)(k)}, \dots) + w_{(j)(k)}(e_{(1^j)(j)}, e_{(2^j)(j)}, \dots)\big]V_{(j)}\right\}V_{(k)} \cdots$$

$$\cdots - \frac{1}{2}\sum_{i=1}^{\infty}\left\{\tfrac{1}{2}\big[w_{(i)(k)}(e_{(1^i)(i)}, e_{(2^i)(i)}, \dots) + w_{(k)(i)}(e_{(1^k)(k)}, e_{(2^k)(k)}, \dots)\big]V_{(i)}\right\}V_{(k)} \cdots$$

$$\cdots + (b_{z(k)}u_{z(k)})V_{(k)} \cdots \tag{12a}$$

or

$$L = \cdots + \tfrac{1}{2}\rho_{(k)}\dot{u}_{z(k)}\dot{u}_{z(k)}V_{(k)} + \cdots$$

$$\cdots - \frac{1}{2}\sum_{j=1}^{\infty}\{w_{(k)(j)}(e_{(1^k)(k)}, e_{(2^k)(k)}, \dots)V_{(j)}V_{(k)}\} \cdots$$

$$\cdots - \frac{1}{2}\sum_{j=1}^{\infty}\{w_{(j)(k)}(e_{(1^j)(j)}, e_{(2^j)(j)}, \dots)V_{(j)}V_{(k)}\} \cdots$$

$$\cdots + (b_{z(k)}u_{z(k)})V_{(k)} \cdots . \tag{12b}$$

Substituting from (12b) into (9) results in the Euler–Lagrange equation of the material point $x_{(k)}$ as

$$\rho_{(k)}\ddot{u}_{z(k)}V_{(k)} + \left(\sum_{j=1}^{\infty}\frac{1}{2}\left(\sum_{i=1}^{\infty}\frac{\partial w_{(k)(j)}}{\partial(u_{z(j)}-u_{z(k)})}V_{(i)}\right)\frac{\partial(u_{z(j)}-u_{z(k)})}{\partial u_{z(k)}}\right.$$

$$\left. + \sum_{j=1}^{\infty}\frac{1}{2}\left(\sum_{i=1}^{\infty}\frac{\partial w_{(j)(k)}}{\partial(u_{z(k)}-u_{z(j)})}V_{(i)}\right)\frac{\partial(u_{z(k)}-u_{z(j)})}{\partial u_{z(k)}} - b_{z(k)}\right)V_{(k)} = 0 \tag{13a}$$

or

$$\rho_{(k)}\ddot{u}_{z(k)} = \sum_{j=1}^{\infty}\frac{1}{2}\left(\sum_{i=1}^{\infty}\frac{\partial w_{(k)(j)}}{\partial(u_{z(j)}-u_{z(k)})}V_{(i)}\right) - \sum_{j=1}^{\infty}\frac{1}{2}\left(\sum_{i=1}^{\infty}\frac{\partial w_{(j)(k)}}{\partial(u_{z(k)}-u_{z(j)})}V_{(i)}\right) + b_{z(k)} = 0, \tag{13b}$$

in which it is assumed that the interactions not involving material point $x_{(k)}$ do not have any effect on material point $x_{(k)}$. Based on the dimensional analysis of this equation, it is apparent that the quantity $\sum_{i=1}^{\infty}V_{(i)}\partial w_{(k)(i)}/\partial(u_{z(j)}-u_{z(k)})$ represents the force density in the z-direction that material point $x_{(j)}$ exerts on material point $x_{(k)}$ and the quantity $\sum_{i=1}^{\infty}V_{(i)}\partial w_{(k)(i)}/\partial(u_{z(k)}-u_{z(j)})$ represents the force density in the z-direction that material point $x_{(k)}$ exerts on material point $x_{(j)}$. With this interpretation, (13b) can be rewritten as

$$t_{z(k)(j)}(e_{(j)(k)}, x_{(j)} - x_{(k)}, t) = \frac{1}{2}\frac{1}{V_{(j)}}\sum_{i=1}^{\infty}\frac{\partial w_{(k)(i)}}{\partial(u_{z(j)}-u_{z(k)})}V_{(i)}, \tag{14a}$$

and

$$t_{z(j)(k)}(e_{(k)(j)}, x_{(k)} - x_{(j)}, t) = \frac{1}{2}\frac{1}{V_{(j)}}\sum_{i=1}^{\infty}\frac{\partial w_{(i)(k)}}{\partial(u_{z(k)}-u_{z(j)})}V_{(i)}, \tag{14b}$$

in which $V_{(j)}$ represents the volume of material point $\boldsymbol{x}_{(j)}$. The material point $\boldsymbol{x}_{(j)}$ exerts the force density $t_{z(k)(j)}$ on material point $\boldsymbol{x}_{(k)}$.

By utilizing the state concept described by Silling et al. [2007] and Silling and Lehoucq [2010], the force densities $t_{z(k)(j)}$ and $t_{z(j)(k)}$ can be stored in force scalar states that belong to material points $\boldsymbol{x}_{(k)}$ and $\boldsymbol{x}_{(j)}$, respectively, as

$$\underline{t}_z(\boldsymbol{x}_{(k)}, t) = \left\{\begin{array}{c} \vdots \\ t_{z(k)(j)} \\ \vdots \end{array}\right\} \quad \text{and} \quad \underline{t}_z(\boldsymbol{x}_{(j)}, t) = \left\{\begin{array}{c} \vdots \\ t_{z(j)(k)} \\ \vdots \end{array}\right\}. \tag{15}$$

The force densities $t_{z(k)(j)}$ and $t_{z(j)(k)}$ stored in scalar states $\underline{t}_z(\boldsymbol{x}_{(k)}, t)$ and $\underline{t}_z(\boldsymbol{x}_{(j)}, t)$ can be extracted again by operating the force states on the corresponding initial relative position vectors, $(\boldsymbol{x}_{(j)} - \boldsymbol{x}_{(k)})$ and $(\boldsymbol{x}_{(k)} - \boldsymbol{x}_{(j)})$, as

$$t_{z(k)(j)} = \underline{t}_z(\boldsymbol{x}_{(k)}, t)\langle \boldsymbol{x}_{(j)} - \boldsymbol{x}_{(k)}\rangle \quad \text{and} \quad t_{z(j)(k)} = \underline{t}_z(\boldsymbol{x}_{(j)}, t)\langle \boldsymbol{x}_{(k)} - \boldsymbol{x}_{(j)}\rangle. \tag{16}$$

By using (14a)–(14b), the Euler–Lagrange equation of the material point $\boldsymbol{x}_{(k)}$ can be recast as

$$\rho_{(k)}\ddot{u}_{z(k)} = \sum_{j=1}^{\infty}\left[t_{z(k)(j)}(e_{(j)(k)}, \boldsymbol{x}_{(j)} - \boldsymbol{x}_{(k)}, t) - t_{z(j)(k)}(e_{(k)(j)}, \boldsymbol{x}_{(k)} - \boldsymbol{x}_{(j)}, t)\right]V_{(j)} + b_{z(k)}. \tag{17}$$

Because the area of each material point $V_{(j)}$ is infinitesimally small, for the limiting case of $V_{(j)} \to 0$, the infinite summation can be expressed as a Riemann integral while considering only the material points within the horizon. Therefore, (17) can be rewritten in integral equation form as

$$\rho\ddot{u}_z = \int_H \left[t_z(u'_{(z)} - u_{(z)}, \boldsymbol{x}' - \boldsymbol{x}, t) - t'_z(u_{(z)} - u'_{(z)}, \boldsymbol{x} - \boldsymbol{x}', t)\right]dV_{x'} + b_z \tag{18}$$

in which $u_{(z)}$ and $u'_{(z)}$ represent the transverse displacement at material points $\boldsymbol{x}$ and $\boldsymbol{x}'$, respectively. Depending on the boundary conditions, the solution to this equation provides either the antiplane or torsional deformation.

3.1. *Peridynamic force density.* The force densities at material points $\boldsymbol{x}_{(k)}$ and $\boldsymbol{x}_{(j)}$ can be defined in the form

$$t_{z(k)(j)}(e_{(j)(k)}, \boldsymbol{x}_{(j)} - \boldsymbol{x}_{(k)}, t) = \tfrac{1}{2}A_{(k)(j)} \quad \text{and} \quad t_{z(j)(k)}(e_{(k)(j)}, \boldsymbol{x}_{(k)} - \boldsymbol{x}_{(j)}, t) = -\tfrac{1}{2}B_{(k)(j)}, \tag{19}$$

where $A_{(k)(j)}$ and $B_{(k)(j)}$ are auxiliary parameters that are dependent on engineering material constants, the deformation field, and the horizon.

In light of the definition (14) of the expressions for force density in terms of micropotentials, the force density vectors can be related to the strain energy density function, $W_{(k)}$, at material point $\boldsymbol{x}_{(k)}$ as

$$t_{z(k)(j)}(u_{z(j)} - u_{z(k)}, \boldsymbol{x}_{(j)} - \boldsymbol{x}_{(k)}, t) = \frac{1}{V_{(j)}}\frac{\partial W_{(k)}}{\partial(u_{z(j)} - u_{z(k)})}, \tag{20a}$$

$$t_{z(j)(k)}(u_{z(k)} - u_{z(j)}, \boldsymbol{x}_{(k)} - \boldsymbol{x}_{(j)}, t) = \frac{1}{V_{(k)}}\frac{\partial W_{(j)}}{\partial(u_{z(k)} - u_{z(j)})}. \tag{20b}$$

However, the determination of the auxiliary parameters, $A_{(k)(j)}$ and $B_{(k)(j)}$, requires an explicit form of the strain energy density function.

3.2. *Peridynamic material parameters.*

For an isotropic and elastic material experiencing antiplane and torsional deformation, the classical expression for the strain energy density, $W_{(k)}$, at material point $\boldsymbol{x}_{(k)}$ can be written as

$$W_{(k)} = \tfrac{1}{2}\mu[\gamma_{(k)xz}^2 + \gamma_{(k)yz}^2] \tag{21}$$

in which μ is the shear modulus of the material, and $\gamma_{(k)xz}$ and $\gamma_{(k)yz}$ are the transverse shear strain components at material point $\boldsymbol{x}_{(k)}$.

Analogous to (21), the PD representation of the strain energy density, $W_{(k)}$, at material point $\boldsymbol{x}_{(k)}$ can be expressed as

$$W_{(k)} = a[r_{(k)xz}^2 + r_{(k)yz}^2], \tag{22}$$

in which a is the ordinary state-based PD material parameter for strain energy and $r_{(k)xz}$ and $r_{(k)yz}$ are defined in the form

$$r_{(k)xz} = b\sum_{j=1}^{N} w_{(k)(j)}e_{(j)(k)}\cos\theta_{(k)(j)}V_{(j)} \quad\text{and}\quad r_{(k)yz} = b\sum_{j=1}^{N} w_{(k)(j)}e_{(j)(k)}\sin\theta_{(k)(j)}V_{(j)}, \tag{23}$$

in which $\cos\theta_{(k)(j)} = (x_{(j)} - x_{(k)})/\xi_{(k)(j)}$ and $\sin\theta_{(k)(j)} = (y_{(j)} - y_{(k)})/\xi_{(k)(j)}$, N represents the number of material points within the family of $\boldsymbol{x}_{(k)}$, and b is a PD parameter. The nondimensional influence function, which can be taken in the form of $w_{(k)(j)} = \delta/\xi_{(k)(j)}$, provides a means to control the influence of material points away from the current material point at $\boldsymbol{x}_{(k)}$. The infinitesimal volume of the material point $\boldsymbol{x}_{(j)}$ is denoted by $V_{(j)} = \ell\xi_{(k)(j)}\Delta\xi_{(k)(j)}\Delta\theta_{(k)(j)}$, where $\Delta\xi_{(k)(j)}$ and $\Delta\theta_{(k)(j)}$ represent the incremental distance and angle between material points $\boldsymbol{x}_{(k)}$ and $\boldsymbol{x}_{(j)}$ and ℓ is the length of the component.

As the horizon approaches zero, the out-of-plane displacement at material point $\boldsymbol{x}_{(j)}$ can be expressed by using a Taylor series expansion as

$$u_{z(j)} - u_{z(k)} = u_{z(k),x}\xi_{(k)(j)}\cos\theta_{(k)(j)} + u_{z(k),y}\xi_{(k)(j)}\sin\theta_{(k)(j)} + \tfrac{1}{2}u_{z(k),xx}\xi_{(k)(j)}^2\cos^2\theta_{(k)(j)}$$
$$+ u_{z(k),xy}\xi_{(k)(j)}^2\cos\theta_{(k)(j)}\sin\theta_{(k)(j)} + \tfrac{1}{2}u_{z(k),yy}\xi_{(k)(j)}^2\sin^2\theta_{(k)(j)}. \tag{24}$$

Substituting from (24) into (23) along with the infinitesimal volume and influence function, performing algebraic manipulations, and converting the summations to integrations lead to

$$r_{(k)xz} = b\frac{\ell\pi\delta^3}{2}u_{z(k),x} \quad\text{and}\quad r_{(k)yz} = b\frac{\ell\pi\delta^3}{2}u_{z(k),y}. \tag{25}$$

Defining $b = 2/(\ell\pi\delta^3)$ reduces $r_{(k)xz}$ and $r_{(k)yz}$ to the classical transverse shear strains $\gamma_{(k)xz}$ and $\gamma_{(k)yz}$; thus, equating the peridynamic and classical strain energy density, $W_{(k)}$, at material point $\boldsymbol{x}_{(k)}$ results in

$$W_{(k)} = a[r_{(k)xz}^2 + r_{(k)yz}^2] = \tfrac{1}{2}\mu[\gamma_{(k)xz}^2 + \gamma_{(k)yz}^2]. \tag{26}$$

It yields the ordinary state-based peridynamic material parameter for strain energy as

$$a = \tfrac{1}{2}\mu, \tag{27}$$

which is not dependent on the horizon, unlike the parameter b. The parameters, $r_{(k)xz}$ and $r_{(k)yz}$, can be viewed as the peridynamic transverse shear angles.

3.3. *Force density-displacement relation.* Substituting for $W_{(k)}$ in (20) and differentiating, the force density, $t_{z(k)(j)}$, can be obtained as

$$t_{z(k)(j)}(u_{z(j)} - u_{z(k)}, \boldsymbol{x}_{(j)} - \boldsymbol{x}_{(k)}, t) = \mu \left[w_{(k)(j)} \frac{x_{(j)} - x_{(k)}}{\xi_{(k)(j)}} r_{(k)xz} + w_{(k)(j)} \frac{y_{(j)} - y_{(k)}}{\xi_{(k)(j)}} r_{(k)yz} \right], \quad (28a)$$

$$t_{z(j)(k)}(u_{z(k)} - u_{z(j)}, \boldsymbol{x}_{(k)} - \boldsymbol{x}_{(j)}, t) = \mu \left[w_{(j)(k)} \frac{x_{(k)} - x_{(j)}}{\xi_{(k)(j)}} r_{(j)xz} + w_{(j)(k)} \frac{y_{(k)} - y_{(j)}}{\xi_{(k)(j)}} r_{(j)yz} \right]. \quad (28b)$$

Comparison of (28) and (19) leads to the determination of $A_{(k)(j)}$ and $B_{(k)(j)}$ as

$$A_{(k)(j)} = 2\mu \left[w_{(k)(j)} \frac{x_{(j)} - x_{(k)}}{\xi_{(k)(j)}} r_{(k)xz} + w_{(k)(j)} \frac{y_{(j)} - y_{(k)}}{\xi_{(k)(j)}} r_{(k)yz} \right], \quad (29a)$$

$$B_{(j)(k)} = 2\mu \left[w_{(j)(k)} \frac{x_{(j)} - x_{(k)}}{\xi_{(k)(j)}^2} r_{(j)xz} + w_{(j)(k)} \frac{y_{(j)} - y_{(k)}}{\xi_{(k)(j)}^2} r_{(j)yz} \right]. \quad (29b)$$

After substituting for the force densities, the final form of the equation of motion becomes

$$\rho_{(k)} \ddot{u}_{z(k)} = \mu \sum_{j=1}^{\infty} w_{(k)(j)} \left[(r_{(k)xz} + r_{(j)xz}) \frac{x_{(j)} - x_{(k)}}{\xi_{(k)(j)}} + (r_{(k)yz} + r_{(j)yz}) \frac{y_{(j)} - y_{(k)}}{\xi_{(k)(j)}} \right] V_{(j)} + b_{z(k)}, \quad (30a)$$

with

$$r_{(k)xz} = \frac{2}{\ell \pi \delta^3} \sum_{j=1}^{N} w_{(k)(j)} e_{(j)(k)} \cos \theta_{(k)(j)} V_{(j)}, \quad (30b)$$

$$r_{(k)yz} = \frac{2}{\ell \pi \delta^3} \sum_{j=1}^{N} w_{(k)(j)} e_{(j)(k)} \sin \theta_{(k)(j)} V_{(j)}. \quad (30c)$$

4. Bond-based peridynamics

In the case of pairwise interaction only between material points $\boldsymbol{x}_{(i)}$ and $\boldsymbol{x}_{(j)}$, the micropotential, $w_{(i)(j)}$, is a function of $e_{(i)(j)}$. Thus, the total potential energy can be obtained by the summation of the micropotentials $w_{(i)(j)}(e_{(i)(j)})$ arising from deformation only between two material points within the same family

$$U = \sum_{i=1}^{\infty} \left\{ \frac{1}{2} \sum_{j=1}^{\infty} \frac{1}{2} \left[w_{(i)(j)}(e_{(i)(j)}) + w_{(j)(i)}(e_{(j)(i)}) \right] V_{(j)} - (b_{z(i)} u_{z(i)}) \right\} V_{(i)}. \quad (31)$$

For a pairwise interaction, the Euler–Lagrange equation results in

$$\rho_{(k)} \ddot{u}_{z(k)} V_{(k)} + \left(\sum_{j=1}^{\infty} \frac{1}{2} \left(\frac{\partial w_{(k)(j)}}{\partial (u_{z(j)} - u_{z(k)})} \right) \frac{\partial (u_{z(j)} - u_{z(k)})}{\partial u_{z(k)}} \right.$$

$$\left. + \sum_{j=1}^{\infty} \frac{1}{2} \left(\frac{\partial w_{(j)(k)}}{\partial (u_{z(k)} - u_{z(j)})} \right) \frac{\partial (u_{z(k)} - w_{(j)})}{\partial u_{z(k)}} - b_{z(k)} \right) V_{(k)} = 0. \quad (32)$$

This equation can be rewritten as

$$\rho_{(k)}\ddot{u}_{z(k)} + \sum_{j=1}^{\infty} \tfrac{1}{2}[-f_{z(k)(j)} + f_{z(j)(k)}]V_{(j)} - b_{z(k)} = 0, \tag{33}$$

in which $f_{z(k)(j)}$ and $f_{z(j)(k)}$ are defined as

$$f_{z(k)(j)} = \frac{\partial w_{(k)(j)}}{\partial(u_{z(j)} - u_{z(k)})} \quad \text{and} \quad f_{z(j)(k)} = \frac{\partial w_{(j)(k)}}{\partial(u_{z(k)} - u_{z(j)})}. \tag{34}$$

They represent the PD interaction forces between the material points $\boldsymbol{x}_{(k)}$ and $\boldsymbol{x}_{(j)}$ arising from the deformation (elevation). For a linear material behavior, they can be defined in the form

$$f_{z(k)(j)} = cr_{(k)(j)} \quad \text{and} \quad f_{z(j)(k)} = cr_{(j)(k)} \tag{35}$$

or

$$f_{z(k)(j)} = cr_{(k)(j)} \quad \text{and} \quad f_{z(j)(k)} = -cr_{(k)(j)}. \tag{36}$$

With these definitions, the equation of motion, Equation (33), becomes

$$\rho\ddot{u}_{z(k)} = c \sum_{j=1}^{\infty} r_{(k)(j)}V_{(j)} + b_{z(k)} \tag{37a}$$

or

$$\rho\ddot{u}_{z(k)} = c \sum_{j=1}^{\infty} \frac{u_{z(j)} - u_{z(k)}}{\xi_{(k)(j)}} V_{(j)} + b_{z(k)}, \tag{37b}$$

in which c is the PD material parameter (bond constant) associated with the antiplane and torsional deformations.

As the horizon approaches zero, (37) must recover its classical counterpart, given as

$$\rho\ddot{u}_z = \mu(u_{z,xx} + u_{z,yy}). \tag{38}$$

Representing the out-of-plane displacement at material point $\boldsymbol{x}_{(j)}$ by using a Taylor series expansion as in (24), substituting it into (37) along with the infinitesimal volume, and performing algebraic manipulations after converting the summations to integrations lead to

$$\rho\ddot{u}_{z(k)} = c\frac{\pi\ell\delta^3}{6}(u_{z(k),xx} + u_{z(k),yy}). \tag{39}$$

Comparison of the bond-based PD equation of motion with its classical counterpart leads to the determination of the PD bond constant, c, as

$$c = \frac{6\mu}{\pi\ell\delta^3}, \tag{40}$$

which is dependent on the horizon. The final form of the bond-based PD equation of motion becomes

$$\rho\ddot{u}_{z(k)} = \frac{6\mu}{\pi\ell\delta^3} \sum_{j=1}^{\infty} \frac{u_{z(j)} - u_{z(k)}}{\xi_{(k)(j)}} V_{(j)}. \tag{41}$$

Alternatively, in light of (34) and (35), the bond constant can also be determined by considering the explicit expression for the micropotentials in the form

$$w_{(k)(j)} = \tfrac{1}{2}c\xi_{(k)(j)}r_{(k)(j)}^2 \quad \text{and} \quad w_{(j)(k)} = \tfrac{1}{2}c\xi_{(k)(j)}r_{(j)(k)}^2. \tag{42}$$

Therefore, the strain energy density at material point $x_{(k)}$ can be obtained from (7) as

$$W_{(k)} = c\frac{1}{2}\sum_{j=1}^{\infty}\frac{1}{2}\xi_{(k)(j)}r_{(k)(j)}^2 V_{(j)}. \tag{43}$$

Substituting for the slope and infinitesimal volume and converting the summation to integration lead to

$$W_{(k)} = \ell c\frac{1}{2}\int_0^\delta \int_0^{2\pi} \frac{1}{2}(u_{z(j)} - u_{z(k)})^2\, d\xi\, d\theta. \tag{44}$$

The peridynamic bond constant, c, can be determined by equating the strain energies from classical continuum mechanics and peridynamics for a specified simple deformation such as $w(x, y) = (x + y)$. For the material point of interest located at $(x_{(k)} = 0, y_{(k)} = 0)$, the elevation is $e_{(k)(j)} = (x' + y')$ and $\xi = \xi_{(k)(j)} = \sqrt{x'^2 + y'^2}$. Thus, the peridynamic strain energy density can be obtained as

$$W_{(k)} = \ell c\frac{1}{2}\int_0^\delta \int_0^{2\pi} \frac{1}{2}(u_{z(j)} - u_{z(k)})^2\, d\xi\, d\theta = \ell c\frac{1}{2}\int_0^\delta \int_0^{2\pi} \frac{1}{2}\xi^2\, d\xi\, d\theta = \frac{\ell c\pi\delta^3}{6}. \tag{45}$$

The corresponding strain energy density based on classical continuum mechanics can be written as

$$W = \tfrac{1}{2}(\sigma_{xz}\gamma_{xz} + \sigma_{yz}\gamma_{yz}) = \tfrac{1}{2}\mu(u_{z,x}^2 + u_{z,y}^2) = \mu. \tag{46}$$

Equating the strain energies from peridynamics and the classical continuum mechanics leads to the determination of the PD material parameter, $c = 6\mu/\pi\ell\delta^3$, which is the same as in (40).

5. Correction of PD material parameters

The PD material parameters b and c are determined for material points with a horizon completely embedded in the material. The values of these parameters depend on the domain of integration defined by the horizon. Therefore, their values require correction if the material point is close to free surfaces or material interfaces (Figure 4). Since the presence of free surfaces is problem-dependent, it is impractical to resolve this issue analytically.

5.1. *Surface correction.* The bond-based and ordinary state-based PD parameters are corrected by comparing the PD and classical expressions for the strain energy density and shear strain components for two different simple loading conditions. The correction for the parameter c is achieved by comparing the strain energy densities, and for the parameter b by comparing the shear strain components.

The first loading case is a simple linear displacement distribution in the x-direction given by

$$u_z = \zeta x. \tag{47}$$

The second loading case is a simple linear displacement distribution in the y-direction given by

$$u_z = \zeta y. \tag{48}$$
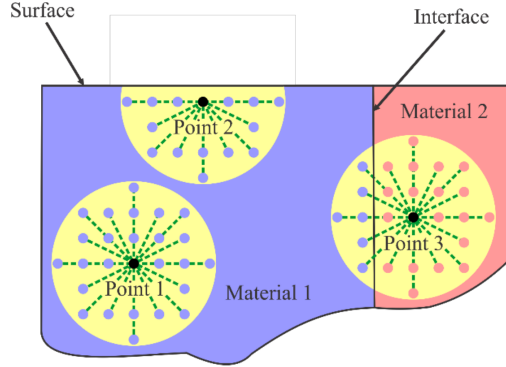
Figure 4. Surface effects in the domain of interest.

Due to these loading conditions, the corresponding PD strain energy density and shear strain can be obtained from (43) and (23) as

$$W_{(k)x}^{\text{PD}} = \zeta^2 c \frac{1}{2} \sum_{j=1}^{N} \frac{1}{2} \frac{1}{\xi_{(k)(j)}} (x_{(j)} - x_{(k)})^2 V_{(j)}, \quad W_{(k)y}^{\text{PD}} = \zeta^2 c \frac{1}{2} \sum_{j=1}^{N} \frac{1}{2} \frac{1}{\xi_{(k)(j)}} (y_{(j)} - y_{(k)})^2 V_{(j)} \quad (49)$$

and

$$r_{(k)xz} = \zeta b \sum_{j=1}^{N} w_{(k)(j)} (x_{(j)} - x_{(k)}) \cos \theta_{(k)(j)} V_{(j)}, \quad r_{(k)yz} = b\zeta \sum_{j=1}^{N} w_{(k)(j)} (y_{(j)} - y_{(k)}) \sin \theta_{(k)(j)} V_{(j)}, \quad (50)$$

with N representing the number of material points inside the horizon of $\boldsymbol{x}_{(k)}$. For these loading conditions, the classical strain energy of a material point $W_{(k)}^{\text{CCM}}$ and shear strain components are

$$W_{(k)x}^{\text{CCM}} = \tfrac{1}{2}\mu\zeta^2 \quad \text{and} \quad W_{(k)y}^{\text{CCM}} = \tfrac{1}{2}\mu\zeta^2 \quad (51)$$

and

$$\gamma_{(k)xz} = \zeta \quad \text{and} \quad \gamma_{(k)yz} = \zeta. \quad (52)$$

The correction factors for these loading conditions at material point $\boldsymbol{x}_{(k)}$ can be determined as

$$g_{x(k)} = \frac{W_{(k)x}^{\text{CCM}}}{W_{(k)x}^{\text{PD}}} \quad \text{and} \quad g_{(k)xz} = \frac{\gamma_{(k)xz}}{r_{(k)xz}} \quad (53)$$

and

$$g_{y(k)} = \frac{W_{(k)y}^{\text{CCM}}}{W_{(k)y}^{\text{PD}}} \quad \text{and} \quad g_{(k)yz} = \frac{\gamma_{(k)yz}}{r_{(k)yz}}. \quad (54)$$

With these correction factors, the final form of the ordinary state-based PD equation become

$$\rho_{(k)} \ddot{u}_{z(k)} = \mu \sum_{j=1}^{\infty} w_{(k)(j)} \left[(r_{(k)xz} g_{(k)xz} + r_{(j)xz} g_{(j)xz}) \frac{x_{(j)} - x_{(k)}}{\xi_{(k)(j)}} \right.$$
$$\left. + (r_{(k)yz} g_{(k)yz} + r_{(j)yz} g_{(j)yz}) \frac{y_{(j)} - y_{(k)}}{\xi_{(k)(j)}} \right] V_{(j)} + b_{z(k)}, \quad (55)$$

in which

$$r_{(k)xz} = b \sum_{j=1}^{N} w_{(k)(j)} e_{(j)(k)} g_{(k)xz} \cos\theta_{(k)(j)} V_{(j)}, \quad r_{(k)yz} = b \sum_{j=1}^{N} w_{(k)(j)} e_{(j)(k)} g_{(k)yz} \sin\theta_{(k)(j)} V_{(j)}. \quad (56)$$

For the bond-based parameter, the correction factors can be obtained by taking their mean value as

$$\bar{g}_{(k)(j)x} = \frac{g_{x(k)} + g_{x(j)}}{2} \quad \text{and} \quad \bar{g}_{(k)(j)y} = \frac{g_{y(k)} + g_{y(j)}}{2}, \quad (57)$$

which may represent the principal axis of an ellipsoid. As introduced by Kilic [2008], the correction factor between arbitrary material points $x_{(k)}$ and $x_{(j)}$ can be calculated by

$$G_{(k)(j)} = \left[(n_x/\bar{g}_{(k)(j)x})^2 + (n_y/\bar{g}_{(k)(j)y})^2 \right]^{-1/2}, \quad (58)$$

where n_x and n_y are direction cosines of $\boldsymbol{n} = (\boldsymbol{x}_{(j)} - \boldsymbol{x}_{(k)})/|\boldsymbol{x}_{(j)} - \boldsymbol{x}_{(k)}|$. The final form of the bond-based PD equation including the correction factor for material point $\boldsymbol{x}_{(k)}$ becomes

$$\rho \ddot{u}_{z(k)} = \frac{6\mu}{\pi \ell \delta^3} \sum_{j=1}^{\infty} G_{(k)(j)} \frac{u_{z(j)} - u_{z(k)}}{\xi_{(k)(j)}} V_{(j)}. \quad (59)$$

5.2. *Dissimilar material interface.* The correction at the interface is achieved by using equivalent PD material parameters [Oterkus et al. 2014]. As shown in Figure 5, the material point $\boldsymbol{x}_{(i)}$ may interact with material points $\boldsymbol{x}_{(j)}$ and $\boldsymbol{x}_{(m)}$. Material points $\boldsymbol{x}_{(i)}$ and $\boldsymbol{x}_{(j)}$ are embedded in material 1, and $\boldsymbol{x}_{(m)}$ is embedded in material 2. The PD material parameter between points $\boldsymbol{x}_{(i)}$ and $\boldsymbol{x}_{(j)}$ is $a_{(i)(j)}$, and it differs from $a_{(i)(m)}$ between material points $\boldsymbol{x}_{(i)}$ and $\boldsymbol{x}_{(m)}$. Because the material points $\boldsymbol{x}_{(i)}$ and $\boldsymbol{x}_{(m)}$ are embedded in two different materials, their material parameter, $a_{(i)(m)}$, can be expressed in terms of an equivalent material constant as

$$a_{(i)(m)} = \frac{\ell_1 + \ell_2}{\ell_1/a_1 + \ell_2/a_2}, \quad (60)$$

in which ℓ_1 represents the segment of the distance between material points $\boldsymbol{x}_{(i)}$ and $\boldsymbol{x}_{(m)}$ in material 1, whose material parameter is a_1, and ℓ_2 represents the segment in material 2, whose material parameter is a_2.

6. Boundary conditions

Unlike the local theory, the PD boundary conditions are imposed through a nonzero volume of fictitious boundary layers. This necessity arises because the PD field equations do not contain any spatial derivatives; therefore, constraint conditions are, in general, not necessary for the solution of an integro-differential equation of motion. However, such conditions can be imposed by prescribing constraints on the displacement or transverse shear stress components in a fictitious boundary layer.

6.1. *Displacement constraints.* This type of boundary condition can be achieved through a fictitious region, $\mathcal{R}_f$. Therefore, a fictitious boundary layer with depth δ is introduced along the boundary of the actual material region, $\mathcal{R}$, as shown in Figure 6. Based on numerical experiments, Macek and Silling
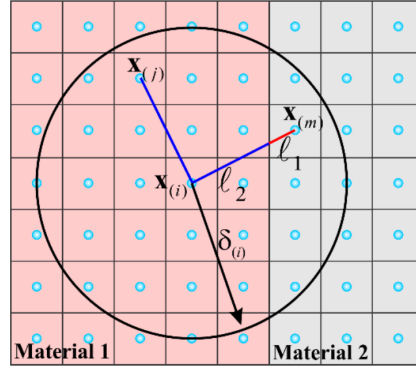
Figure 5. Interaction of material points across the interface.
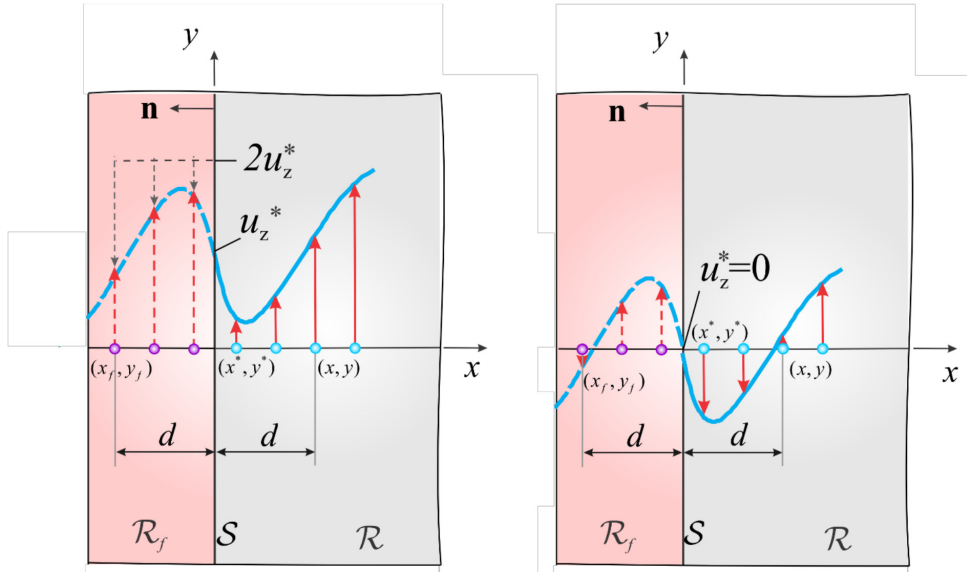

Figure 6. Imposing displacement constraints on the boundary: (left) nonzero constraint $u_z(x^*, y^*, t) = u_z^*$, and (right) zero constraint $u_z(x^*, y^*, t) = u_z^* = 0$.

[2007] suggest that the extent of the fictitious boundary layer be equal to the horizon, δ, in order to ensure that the imposed prescribed constraints are accurately reflected in the real domain.

The prescribed boundary value, $u_z^*(x^*, y^*, t)$, is imposed through a layer of the fictitious region, $\mathcal{R}_f$, along the boundary of the material surface, $\mathcal{S}$, as

$$u_z(x_f, y_f, t + \Delta t) = 2u_z^*(x^*, y^*, t + \Delta t) - u_z(x, y, t) \tag{61a}$$

with

$$(x^*, y^*) \in \mathcal{S}, \quad (x_f, y_f) \in \mathcal{R}_f, \quad (x, y) \in \mathcal{R}, \tag{61b}$$

in which (x, y) represents the position of a material point in $\mathcal{R}$, and (x^*, y^*) represents the location of a point on the boundary surface, $\mathcal{S}$. The location of the image material point in $\mathcal{R}_f$ is denoted by (x_f, y_f). The implementation of the prescribed boundary value of the displacement is depicted in Figure 6. In the case of $u_z^*(x^*, y^*, t) = 0$, this condition becomes

$$u_z(x_f, y_f, t + \Delta t) = -u_z(x, y, t). \tag{62}$$

6.2. Conditions on transverse shear stress components. Similar to the displacement boundary conditions, the transverse shear stress conditions are imposed through a fictitious region, $\mathcal{R}_f$. In the case of antiplane shear deformation, applied transverse shear stress on the boundary, $\sigma_{\alpha z}(x^*, y^*, t) = \tau_\alpha$ with $\alpha = x, y$, is imposed as (Figure 7, left)

$$\sigma_{\alpha z}(x^*, y^*, t) = \mu\left[\frac{\partial u_z}{\partial \alpha}(x^*, y^*)\right] = \tau_\alpha \tag{63a}$$

or

$$\frac{\partial u_z}{\partial \alpha}(x^*, y^*) = \frac{\tau_\alpha}{\mu}, \tag{63b}$$

which can be enforced as

$$u_z(x_f, y_f) = \frac{1}{\mu}\tau_\alpha(\alpha_f - \alpha) + u_z(x, y). \tag{63c}$$

For a zero transverse shear stress condition, i.e., $\sigma_{\alpha z}(x^*, y^*, t) = 0$, this expression reduces to

$$u_z(x^*, y^*) = u_z(x, y). \tag{64}$$

In the case of torsional deformation, zero shear stress boundary conditions are imposed as

$$\sigma_{xz}(x^*, y^*, t) = \mu\left[\frac{\partial u_z}{\partial x}(x^*, y^*) - \psi(y - y_0)\right] = 0, \tag{65a}$$

$$\sigma_{yz}(x^*, y^*, t) = \mu\left[\frac{\partial u_z}{\partial y}(x^*, y^*) - \psi(x - x_0)\right] = 0 \tag{65b}$$

or

$$\frac{\partial u_z}{\partial x}(x^*, y^*) = \frac{1}{\mu}\psi(y - y_0), \tag{66a}$$

$$\frac{\partial u_z}{\partial y}(x^*, y^*) = \frac{1}{\mu}\psi(x - x_0), \tag{66b}$$

which can be imposed as

$$u_z(x_f, y_f) = \frac{1}{\mu}\psi(y - y_0)(x_f - x) + u_z(x, y), \tag{67a}$$

$$u_z(x_f, y_f) = \frac{1}{\mu}\psi(x - x_0)(y_f - y) + u_z(x, y), \tag{67b}$$

in which ψ represents the applied angle of twist and (x_0, y_0) denote the coordinates of the reference point.
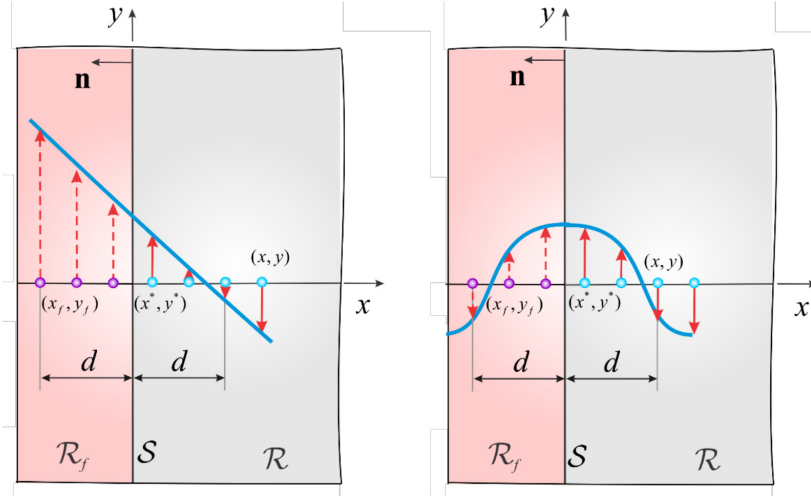
Figure 7. Material points and their image in the fictitious region for imposing (left) nonzero flux, and (right) zero flux.

7. Failure prediction

Damage is introduced through elimination of interactions (micropotentials) among the material points. It is assumed that when the change in angle (transverse shear strain), $r_{(k)(j)}$, between two material points, k and j, exceeds its critical value, r_c, the onset of damage occurs. Damage is reflected in the equations of motion by removing the force density vectors between the material points in an irreversible manner. Therefore, the force density vectors $t_{z(k)(j)}$ and $t_{z(j)(k)}$ in the case of the ordinary state-based form of the equations of motion and $f_{z(k)(j)}$ and $f_{z(j)(k)}$ in the case of the bond-based form can be modified through a history-dependent scalar-valued function $H(t, x_{(j)} - x_{(k)})$ [Silling and Askari 2005] as

$$t_{z(k)(j)} = H(t, x_{(j)} - x_{(k)})t_{z(k)(j)} \quad \text{and} \quad t_{z(j)(k)} = H(t, x_{(k)} - x_{(j)})t_{z(j)(k)} \tag{68}$$

and

$$f_{z(k)(j)} = H(t, x_{(j)} - x_{(k)})f_{z(k)(j)} \quad \text{and} \quad f_{z(j)(k)} = H(t, x_{(k)} - x_{(j)})f_{z(j)(k)} \tag{69}$$

in which a history-dependent scalar-valued function H is defined as

$$H(t, x_{(j)} - x_{(k)}) = \begin{cases} 1 & \text{if } r_{(k)(j)}(t', x_{(j)} - x_{(k)}) < r_c \text{ for all } 0 \le t' \le t, \\ 0 & \text{otherwise.} \end{cases} \tag{70}$$

The critical value, r_c, can be determined by equating the amount of energy required to remove all of the micropotentials across a unit crack surface to the critical energy release rate, G_{IIIC}, for the mode III type of loading of linear elastic fracture mechanics (LEFM). In order to create a new crack surface, A, all of the micropotentials (interactions) between the material points $x_{(k+)}$ and $x_{(j-)}$ whose line of action crosses this new surface must be terminated, as sketched in Figure 8. The material points $x_{(k+)}$ and $x_{(j-)}$ are located above and below the new crack surface, respectively.
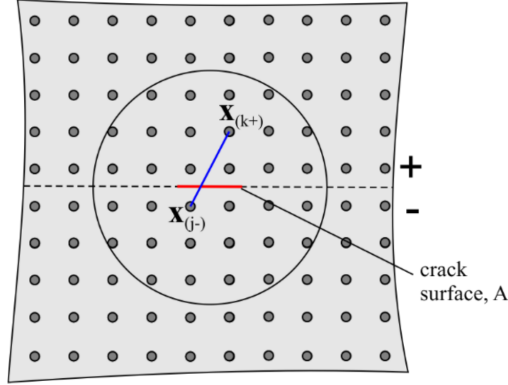
Figure 8. Interaction of the material points $x_{(k+)}$ and $x_{(j-)}$ above and below the crack surface.

Hence, the strain energy required to remove the interaction between two material points $x_{(k+)}$ and $x_{(j-)}$ can be expressed as

$$W^c_{(k+)(j-)} = \frac{1}{2} \frac{w^c_{(k+)(j-)} + w^c_{(j-)(k+)}}{2} V_{(k+)} V_{(j-)}. \tag{71}$$

Furthermore, the total strain energy required to remove all of the interactions across the newly created crack surface A can be obtained as

$$W^c = \frac{1}{2} \sum_{k=1}^{K^+} \frac{1}{2} \sum_{j=1}^{J^-} w^c_{(k+)(j-)} V_{(k+)} V_{(j-)} + \frac{1}{2} \sum_{k=1}^{K^+} \frac{1}{2} \sum_{j=1}^{J^-} w^c_{(j-)(k+)} V_{(j-)} V_{(k+)}, \tag{72}$$

for which the line of interaction defined by $\xi_{(k+)(j-)} = |x_{(k+)} - x_{(j-)}|$ and the crack surface intersect, and K^+ and J^- indicate the number of material points above and below the crack surface within the families of $x_{(k+)}$ and $x_{(j-)}$, respectively. If this line of interaction and crack surface intersect at the crack tip, only half of the critical micropotential is considered in the summation.

Considering only the pairwise interactions between $x_{(k+)}$ and $x_{(j-)}$ crossing the crack surface, the micropotentials for linear elastic deformation are given by (42) as

$$w_{(k+)(j-)} = \tfrac{1}{2} c \xi_{(k+)(j-)} r^2_{(k+)(j-)} \quad \text{and} \quad w_{(j-)(k+)} = \tfrac{1}{2} c \xi_{(j-)(k+)} r^2_{(j-)(k+)}. \tag{73}$$

Their critical values can be expressed as

$$w^{\text{cr}}_{(k+)(j-)} = \tfrac{1}{2} c \xi_{(k+)(j-)} r^2_c \quad \text{and} \quad w^{\text{cr}}_{(j-)(k+)} = \tfrac{1}{2} c \xi_{(j-)(k+)} r^2_c. \tag{74}$$

Thus, the total strain energy required to remove all of the interactions across the newly created crack surface A becomes

$$W^c = \tfrac{1}{2} c r^2_c \sum_{k=1}^{K^+} \sum_{j=1}^{J^-} \xi_{(j-)(k+)} V_{(k+)} V_{(j-)}. \tag{75}$$

The amount of energy required to remove all of the interactions (micropotentials) across the unit crack surface equals the critical strain energy release rate, thus leading to

$$G_{\text{IIIc}} = \frac{W^c}{A} = \frac{\frac{1}{2} c r_c^2 \sum_{k=1}^{K^+} \sum_{j=1}^{J^-} \xi_{(j^-)(k^+)} V_{(k^+)} V_{(j^-)}}{A}. \tag{76}$$

As given by Madenci and Oterkus [2014], the summation in (76) can be evaluated as

$$\frac{\sum_{k=1}^{K^+} \sum_{j=1}^{J^-} \xi_{(j^-)(k^+)} V_{(k^+)} V_{(j^-)}}{A} = \frac{h \delta^4}{2}. \tag{77}$$

Thus, the critical shear angle can be obtained as

$$r_c = \sqrt{\frac{2\pi G_{\text{IIIc}}}{3\mu\delta}}. \tag{78}$$

The local damage at a point is defined as the weighted ratio of the number of eliminated interactions to the total number of initial interactions of a material point with its family members [Silling and Askari 2005]:

$$\phi(x_{(k)}, t) = 1 - \frac{\sum_{j=1}^{N} H(t, x_{(j)} - x_{(k)}) V_{(j)}}{\sum_{j=1}^{N} V_{(j)}}. \tag{79}$$

If the local damage value has a value equal to or larger than 0.5, it can be interpreted as the creation of new crack surfaces.

8. Numerical results

The solution to the PD field equations requires time and spatial integrations while considering constraints and/or loading conditions, as well as initial conditions. The spatial integration is performed by using a Gaussian integration (meshless) scheme because of its simplicity, and time integration by using backward and forward difference explicit integration schemes. The horizon size is commonly defined as three times the spacing between the material points. This ratio is established based on numerical experimentation and the spacing between the material points is based on a convergence study. The domain is divided into a uniform grid, with integration or collocation (material) points associated with specific volumes. Associated with a particular material point, the numerical implementation of spatial integration involves the summation of the volumes of material points within its horizon. However, the volume of each material point may not be embedded in the horizon in its entirety, i.e., the material points located near the surface of the horizon may have truncated volumes. As a result, the volume integration over the horizon may be incorrect if the entire volume of each material point is included in the numerical implementation. Therefore, a volume correction factor is necessary to correct for the extra volume, as explained by Madenci and Oterkus [2014]. The steady-state solution to the PD field equation can be achieved by different techniques; however, in this study, an adaptive dynamic relaxation method (ADR) is employed (described in detail by Madenci and Oterkus [2014]).

The capability of the PD theory is demonstrated by considering (1) a square bar under antiplane shear loading, (2) a bimaterial rectangular bar under antiplane shear loading, (3) a square bar with a crack under
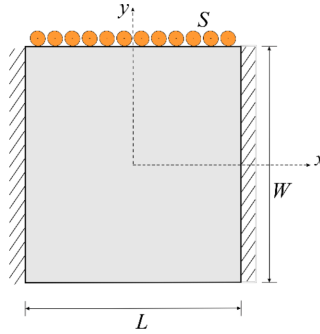
Figure 9. Square bar under antiplane shear loading.

antiplane shear loading, (4) a rectangular bar under torsion, and (5) a rectangular bar with a preexisting crack under torsion. If an analytical solution is not available, a comparison is performed against finite element analysis (FEA) by using ANSYS, a commercially available program, in order to establish the validity of the predictions. During the construction of the solutions to all these problems, uniform spacing, $\Delta x = \Delta y$, between the material points is employed, and the horizon is specified as $\delta = 3.015\Delta x$. Also, the steady-state solutions are achieved by using ADR with a time integration interval of $\Delta t = 1$ s.

8.1. *Square bar under antiplane shear loading.* As illustrated in Figure 9, a square bar with $L = W = 1$ in is clamped along its left and right surfaces while subjected to a uniform transverse shear stress of $S = 12000$ psi on its top surface. The bottom surface is free of loading. These boundary conditions are imposed as

$$u_z\left(x = \pm\tfrac{1}{2}L, y\right) = 0, \quad \mu\frac{\partial u_z}{\partial y}\left(x, y = -\tfrac{1}{2}W\right) = 0, \quad \mu\frac{\partial u_z}{\partial y}\left(x, y = \tfrac{1}{2}W\right) = S. \tag{80}$$

The shear modulus is specified as $\mu = 12 \times 10^6$ psi. The cross-section is discretized with a uniform grid spacing of $\Delta x = \Delta y = 0.01$ in, resulting in 100 material points in each of the x- and the y-directions. The bond-based and ordinary state-based PD displacement predictions and their comparison with the FEA results are shown in Figure 10. The PD theory successfully captures the antiplane shear deformation, and this comparison confirms the validity of the implementation for displacement- and stress-type boundary conditions.

8.2. *Bimaterial rectangular bar under antiplane shear loading.* As shown in Figure 11, a bimaterial rectangular bar with $L = 0.2$ in and $W = 1$ in is clamped along its bottom surface and subjected to a uniform transverse shear stress of $S = 12000$ psi on its top surface. The bottom surface is free of any loading. These boundary conditions are imposed as

$$u_z\left(x, y = -\tfrac{1}{2}W\right) = 0, \quad \mu\frac{\partial u_z}{\partial x}\left(x = \pm\tfrac{1}{2}L, y\right) = 0, \quad \mu\frac{\partial u_z}{\partial y}\left(x, y = \tfrac{1}{2}W\right) = S. \tag{81}$$

The shear moduli of the materials are specified as $\mu_1 = 12 \times 10^6$ psi and $\mu_2 = 6 \times 10^6$ psi. The cross-section is discretized with a uniform grid spacing of $\Delta x = \Delta y = 0.01$ in, resulting in 20 and 100 material points in the x- and in the y-directions, respectively.
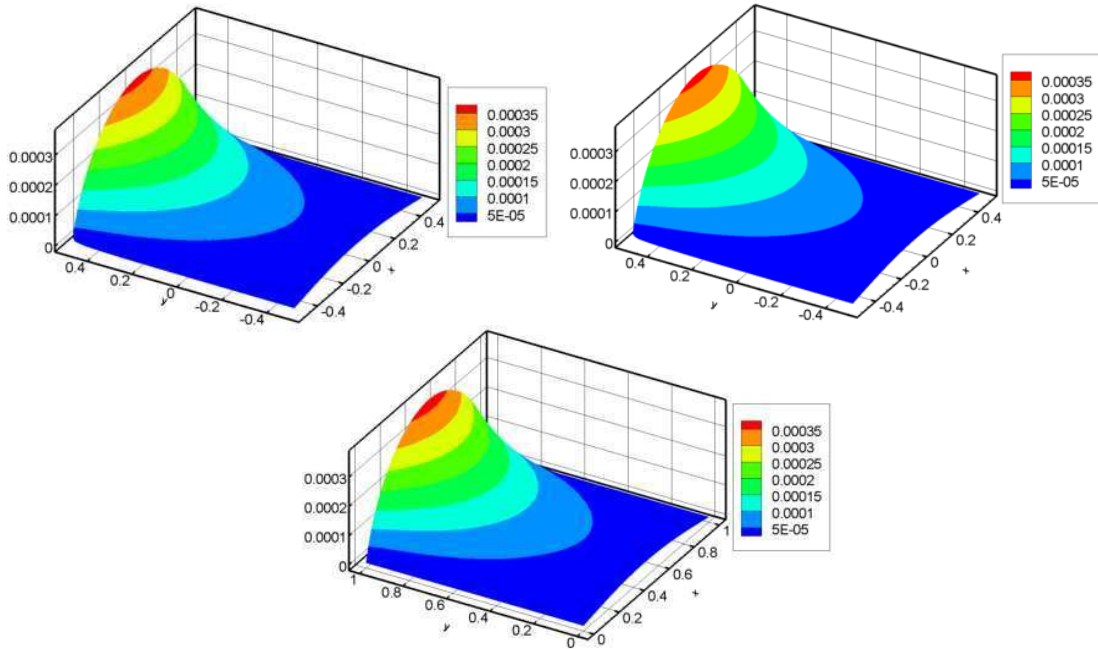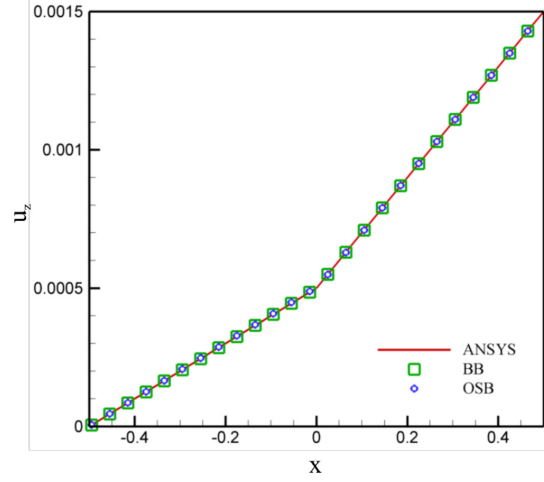
Figure 10. Displacement variation across the bar: (top left) ordinary state-based PD
solution, (top right) bond-based PD solution, and (bottom) FEA solution.
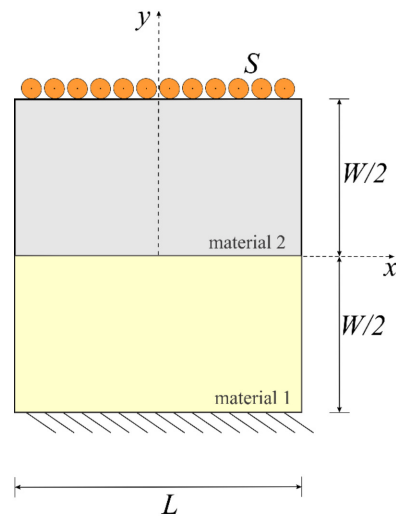
Figure 11. Square bar under antiplane shear loading.

Along the vertical axis, the bond-based and ordinary state-based PD displacement variations and their
comparison with the FEA results are shown in Figure 12. The results demonstrate the validity of the PD
modeling of interface conditions. The predictions are in excellent agreement and capture the effect of
dissimilar materials.

Figure 12. Displacement variation along the vertical axis.

8.3. *Square bar with a crack under antiplane shear loading.* As illustrated in Figure 13, a square bar with $L = W = 1$ in with a preexisting central crack of length $a = 0.2$ in is subjected to a uniform transverse shear stress of $S = 12000$ psi on its top and bottom surfaces. It is free of any loading and constraints on its other surfaces. These boundary conditions are imposed as

$$\mu \frac{\partial u_z}{\partial x}\left(x = \pm \tfrac{1}{2}L, y\right) = 0, \quad \mu \frac{\partial u_z}{\partial y}\left(x, y = \tfrac{1}{2}W\right) = S, \quad \mu \frac{\partial u_z}{\partial y}\left(x, y = -\tfrac{1}{2}W\right) = -S. \tag{82}$$

The shear modulus is specified as $\mu = 12 \times 10^6$ psi. The critical angle value is specified as $r_{\mathrm{cr}} = 0.0035$. The cross-section is discretized with a uniform grid spacing of $\Delta x = \Delta y = 0.01$ in, resulting in 100 material points in both the x- and in the y-directions. As expected, a self-similar crack growth, shown in Figure 14 (left), is observed. Also, the crack surfaces exhibit a tearing type of deformation, as shown in Figure 14 (right).

8.4. *Rectangular bar under torsion.* As illustrated in Figure 15, a rectangular bar with $L = 1$ in and $W = 2$ in is subjected to a unit angle of twist, $\theta = 1$ in/in. All surfaces of the bar are free of loading. These boundary conditions are

$$\tau_{xz}\left(x = \pm \tfrac{1}{2}L, y\right) = \mu \left[\frac{\partial u_z}{\partial x}\left(x = \pm \tfrac{1}{2}L, y\right) - \theta(y - y_0) \right] = 0 \tag{83}$$

and

$$\tau_{yz}\left(x, y = \pm \tfrac{1}{2}W\right) = \mu \left[\frac{\partial u_z}{\partial y}\left(x, y = \pm \tfrac{1}{2}W\right) + \theta(x - x_0) \right] = 0. \tag{84}$$

They can be rewritten as

$$\frac{\partial u_z}{\partial x}\left(x = \pm \tfrac{1}{2}L, y\right) = \frac{\theta(y - y_0)}{\mu} \tag{85}$$

and

$$\frac{\partial u_z}{\partial y}\left(x, y = \pm \tfrac{1}{2}W\right) = -\frac{\theta(x - x_0)}{\mu}, \tag{86}$$
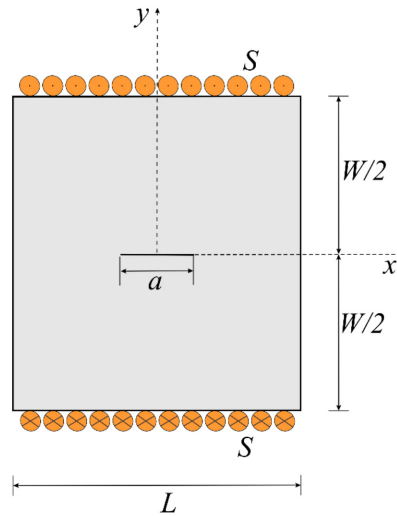
**Figure 13.** Square bar with a crack under antiplane shear loading.
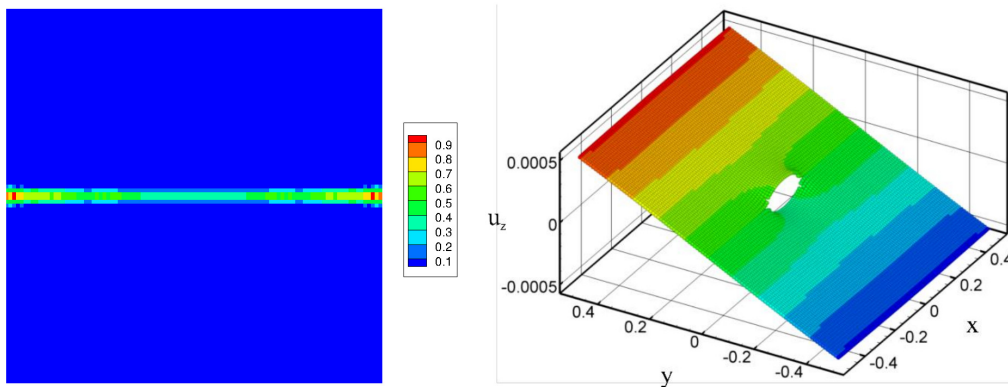
Figure 14. Square bar with a crack under antiplane shear loading: (left) crack growth path (damage distribution), and (right) crack opening mode.

in which x_0 and y_0 represent the coordinates of the reference point on the boundary and are specified as $(0, 0)$. The cross-section is discretized with a uniform grid spacing of $\Delta x = \Delta y = 0.02$ in, resulting in 50 and 100 material points in the x- and in the y-directions, respectively.

The bond-based and ordinary state-based PD warpage predictions and their comparison with the FEA results are shown in Figure 16. Comparisons of the stress predictions are shown in Figures 17 and 18. As shown in these figures, the agreement is remarkable, and the traction-free boundary conditions are enforced through fictitious regions. The PD results capture the expected warping behavior.

8.5. *Rectangular bar with a preexisting crack under torsion.* The rectangular bar has a preexisting edge crack length of a, as shown in Figure 19. The crack length is varied from 0 to b, as investigated by Armero [2012]. The external boundary conditions and loading are the same as those of the previous
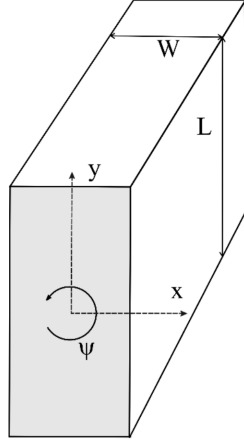
Figure 15. Rectangular bar under torsion.
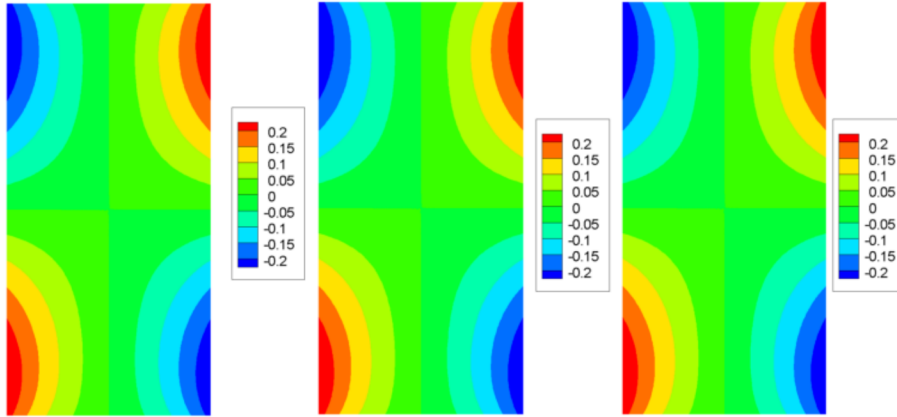
Figure 16. Displacement variation: (left) bond-based solution, (middle) ordinary state-based solution, and (right) exact solution.

problem. The traction-free conditions on the crack surfaces are also imposed explicitly as

$$\tau_{yz}(x, y = \pm 0) = \mu \left[\frac{\partial u_z}{\partial y}(x, y = \pm 0) + \theta(x - x_0) \right] = 0 \tag{87}$$

or

$$\frac{\partial u_z}{\partial y}(x, y = \pm 0) = -\frac{\theta(x - x_0)}{\mu}. \tag{88}$$

The cross-section is discretized with a uniform grid spacing of $\Delta x = \Delta y = 0.005$ in, resulting in 200 and 400 material points in the x- and in the y-directions, respectively.

The bond-based and ordinary state-based PD predictions for the shear stress norm for varying crack lengths are shown in Figures 20 and 21, respectively. These predictions are in remarkable agreement with the results of Armero [2012], who employs finite elements with embedded discontinuities. Figure 22
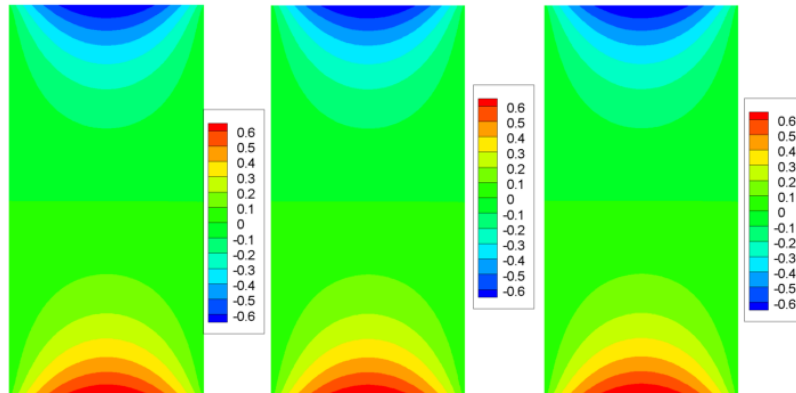
Figure 17. Shear stress, τ_{xz}, variation: (left) bond-based solution, (middle) ordinary state-based solution, and (right) exact solution.
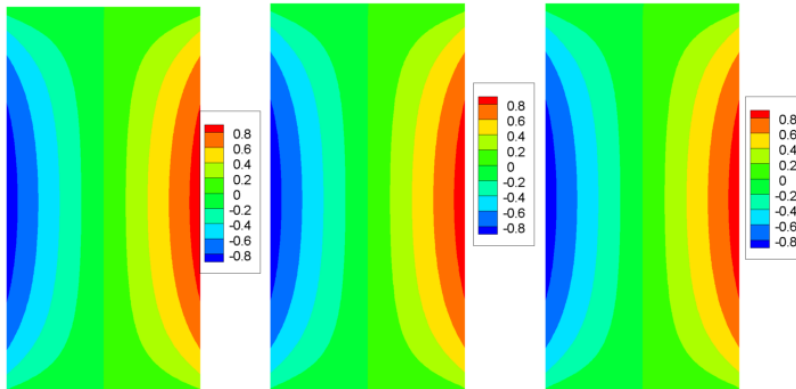
Figure 18. Shear stress, τ_{yz}, variation: (left) bond-based solution, (middle) ordinary state-based solution, and (right) exact solution.
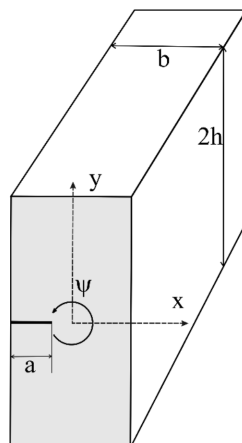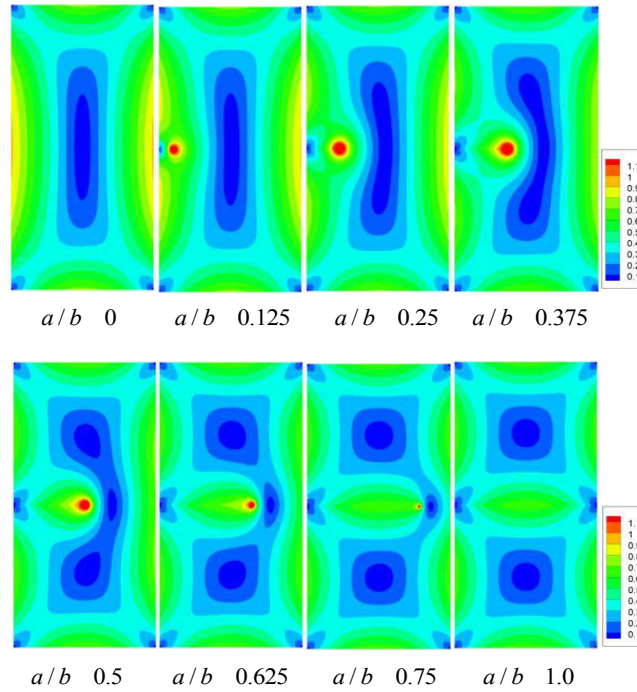

Figure 19. Rectangular bar with a preexisting crack under torsion.
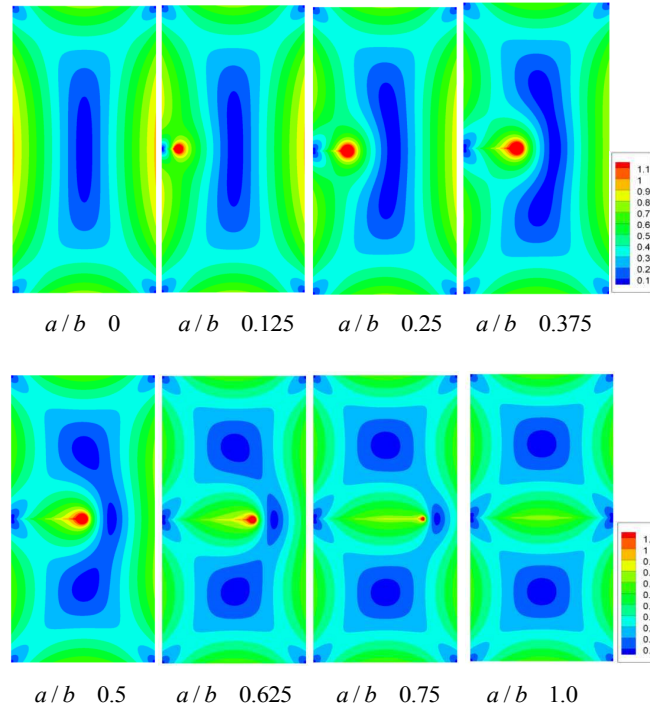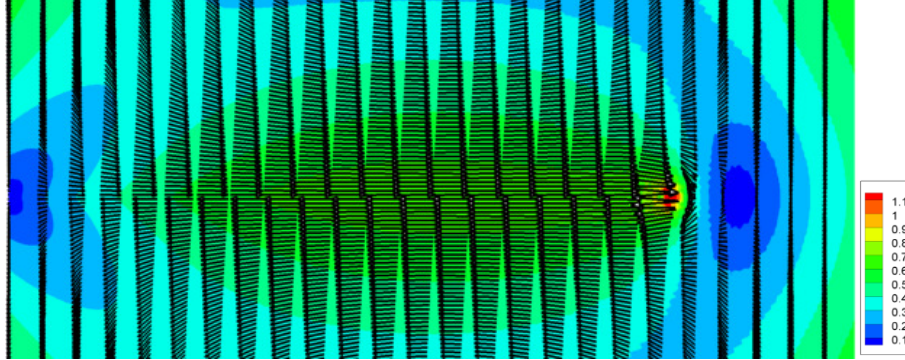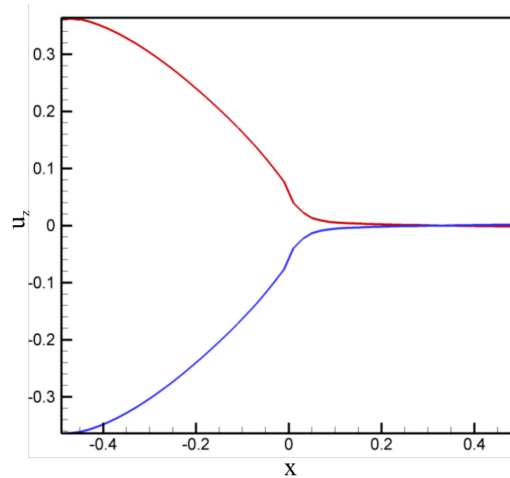
Figure 20. Bond-based PD predictions for stress norm $\tau = \sqrt{\tau_{xz}^2 + \tau_{yz}^2}$.

Figure 21. Ordinary state-based PD predictions for stress norm $\tau = \sqrt{\tau_{xz}^2 + \tau_{yz}^2}$.

Figure 22. Ordinary state-based PD predictions for stress vector $\boldsymbol{\tau} = \{\tau_{xz}, \tau_{yz}\}$ close to the crack surface for $a/b = 0.75$.

Figure 23. Crack tip opening profile at the crack surface for $a/b = 0.5$.

presents the variation of stress vectors near the crack. As expected, the results show that the stress vectors are aligned with the crack ($\tau_{yz} = 0$). Also, the crack opening displacement is shown in Figure 23. The PD analysis predicts a cusp-like crack opening displacement near the crack tip. It is similar to that obtained by Silling [2000].

9. Final remarks

The classical equilibrium equations for antiplane shear and torsional deformations present only one engineering constant; i.e., shear modulus. Therefore, bond-based peridynamics does not suffer from the loss of an independent engineering constant as in the case of in-plane deformation with a constraint on the Poisson's ratio being $\frac{1}{3}$. If the degree of nonlocality is insignificant, then both the ordinary state-based and bond-based peridynamics lead to the same predictions. However, if the degree of interaction among the material points needs to be specified, then the ordinary state-based peridynamics may be better

suited, such as in the case of a porous medium with fluid pressure. This study describes the determination of the PD material parameters for both formulations, as well as their correction near the free surfaces and interface of dissimilar materials. Inherent with the nonlocal formulations, the imposition of the boundary conditions requires volume constraints. This study also describes the implementation of the essential and natural boundary conditions. The validity of the equations of motion for both ordinary state-based and bond-based peridynamics, the surface correction procedure, and implementation of the boundary conditions are established by considering benchmark problems with complex geometry and boundary conditions. Comparison of the PD predictions with the FEA results proves the fidelity of the peridynamics, which offers its distinct advantage for predicting damage paths.

References

[Agwai et al. 2011] A. Agwai, I. Guven, and E. Madenci, "Predicting crack propagation with peridynamics: A comparative study", *Int. J. Fract.* **171**:1 (2011), 65–78.

[Armero 2012] F. Armero, "Strong discontinuities in antiplane/torsional problems of computational failure mechanics", *Int. J. Fract.* **178**:1–2 (2012), 3–32.

[Kilic 2008] B. Kilic, *Peridynamic theory for progressive failure prediction in homogeneous and heterogeneous materials*, Ph.D. thesis, The University of Arizona, 2008, Available at http://hdl.handle.net/10150/193658.

[Lipton 2014] R. Lipton, "Dynamic brittle fracture as a small horizon limit of peridynamics", *J. Elasticity* **117**:1 (2014), 21–50.

[Macek and Silling 2007] R. W. Macek and S. A. Silling, "Peridynamics via finite element analysis", *Finite Elem. Anal. Des.* **43**:15 (2007), 1169–1178.

[Madenci and Oterkus 2014] E. Madenci and E. Oterkus, *Peridynamic theory and its applications*, Springer, New York, 2014.

[Oterkus et al. 2014] S. Oterkus, E. Madenci, and A. Agwai, "Peridynamic thermal diffusion", *J. Comput. Phys.* **265** (2014), 71–96.

[Silling 2000] S. A. Silling, "Reformulation of elasticity theory for discontinuities and long-range forces", *J. Mech. Phys. Solids* **48**:1 (2000), 175–209.

[Silling and Askari 2005] S. A. Silling and E. Askari, "A meshfree method based on the peridynamic model of solid mechanics", *Comput. Struct.* **83**:17–18 (2005), 1526–1535.

[Silling and Lehoucq 2010] S. A. Silling and R. B. Lehoucq, "Peridynamic theory of solid mechanics", pp. 73–168 in *Advances in applied mechanics*, edited by H. Aref and E. van der Giessen, Advances in applied mechanics **44**, Elsevier, New York, 2010.

[Silling et al. 2007] S. A. Silling, M. Epton, O. Weckner, J. Xu, and E. Askari, "Peridynamic states and constitutive modeling", *J. Elasticity* **88**:2 (2007), 151–184.

SELDA OTERKUS: seldaalpay@gmail.com
Department of Aerospace and Mechanical Engineering, The University of Arizona, 1130 N Mountain, Tucson, AZ 85721-0119, United States

ERDOGAN MADENCI: madenci@email.arizona.edu
Department of Aerospace and Mechanical Engineering, The University of Arizona, 1130 N Mountain, Tucson, AZ 85721-0119, United States

msp

A HYSTERETIC BINGHAM MODEL FOR MR DAMPERS
TO CONTROL CABLE VIBRATIONS

SELSEBIL SOLTANE, SAMI MONTASSAR, OTHMAN BEN MEKKI AND RACHED EL FATMI

This paper proposes a new parametric dynamic model for magnetorheological (MR) fluid dampers. The proposed model adapts the regularized Bingham model to accurately reproduce the hysteretic behavior of such dampers. The optimized model parameters are then obtained by making the model predictions as close as possible to the reported experimental measurements. As one application of the model, the performances of MR dampers in mitigating free and forced cable vibrations are numerically investigated and evaluated. Numerical simulations results demonstrate the accuracy and the effectiveness of the proposed dynamic hysteretic regularized Bingham model (HRB) in comparison with a standard Bingham model.

1. Introduction

It is widely acknowledged today that long-span cables are prone to vibrations because of their relatively small mass, high flexibility and very low levels of inherent mechanical damping. Large amplitude vibrations of stay cables in cable-stayed structures are one of the major issues that structural engineers aim to obviate. This complex phenomenon is still not fully understood and is most commonly known to be caused by wind [Matsumotoa et al. 1998], by a combination of wind and rain [Hikami and Shiraishi 1988], or by parametric excitation (movements of the pylons or/and the deck in the case of the cable-stayed bridges) [Costa et al. 1996].

In order to mitigate stay cable vibrations, various control techniques and strategies have been developed and some of them have been used in real cable-stayed structures. These techniques include the use of crossing ties or spacers [Langsoe and Larsen 1987], treatment of the stay cable surface to improve its aerodynamic characteristics [Flamand 1995] and use of external dampers. The latter technique is the most widely used of the three nowadays because of its effectiveness in reducing vibrations to an allowable level.

Among the control devices that have been used successfully, the magnetorheological fluid dampers seem to be one of the most reliable and practical. Such dampers are filled with MR fluids which are controllable suspensions that exhibit reversible, rapid and drastic changes in their rheological characteristics when subjected to the application of external magnetic fields.

In order to successfully achieve desirable control performance, it is essential to have a damping force model which can accurately represent the inherent highly nonlinear and hysteretic dynamic behavior of MR dampers. Several quasi-static and dynamic models have been developed for describing the behavior of MR dampers. Quasi-static approaches are based on the study of non-newtonian yield stress fluids flow by using the Bingham model [Hong et al. 2008b; Stanway et al. 1987] or the Herschel–Bulkley model

[Chooi and Oyadiji 2008; Hong et al. 2008a]. Even though quasi-static models are unable to capture the hysteretic force-velocity relationship characterizing the dynamic response of MR dampers, they remain very useful in the preliminary design process and performance prediction of such dampers.

On the other hand, numerous kinds of dynamic models have been proposed in the recent literature. These models focus on the accurate description of the damper nonlinear hysteretic force-velocity relationship. They may be grouped into two distinct categories: nonparametric and parametric models (see the review articles [Wang and Liao 2011; Zhu et al. 2012], which contains an extensive bibliography). The first category includes, among others, neural network models [Chang and Roschke 1998], fuzzy models [Kim et al. 2006] and polynomial models [Choi et al. 2001]. The second category of models consists of those which are based on mechanical constitutive laws such as the viscoelastic-plastic model [Gamota and Filisko 1991], the nonlinear biviscous model [Wereley et al. 1998], the Bouc–Wen model [Piccirillo and Tusset 2014; Spencer et al. 1997], the Dahl model [Zhou et al. 2006], the hyperbolic tangent function model [Guo et al. 2006], the sigmoid function model [Ma et al. 2007], and many others.

In this paper a novel and concise parametric dynamic model for MR fluid dampers is proposed. The optimized model parameters are obtained by best fitting the model predictions with reported experimental data. Based on Galerkin method, the vibration equations for a stay cable/MR damper system are established. Numerical simulations associated with a stay cable, belonging to the Rades-La Goulette cable-stayed bridge, are carried out. The effectiveness of the proposed HRB model, compared to the standard Bingham model, for the MR damper on the vibration mitigation of the considered cable subjected to the free and forced vibration is investigated.

2. The proposed model for MR dampers

The damping force F_d^B generated by the MR dampers, dependent on the time variable t and using the rigid-viscoplastic Bingham model, is given by a relationship of the form

$$
\begin{aligned}
F_d^B(t) - F_0 &= C_v v_d + F_y \operatorname{sgn}(v_d) \quad &&\text{if } F_d^B(t) - F_0 \geq F_y, \\
v_d &= 0 \quad &&\text{if } 0 \leq F_d^B(t) - F_0 \leq F_y,
\end{aligned}
\tag{1}
$$

where v_d denotes the piston velocity, F_0 the offset in the damping force due to the presence of the accumulator, F_y the frictional force related to the yield stress of the MR fluid (generally depending on the applied magnetic field) and C_v the damping coefficient. The latter is defined as the slope of the damping force versus the piston velocity and is related to the plastic viscosity of the MR fluid. The above relationship, illustrated through the dashed bilinear diagram of Figure 1, expresses the fact that the viscoplastic flow of the MR fluid occurs only if the damping force exceeds the frictional force.

Furthermore, an approximation to the strict Bingham model by means of a regularization technique may be introduced, similar to that employed in [Papanastasiou 1987]. In such a case, the discontinuous Bingham equation (1) is replaced by a continuous equation characterized by a regularization parameter and the damping force F_d^{RB} may be expressed in the form

$$
F_d^{RB}(t) - F_0 = C_v v_d + F_y \left[1 - \exp\left(-\operatorname{sgn}(v_d) \frac{v_d}{v_0} \right) \right] \operatorname{sgn}(v_d),
\tag{2}
$$
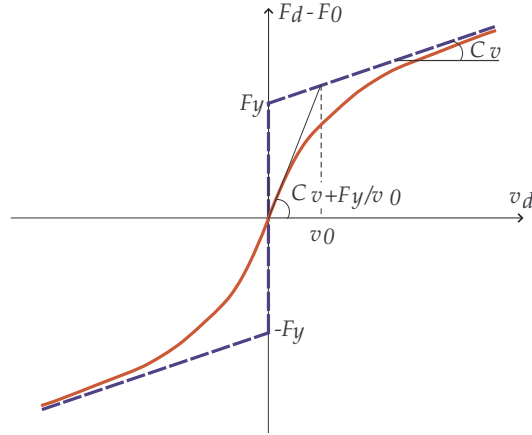
Figure 1. Bingham (dashed line) and regularized Bingham (continuous line) models.

where v_0 denotes the regularization parameter, which has a velocity dimension and controls the exponential growth of the damping force. It is clear from the above formula, that the smaller is this parameter, the better is the approximation of the initial Bingham model, as illustrated in Figure 1.

To take into account the nonlinear hysteretic behavior of the MR damper, we transform (2) to describe a hysteresis loop depicted in Figure 2 and defined for every piston velocity $v_d \in [-v_m, v_m]$ by

$$F_d^{\mathrm{HRB}}(t) - F_0 = \begin{cases} C_v(v_d - v_h) + F_y\left[1 - \exp\left(-\operatorname{sgn}(v_d - v_h)\dfrac{v_d - v_h}{v_0}\right)\right]\operatorname{sgn}(v_d - v_h) & \text{for } \dot{v}_d < 0, \\[2mm] C_v(v_d + v_h) + F_y\left[1 - \exp\left(-\operatorname{sgn}(v_d + v_h)\dfrac{v_d + v_h}{v_0}\right)\right]\operatorname{sgn}(v_d + v_h) & \text{for } \dot{v}_d > 0, \end{cases} \tag{3}$$

where v_h is a scale factor having the dimension of a velocity which defines the width of the hysteresis loop and v_m denotes the maximum reached velocity of the damper piston. The obtained hysteresis loop is composed of an upper curve relating to the force variation with respect to the decreasing velocities, and a lower curve corresponding to the force variation with increasing velocities.
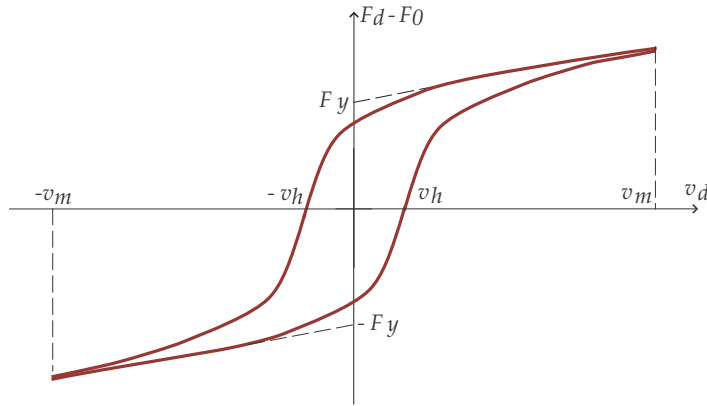
Figure 2. The hysteretic regularized Bingham model (HRB).

3. Identification procedure and model validation through experimental results

In order to accurately model the performance of MR dampers, the proposed dynamic hysteretic regularized Bingham model requires identification of a set of 6 parameters

$$\Xi = \{F_0, F_y, C_v, v_0, v_h, v_m\}. \tag{4}$$

These parameters are obtained by best fitting the model predictions with reported experimental data. This may be accomplished using a multidimensional optimization procedure by means of least-squares.

The experimental data obtained from a series of tests conducted to measure the mechanical response of the MRF132-LD type MR damper system (developed and manufactured by the LORD Corporation) and reported in [Choi et al. 2001] have been first considered. The MR damper was excited sinusoidally with an excitation frequency of 1.4 Hz and an exciting magnitude of ±20 mm at various input currents I (0.0, 1.2 and 2.0 A).

The values of the parameters defined in Equation (4) are adjusted by fitting numerical MR damper force-velocity responses computed from simulations, using the proposed dynamic hysteretic regularized Bingham model, to experimental data measured at different input currents. The obtained values are listed in Table 1. Figure 3 shows good agreement between the measured data and the results of simulations carried out using the identified parameters.

The results of a second series of tests reported in [Guo et al. 2006] have also been analyzed. The MR damper, designed by the Shijiazhuang Railway Institute, was tested under a 1.5 Hz sinusoidal excitation with an amplitude of ±5 mm at various input currents I (0.0, 0.5, 1.0, 1.5 and 2.0 A). It appears from Figure 4 that the MR damper force-velocity responses obtained from numerical simulations, using the identified parameters listed in Table 1, match the recorded experimental measurements very well.

We point out that the values of the identified parameters F_0, C_v, v_0, v_h and v_m remain almost constant,
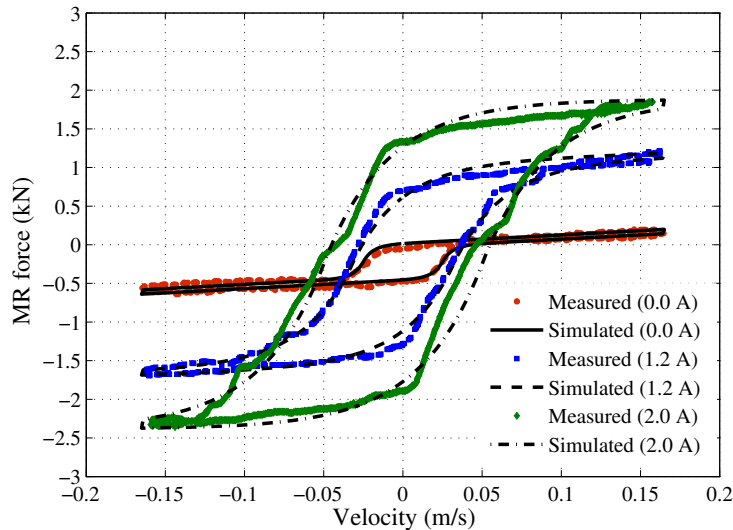
Figure 3. Comparison of model predictions and experimental results reported in [Choi et al. 2001].

Model parameters	Damper from [Choi et al. 2001]			Damper from [Guo et al. 2006]				
I (A)	0	1.2	2.0	0	0.5	1.0	1.5	2.0
F_0 (N)	240	250	250	20	25	20	30	30
F_y (N)	210	1280	2130	250	370	620	850	1070
C_v (N.s/mm)	0.9	0.8	0.7	0.9	1	1	1	1
v_0 (mm/s)	36	30	32	9	8	9	8	9
v_h (mm/s)	29	32	38	8	6	6	6	5
v_m (mm/s)	165	165	165	46.5	46.5	46.5	46.5	46.5

Table 1. Identified model parameters.
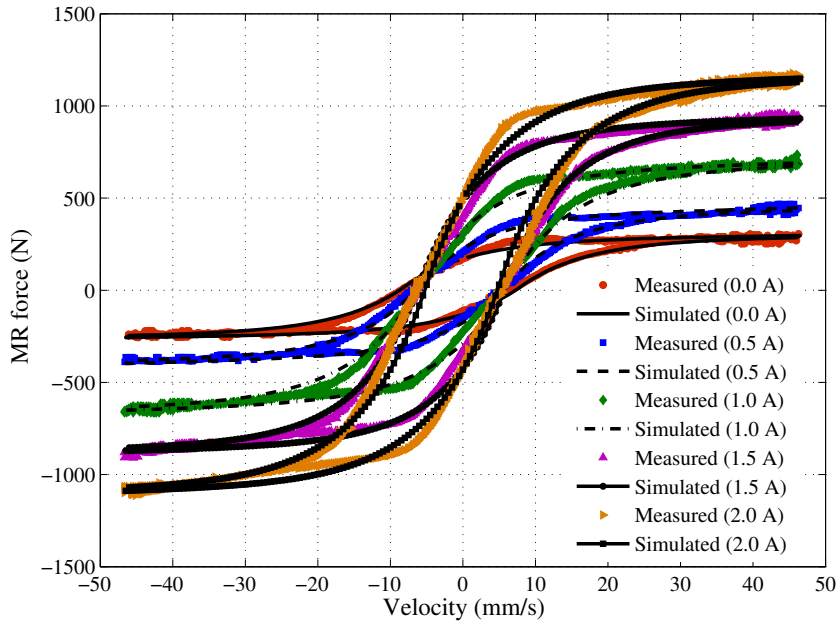
Figure 4. Comparison of model predictions and experimental results reported from [Guo et al. 2006].

while the value of F_y is sensitive to the change of the electrical current I supplied to the MR damper. Furthermore, the frictional force F_y can be linearized with respect to the input current as

$$F_y(I) = \alpha I + \beta, \qquad (5)$$

where α and β are constant coefficients. $\alpha = 956.6\,\text{N.A}^{-1}$ and $\beta = 196.3\,\text{N}$ for the Damper from [Choi et al. 2001], while $\alpha = 414\,\text{N.A}^{-1}$ and $\beta = 228\,\text{N}$ for the Damper from [Guo et al. 2006].

4. Control of cable transverse vibration with an attached MR damper

4A. *Problem formulation for a stay cable/MR damper system.* Consider a uniform and flexible inclined stay cable subjected to its self-weight (m_c denotes the cable's mass per unit length) and hanged at its fixed
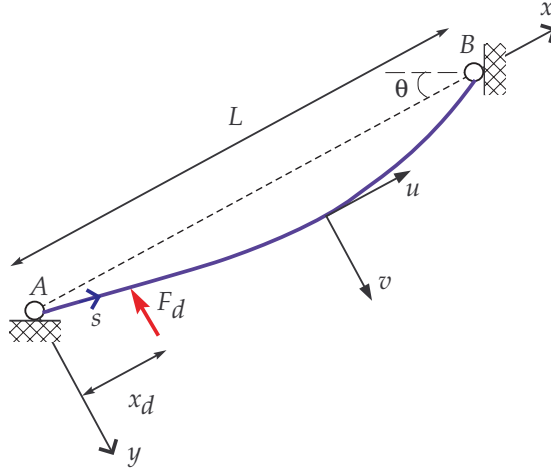
Figure 5. An inclined cable with an attached damper.

end-points A and B that are situated at different levels, as sketched in Figure 5. The stay cable, assumed to be homogeneous and constituted by an isotropic linearly elastic material with Young's modulus E_c, has a chord length L and is inclined at an angle θ to the horizontal. The cable's cross-section is undeformable and its area is denoted by A_c. The strained static profile of the cable is spanned by the curvilinear co-ordinate s with $s = 0$ at A.

Planar oscillations are considered in the Cartesian frame (A, x, y) where the y axis is perpendicular to the x axis taken along the cable's chord. The cable is subjected to a distributed external excitation F_{ext} as well as a transverse concentrated force denoted by F_d due to the presence of a MR damper attached at the location x_d from the support A in the x direction (Figure 5).

The equations governing the dynamic equilibrium of an inclined cable may be written as

$$
\begin{cases}
\dfrac{\partial}{\partial s}\left[(T+\tau)\left(\dfrac{dx}{ds}+\dfrac{\partial u}{\partial s}\right)\right] + F_{\text{ext},x}(x,t) = m_c\left(\dfrac{\partial^2 u}{\partial t^2} + g\sin\theta\right) \\[2mm]
\dfrac{\partial}{\partial s}\left[(T+\tau)\left(\dfrac{dy}{ds}+\dfrac{\partial v}{\partial s}\right)\right] + F_{\text{ext},y}(x,t) + F_d(t)\delta(x-x_d) = m_c\left(\dfrac{\partial^2 v}{\partial t^2} - g\cos\theta\right) \\[2mm]
\dfrac{\partial}{\partial s}\left[(T+\tau)\dfrac{dw}{ds}\right] + F_{\text{ext},z}(x,t) = m_c\dfrac{\partial^2 w}{\partial t^2}
\end{cases}
\tag{6}
$$

where $\tau = E_c A_c \epsilon^D$ is the additional dynamic cable tension, ϵ^D is the additional dynamic axial strain, T is the static stay's tension, g is the acceleration of gravity, $\delta(.)$ is the Dirac's delta function, while u, v and w are the cable dynamic displacement components in the x, y and z directions, respectively.

Considering a Green–Lagrange strain measure, the contribution ϵ^D can be described as

$$
\epsilon^D = \frac{\partial u}{\partial x} + \frac{dy}{dx}\frac{\partial v}{\partial x} + \frac{1}{2}\left[\left(\frac{\partial u}{\partial x}\right)^2 + \left(\frac{\partial v}{\partial x}\right)^2 + \left(\frac{\partial w}{\partial x}\right)^2\right].
\tag{7}
$$

In the foregoing, the following simplifying assumptions are enforced:

- Due to the high tension levels in the stay cable, small sag effects appear (i.e., $ds \simeq dx$). Consequently, the static equilibrium configuration can be described by a parabolic profile (see [Ben Mekki and Auricchio 2011; Irvine 1981] for more details).

- The transversal frequency is smaller than the longitudinal frequency. Thus, the longitudinal (i.e., along the x-direction) inertial force vanishes and the additional dynamic tension τ is approximated as a constant with respect to x.

- By assuming small deformations, second order terms of ϵ^D can be neglected and the additional dynamic tension is considered as a small perturbation with respect to the static tension T.

Making use of these simplifying assumptions, the transverse deflection $v(x, t)$ of the stay cable satisfies the differential equation of motion for the combined stay cable/MR damper system

$$m_c \frac{\partial^2 v}{\partial t^2} - T \frac{\partial^2 v}{\partial x^2} + \frac{E_c A_c}{L} \left(\frac{m_c g \cos \theta}{T} \right)^2 \int_0^L v \, dx = F_{\text{ext}, y} - F_d \delta(x - x_d). \tag{8}$$

The transverse deflection can be approximated using a finite modal superposition of the form

$$v(x, t) = \sum_{i=1}^{N} \xi_i(t) \varphi_i(x) \tag{9}$$

where $\xi_i(t)$ are non-dimensional modal participation factors and $\varphi_i(x)$ are a set of modal shape functions, assumed to be continuous and to satisfy the geometric boundary conditions at the cable's ends A and B.

By assuming sinusoidal modal shape functions as

$$\varphi_i(x) = \sin \left(\frac{i \pi x}{L} \right) \tag{10}$$

and performing a Galerkin-type approximation of (8), the time-dependent generalized modal coordinates $\xi_i(t)$ can be determined by solving the differential equations

$$m_i \ddot{\xi}_i(t) + \left(k_i + \eta m_i \right) \xi_i(t) = F_i - F_d(t) \varphi_i(x_d) \quad \text{for} \quad i = 1 \ldots N \tag{11}$$

where

$$\eta = \frac{E_c A_c}{L} \left(\frac{m_c g \cos \theta}{T} \right)^2,$$

$$m_i = m_c \int_0^L \varphi_i(x) \varphi_i(x) \, dx = m_c \frac{L}{2},$$

$$k_i = T \int_0^L \frac{d\varphi_i}{dx} \frac{d\varphi_i}{dx} \, dx = \frac{T \pi^2 i^2}{2L},$$

$$F_i = m_c \int_0^L F_{\text{ext}, y}(t) \varphi_i(x) \, dx.$$

It is to be noticed that the presence of the MR damper introduces non-linearity into the stay cable/MR damper system. The Newmark scheme is adopted to obtain the numerical solutions of the system of dynamical equations (11).

L [m]	θ [°]	T [kN]	E_c [GPa]	A_c [cm^2]	m_c [kg/m]
55.4	16.5	4313.5	190	55.5	44

Table 2. Geometrical and mechanical design properties of the stay cable (S16) of the Rades-La Goulette cable-stayed bridge.

4B. *An illustrative numerical application.* The longest cable (S16) in the Rades-La Goulette cable-stayed bridge is considered to investigate the effects of the MR damper parameters on the damping capability and control efficacy.

Opened for traffic in 2009, the Rades-La Goulette cable-stayed bridge was built over the Tunis Lake Canal in Tunisia. The total length of the bridge is 260 m divided into three spans, with a 120 m long central span. Two 40 m tall towers carry a pre-stressed concrete deck. Each pylon is equipped with a stay curtain comprising 8 pairs of stays, arranged following a semi-harp scheme and leading to a symmetric bridge scheme with respect to both the axial vertical plane and the mid-span cross-plane.

The geometrical and material properties of the considered stay cable (S16) are summarized in Table 2. The internal damping of the cable is not considered. A MRF132-LD type MR damper, whose characteristics are listed in Table 1, is attached to the stay cable (S16) at the location $x_d = 0.1L$.

Figure 6 compares the modal contributions of the first mode vibration $\alpha_1(t)$ as well as the damper force evolutions computed by considering the proposed HRB model and the Bingham model. Both modal contributions have been obtained by solving system (11) in which the corresponding model of the MR damper has been introduced for a supplied current of 2.0 A. It is worth noting that the cable vibration is damped more effectively when using the proposed HRB model.

According to Figure 6, it can also be observed that the largest vibration response using the proposed HRB model is around 70% of the one obtained by means of the Bingham model and that the vibration decay speed is much faster. An equivalent viscous damping value of the Bingham model is 2.5%. However, the equivalent viscous damping value of the proposed HRB model is 9.2%. It turns out that the proposed HRB model is very effective to reduce structural response. This could be explained by the fact that it can provide a large damper force under small velocities and displacements.

The stay cable/MR damper system is then subjected to an external harmonic excitation of the form

$$F_{\text{ext},y}(t) = 1.5 \cos\left(\sqrt{\frac{k_1}{m_1}}t\right). \tag{12}$$

After a brief transitory period, the stay cable/MR damper (of 2.0 A current) system reaches a periodic regime and the modal coordinate exhibits a sinusoidal behavior in time at frequency $f_{\text{ext}} = \sqrt{k_1/m_1}$. Figure 7 shows that the proposed HRB model is again able to damp the harmonic excitation better than the Bingham model.

Vibrations of stay cables in cable stayed-bridges are mainly caused by two phenomena: cable support motion from either the bridge-girder or the pylon mainly coming from heavy vehicles, and aerodynamic actions on the cable itself from wind or a combination of wind and rain. The augmented system damping due to the attached external actuator is often used to measure the efficacy of a vibration control device. For a long stay cable, damping ratio is the most important parameter that dominates aerodynamic stability.
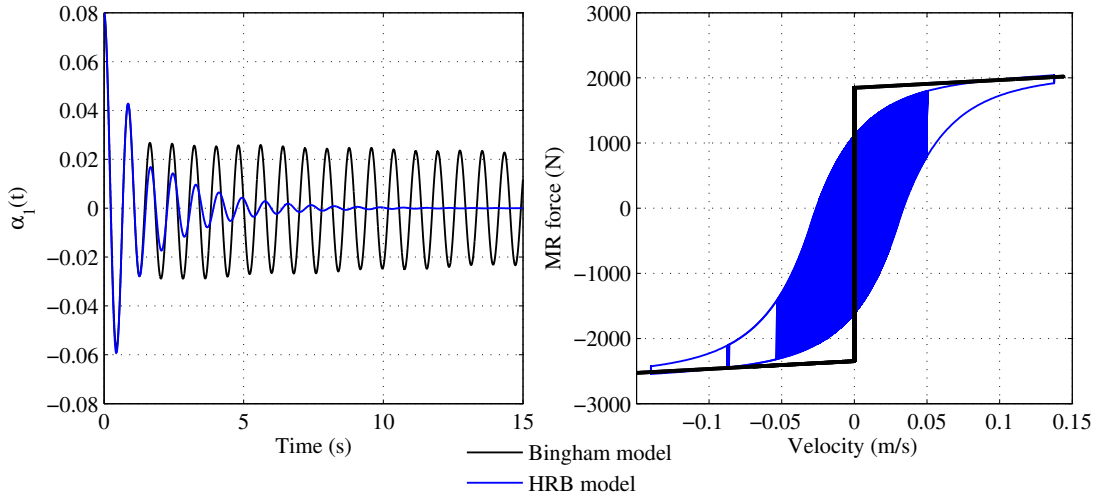
Figure 6. Control of the stay cable free vibration: comparison between the proposed HRB model and the Bingham model.
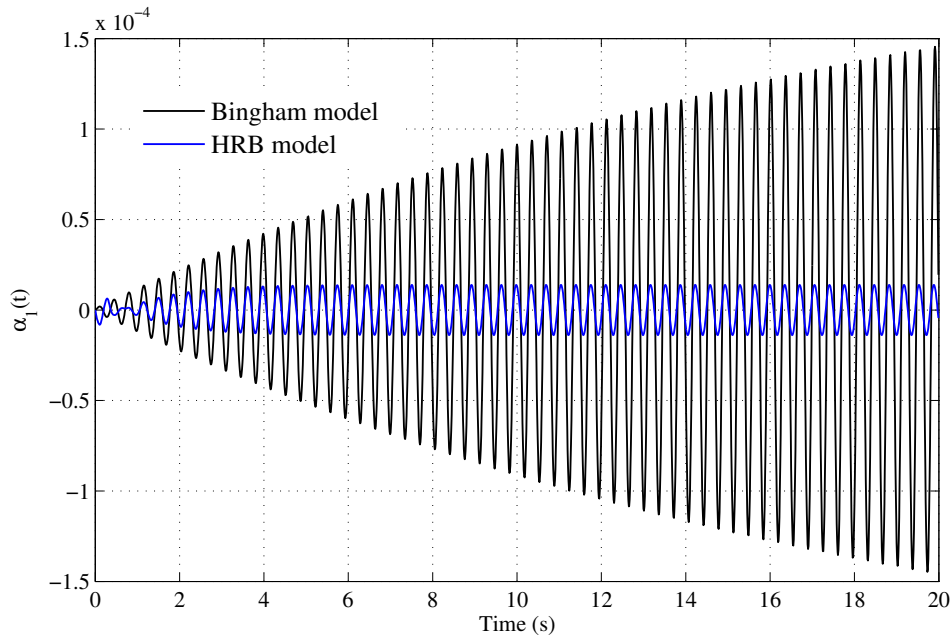
Figure 7. Cable response under a harmonic excitation.

This added damping coefficient by means of an external damping device can be tuned on a wind velocity. The responses of a stay cable will be analyzed with a stepping switch strategy under various constant input currents.

In order to show its influence on the achieved damping of the cable, several values of the supplied electric current are used in the numerical simulations. The force-velocity relationships using the dynamic
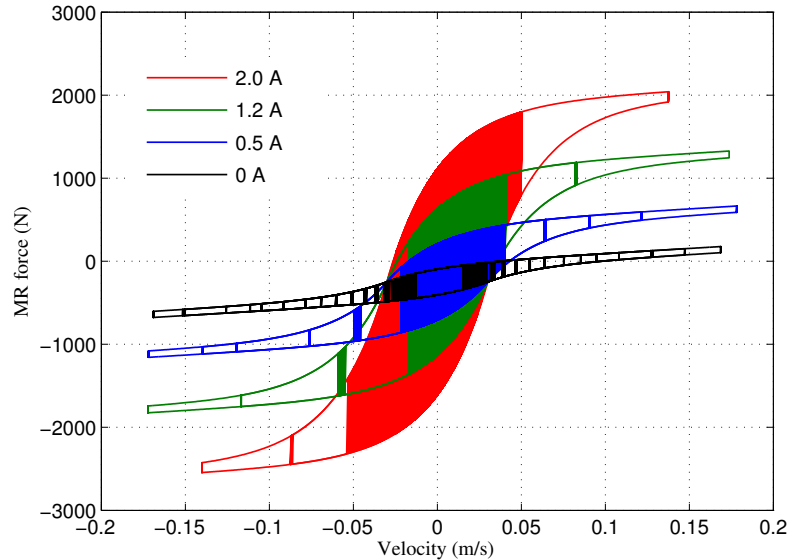
Figure 8. Damper force-velocity relationships for different values of supplied current.

HRB model, for different values of input electric current, are plotted in Figure 8. It can be seen that the MR damper exhibits strong nonlinear hysteretic behavior as well as an excellent property of energy dissipation. Furthermore, the area of the hysteresis loop increases significantly corresponding to the raise of the input current supplied to the MR damper.

In Figure 9 several responses evaluated according to the complete system (11) using the HRB model in correspondence of different values of input electric current are depicted. The effect of the supplied electric current in regulating the equivalent viscous damping clearly appears, as predicted by (5). In particular, the values of the equivalent viscous damping are 1.6%, 4.2%, 7.7% and 9.2% in correspondence of different values of input electric current, respectively, 0 A, 0.5 A, 1.2 A and 2.0 A. The evaluation of the
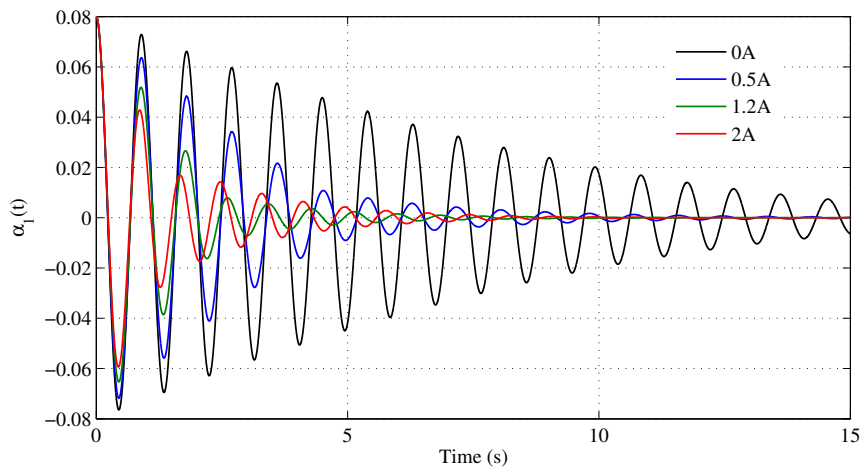
Figure 9. Control of the stay cable free vibration: influence of the input electric current.

equivalent viscous damping has been carried out by using a numerical optimization with the conjugate gradient method. Accordingly, the equivalent viscous damping is chosen by minimizing the square difference between the free response of the system (11) using the proposed HRB model for the MR damper, and the one obtained using a viscous damping.

5. Conclusion

This paper has addressed a new nonlinear dynamic model for a magnetorheological damper to accurately reconstruct the hysteretic relationship between the damping force and the velocity. The optimized model parameters are obtained by reproducing numerically the hysteretic responses of the reported experimental damper force-velocity data. Vibration equations for the stay cable/MR damper system are derived for the analysis of cable vibration mitigation using the proposed HRB model and the standard Bingham model. The longest cable in the Rades-La Goulette cable-stayed bridge is considered. The numerical simulations demonstrate that the proposed HRB model is able to control free and forced vibrations better than the Bingham model.

References

[Ben Mekki and Auricchio 2011] O. Ben Mekki and F. Auricchio, "Performance evaluation of shape-memory-alloy superelastic behavior to control a stay cable in cable-stayed bridges", *International Journal of Non-Linear Mechanics* **46** (2011), 470–477.

[Chang and Roschke 1998] C. Chang and P. Roschke, "Neural network modeling of a magnetorheological damper", *Journal of Intelligent Material Systems and Structures* **9** (1998), 755–764.

[Choi et al. 2001] S. B. Choi, S. K. Lee, and Y. P. Park, "A hysteresis model for the field-dependent damping force of a magnetorheological damper", *Journal of Sound and Vibration* **245**:2 (2001), 375–383.

[Chooi and Oyadiji 2008] W. W. Chooi and S. O. Oyadiji, "Design, modelling and testing of magnetorheological (MR) dampers using analytical flow solutions", *Computers and Structures* **86**:3–5 (2008), 473–482.

[Costa et al. 1996] A. Costa, J. Martins, F. Branco, and J. Lilien, "Oscillations of bridge stay cables induced by periodic motions of deck and/or towers", *Journal of Engineering Mechanics* **122**:7 (1996), 613–622.

[Flamand 1995] O. Flamand, "Rain-wind induced vibration of cables", *Journal of Wind Engineering and Industrial Aerodynamics* **57**:2–3 (1995), 353–362.

[Gamota and Filisko 1991] D. R. Gamota and F. E. Filisko, "Dynamic mechanical studies of electrorheological materials: moderate frequencies", *Journal of Rheology* **35** (1991), 399–425.

[Guo et al. 2006] S. Guo, S. Yang, and C. Pan, "Dynamic modeling of magnetorheological damper behaviors", *Journal of Intelligent Material Systems and Structures* **17**:3 (2006), 3–14.

[Hikami and Shiraishi 1988] Y. Hikami and N. Shiraishi, "Rain-wind induced vibrations of cables stayed bridges", *Journal of Wind Engineering and Industrial Aerodynamics* **29**:1–3 (1988), 409–418.

[Hong et al. 2008a] S. R. Hong, S. John, N. M. Wereley, Y. T. Choi, and S. B. Choi, "A unifying perspective on the quasi-steady analysis of magnetorheological dampers", *Journal of Intelligent Material Systems and Structures* **19** (2008), 959–976.

[Hong et al. 2008b] S. R. Hong, N. M. Wereley, Y. T. Choi, and S. B. Choi, "Analytical and experimental validation of a nondimensional Bingham model for mixed-mode magnetorheological dampers", *Journal of Sound and Vibration* **312**:3 (2008), 399–417.

[Irvine 1981] H. M. Irvine, *Cable structures*, The MIT Press, Cambridge, 1981.

[Kim et al. 2006] H. S. Kim, P. N. Roschke, P. Y. Lin, and C. H. Loh, "Neuro-fuzzy model of hybrid semi-active base isolation system with FPS bearings and an MR damper", *Engineering Structures* **28**:7 (2006), 947–958.

[Langsoe and Larsen 1987] H. E. Langsoe and O. D. Larsen, "Generating mechanisms for cable stay oscillations at the FARO bridges", in *Proceedings of the international conference on cable-stayed bridges*, Asian Institute of Technology, Bangkok, Thailand, 1987.

[Ma et al. 2007] X. Q. Ma, S. Rakheja, and C. Y. Su, "Development and relative assessments of models for characterizing the current dependent hysteresis properties of magnetorheological fluid dampers", *Journal of Intelligent Material Systems and Structures* **18** (2007), 487–502.

[Matsumotoa et al. 1998] M. Matsumotoa, Y. Daitob, T. Kanamurac, Y. Shigemuraa, S. Sakumad, and H. Ishizakie, "Wind-induced vibration of cables of cable-stayed bridges", *Journal of Wind Engineering and Industrial Aerodynamics* **74–76** (1998), 1015–1027.

[Papanastasiou 1987] T. C. Papanastasiou, "Flow of materials with yield", *Journal of Rheology* **31** (1987), 385–404.

[Piccirillo and Tusset 2014] V. Piccirillo and A. M. Tusset, "Dynamical jump attenuation in a non-ideal system through a magnetorheological damper", *Journal of Theoretical and Applied Mechanics* **52**:3 (2014), 595–604.

[Spencer et al. 1997] B. F. Spencer, Jr, S. J. Dyke, M. K. Sain, and J. D. Carlson, "Phenomenological model for magnetorheological dampers", *Journal of Engineering Mechanics* **123**:3 (1997), 230–238.

[Stanway et al. 1987] R. Stanway, J. L. Sproston, and N. G. Stevens, "Non-linear modeling of an electrorheological vibration damper", *Journal of Electrostatics* **20**:2 (1987), 167–184.

[Wang and Liao 2011] D. H. Wang and W. H. Liao, "Magnetorheological fluid dampers: a review of parametric modelling", *Smart Materials and Structures* **20**:2 (2011), 1–34.

[Wereley et al. 1998] N. M. Wereley, L. Pang, and G. M. Kamath, "Idealized hysteresis modeling of electrorheological and magnetorheological dampers", *Journal of Intelligent Material Systems and Structures* **9**:8 (1998), 642–649.

[Zhou et al. 2006] Q. Zhou, S. R. K. Nielsen, and W. L. Qu, "Semi-active control of three-dimensional vibrations of an inclined sag cable with magnetorheological dampers", *Journal of Sound and Vibration* **296**:1–2 (2006), 1–22.

[Zhu et al. 2012] X. Zhu, X. Jing, and L. Cheng, "Magnetorheological fluid dampers: a review on structure design and analysis", *Journal of Intelligent Material Systems and Structures* **23**:8 (2012), 839–873.

SELSEBIL SOLTANE: soltane_selsebil@yahoo.fr
Université de Tunis El Manar, Ecole Nationale d'Ingénieurs de Tunis, LGC, BP 37, Le Belvédère, 1002 Tunis, Tunisia

SAMI MONTASSAR: sami.montassar@enit.rnu.tn
Université de Tunis El Manar, Ecole Nationale d'Ingénieurs de Tunis, LGC, BP 37, Le Belvédère, 1002 Tunis, Tunisia

OTHMAN BEN MEKKI: mekki07@unipv.it
Université de Tunis El Manar, Ecole Nationale d'Ingénieurs de Tunis, LGC, BP 37, Le Belvédère, 1002 Tunis, Tunisia

RACHED EL FATMI: rached.elfatmi@enit.rnu.tn
Université de Tunis El Manar, Ecole Nationale d'Ingénieurs de Tunis, LGC, BP 37, Le Belvédère, 1002 Tunis, Tunisia

SUBMISSION GUIDELINES

ORIGINALITY

Authors may submit manuscripts in PDF format online at the Submissions page. Submission of a manuscript acknowledges that the manuscript is original and has neither previously, nor simultaneously, in whole or in part, been submitted elsewhere. Information regarding the preparation of manuscripts is provided below. Correspondence by email is requested for convenience and speed. For further information, write to contact@msp.org.

LANGUAGE

Manuscripts must be in English. A brief abstract of about 150 words or less must be included. The abstract should be self-contained and not make any reference to the bibliography. Also required are keywords and subject classification for the article, and, for each author, postal address, affiliation (if appropriate), and email address if available. A home-page URL is optional.

FORMAT

Authors can use their preferred manuscript-preparation software, including for example Microsoft Word or any variant of TeX. The journal itself is produced in LaTeX, so accepted articles prepared using other software will be converted to LaTeX at production time. Authors wishing to prepare their document in LaTeX can follow the example file at www.jomms.net (but the use of other class files is acceptable). At submission time only a PDF file is required. After acceptance, authors must submit all source material (see especially Figures below).

REFERENCES

Bibliographical references should be complete, including article titles and page ranges. All references in the bibliography should be cited in the text. The use of BibTeX is preferred but not required. Tags will be converted to the house format (see a current issue for examples); however, for submission you may use the format of your choice. Links will be provided to all literature with known web locations; authors can supply their own links in addition to those provided by the editorial process.

FIGURES

Figures must be of publication quality. After acceptance, you will need to submit the original source files in vector format for all diagrams and graphs in your manuscript: vector EPS or vector PDF files are the most useful. (EPS stands for Encapsulated PostScript.)

Most drawing and graphing packages—Mathematica, Adobe Illustrator, Corel Draw, MATLAB, etc.—allow the user to save files in one of these formats. Make sure that what you're saving is vector graphics and not a bitmap. If you need help, please write to graphics@msp.org with as many details as you can about how your graphics were generated.

Please also include the original data for any plots. This is particularly important if you are unable to save Excel-generated plots in vector format. Saving them as bitmaps is not useful; please send the Excel (.xls) spreadsheets instead. Bundle your figure files into a single archive (using zip, tar, rar or other format of your choice) and upload on the link you been given at acceptance time.

Each figure should be captioned and numbered so that it can float. Small figures occupying no more than three lines of vertical space can be kept in the text ("the curve looks like this:"). It is acceptable to submit a manuscript with all figures at the end, if their placement is specified in the text by means of comments such as "Place Figure 1 here". The same considerations apply to tables.

WHITE SPACE

Forced line breaks or page breaks should not be inserted in the document. There is no point in your trying to optimize line and page breaks in the original manuscript. The manuscript will be reformatted to use the journal's preferred fonts and layout.

PROOFS

Page proofs will be made available to authors (or to the designated corresponding author) at a Web site in PDF format. Failure to acknowledge the receipt of proofs or to return corrections within the requested deadline may cause publication to be postponed.

Journal of Mechanics of Materials and Structures

Volume 10, No. 2   March 2015